THE RELATIONSHIP OF MICROSTRUCTURE TO FRACTURE AND CORROSION BEHAVIOR OF A DIRECTIONALLY SOLIDIFIED SUPERALLOY

A Thesis
Presented to
The Academic Faculty

by

Matthew D. Trexler

In Partial Fulfillment
of the Requirements for the Degree
Doctor of Philosophy in the
School of Materials Science and Engineering

Georgia Institute of Technology
May 2007

THE RELATIONSHIP OF MICROSTRUCTURE TO FRACTURE AND CORROSION BEHAVIOR OF A DIRECTIONALLY SOLIDIFIED SUPERALLOY

Approved by:

Dr. Thomas H. Sanders Jr., Advisor
School of Materials Science and Engineering
Georgia Institute of Technology

Dr. Arun Gokhale
School of Materials Science and Engineering
Georgia Institute of Technology

Dr. David McDowell
Woodrow School of Mechanical Engineering
Georgia Institute of Technology

Dr. Richard Neu
Woodrow School of Mechanical Engineering
Georgia Institute of Technology

Dr. Preet Singh
School of Materials Science and Engineering
Georgia Institute of Technology

Date Approved: December 11, 2006

Dedicated to my family

ACKNOWLEDGEMENTS

I would like to acknowledge Dr. Thomas Sanders for his support during my time at Georgia Tech as a research advisor, mentor and friend. I would like to thank Dr. Preet Singh, Dr. Richard Neu, Dr. David McDowell, and Dr. Arun Gokhale for being members of my thesis committee and whose advice was of great value to me during this work. Special thanks to both Dr. Mahesh Shenoy and Dr. Ali Gordon for our many discussions about research, specifically about GTD-111 DS. I would also like to acknowledge my fellow group members both past and present: Dr. Jason Nadler, Dr. Benjamin Church, Dr. Tracie Durbin, Peter Chamberlain and Laura Cerully for their support over the years. This research was funded by both GE Energy and The Institute of Paper Science and Technology at Georgia Tech to whom I am also grateful.

Finally, I would like to acknowledge my family as well as Morgana Martin without whose love and support I could not survive.

TABLE OF CONTENTS

LIST OF TABLES

LIST OF FIGURES

SUMMARY

GTD-111 DS is a directionally solidified superalloy currently used in turbine engines. To accurately predict the life of engine components it is essential to examine and characterize the microstructural evolution of the material and its effects on material properties. The as-cast microstructure of GTD-111 is highly inhomogeneous as a result of coring. The current post-casting heat treatments do not effectively eliminate the inhomogeneity. This inhomogeneity affects properties including tensile strength, fracture toughness, fracture path, and corrosion behavior, primarily in terms of the number of grains per specimen. The goal of this work was to link microstructural features to these properties.

Quantitative fractography was used to determine that the path of cracks during failure of tensile specimens is influenced by the presence of carbides, which are located in the interdendritic regions of the material as dictated by segregation. The solvus temperature of the precipitate phase, $Ni_3(Al, Ti)$, was determined to be 1200°C using traditional metallography, differential thermal analysis, and dilatometry. A heat-treatment was designed to homogenize the microstructure for tensile testing that isolates the carbide by dissolving all of the "eutectic" $Ni_3(Al, Ti)$ precipitate phase, which is also found in the interdendritic areas.

High temperature oxidation/sulfidation tests were conducted to investigate the corrosion processes involved when GTD-111 DS is utilized in steam and gas combustion turbine engines. The kinetics of corrosion in both oxidizing and sulfidizing atmospheres were determined using thermogravimetric analysis. Additionally, metallography of these samples after TGA revealed a correlation between the presence of grain boundaries and sulfur attack, which led to catastrophic failure of the material under stress-free conditions in a sulfur bearing environment. In summary, this work correlates the inhomogeneous microstructure of GTD-111 DS to tensile fracture, and the corrosion process in turbine engines.

CHAPTER I

INTRODUCTION

Recent advances in coal combustion have made coal a cleaner, more viable source for power generation. Integrated Gasification Combined Cycle (IGCC) plants pair conventional steam turbines and coal gas turbines. The process uses the coal gasification reaction to power both systems by using the heat of the process to generate steam for the convention turbines and then channeling the gasified coal (syngas), into a second set of turbines as seen in figure 1.

The overall efficiency of each system is largely dependent on the maximum operating temperature of the system, which is limited by the available materials. Superalloys have long been used as a turbine material due to their high temperature strength and general resistance to oxidation. Superalloy GTD-111 DS is currently being used as components in steam turbine engine such as turbine blades and discs and is now being introduced to the syngas environment, which consists of H_2, CO, CH_4, and H_2S in addition to H_2O. H_2S is highly corrosive and complicates the corrosion process. The degradation and failure of turbine components in an operating system is dangerous and costly. There is a clear need to predict the life of these components. This requires an understanding of mechanical properties as well as corrosion properties of the alloy as they relate to microstructure and turbine environments. The increasing use of IGCC engines is the impetus for research which advances the understanding of how steam and syngas turbine environments affect components at high temperatures. The key to reaching this goal rests in linking the microstructure of GTD-111, which is highly inhomogeneous and anisotropic, to mechanical properties and corrosion in both turbine environments.

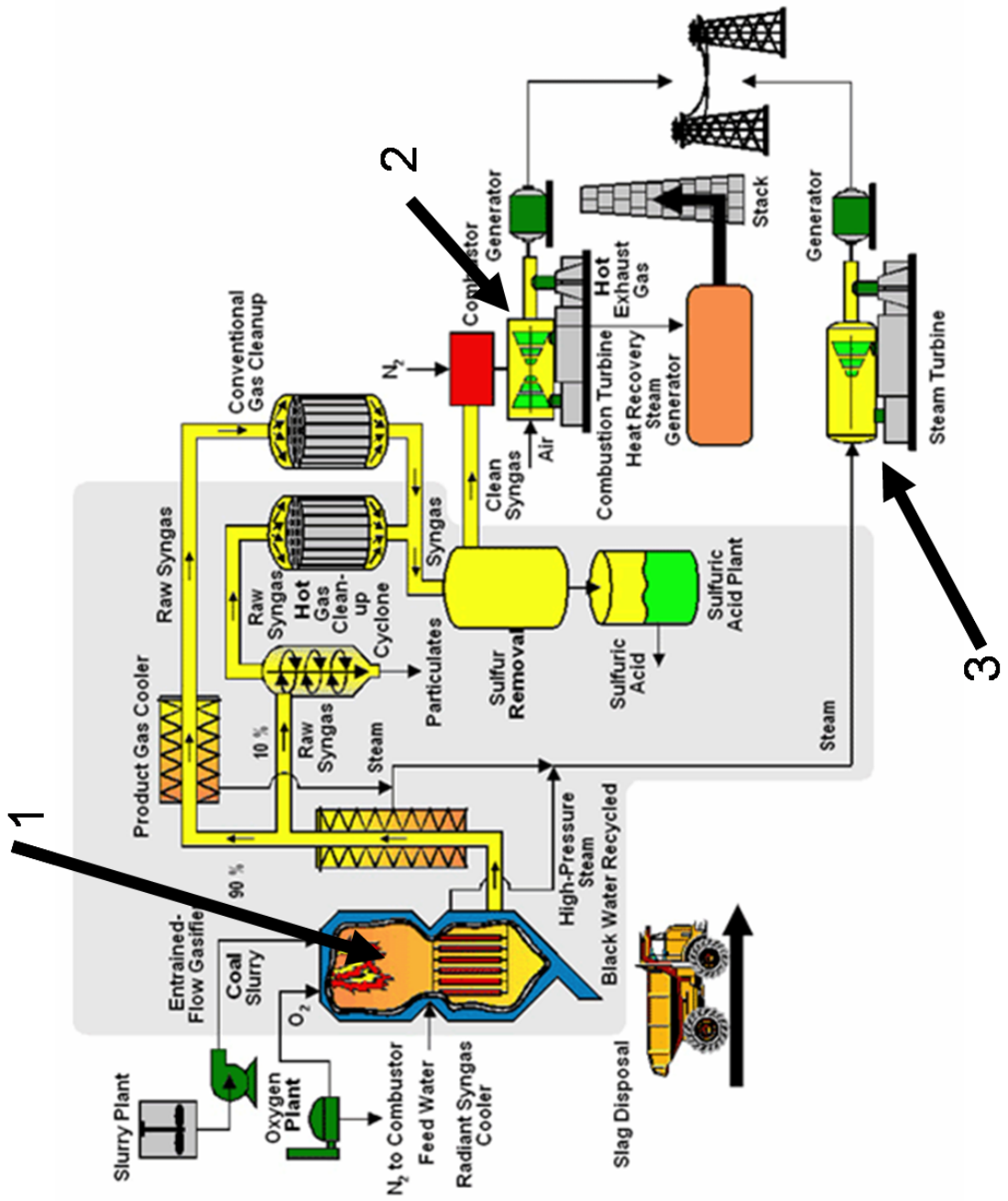

Figure 1: Diagram of an integrated gasification combined cycle (IGCC) process [1] in which coal is gasified (1), cleaned and passed through a gas turbine to generate electricity (2). The thermal energy used to gasify the coal also provides a source of steam for a convention turbine (3).

1.1 Overview

This dissertation begins in chapter two with general background of directionally solidified superalloys in terms of microstructural features, mechanical behavior and corrosion properties. Chapter three summarizes the microstructural characterization of bulk GTD-111 DS. The experimental work and subsequent results are separated into three parts: microstructure as it relates to tensile failure, microstructure refinement through heat-treatment, and high temperature oxidation and sulfidation. These parts are presented in chapters four, five, and six, respectively. The overall conclusions drawn from this work are given in chapter seven, followed by several suggestions for continuing work in chapter eight.

CHAPTER II

BACKGROUND

GTD-111 DS is a directionally solidified (DS) nickel-based superalloy that is currently used in land-based turbine engines. As with other superalloys, GTD-111 DS is a precipitation hardenable alloy that has excellent high temperature mechanical properties as well as corrosion resistance. DS materials were developed to increase high temperature mechanical properties by reducing grain boundaries normal to the stress axis or by controlling the casting process to make single crystals.

The production of DS alloys involves casting the metal in a mold such that heat flow is unidirectional. This is achieved by heating the side wall of the mold and extracting heat from the bottom of the mold through a chill plate. Additionally, the mold assembly passes through the furnace at a controlled rate. The resulting microstructure consists of columnar grains which grow anti-parallel to the heat flow, along the $\langle 100 \rangle$ direction for cubic materials [6]. Certain mechanical properties of DS materials are significantly improved over conventionally cast alloys due to the reduction of grain boundaries normal to the stress axis. This increases fatigue life, creep resistance, and provides for higher yield strengths. Thermal fatigue resistance is also enhanced by the preferred $\langle 100 \rangle$ orientation of DS alloys along the solidification direction.

2.1 Microstructure of Directionally Solidified (DS) superalloys

The microstructure of DS superalloys is comprised of primary dendrite stalks roughly parallel to $\langle 100 \rangle$ directions. Slight deviations from $\langle 100 \rangle$ growth direction are usually attributed to anisotropy of the solid/liquid interfacial energy. These primary dendrites are accompanied by secondary dendrite arms that grow perpendicular to the primary $\langle 100 \rangle$ directions. Tertiary arms grow perpendicular to the secondary arms and parallel to the primary arms.

The spacing of the primary arms is fixed once the arms develop and no coarsening of the primary stalks occurs during the remainder of the solidification event [16]. Secondary and

tertiary arms are susceptible to coarsening as the solidification process continues toward completion. Like any coarsening phenomenon, the larger arms grow at the expense of the smaller arms in accordance with Ostwald ripening theory. The result is an increase in the spacing between secondary arms through the elimination of smaller secondary and tertiary arms. Upon the completion of solidification, secondary arm spacing is fixed. Heat treatment temperatures are not sufficiently high to melt the secondary arms and establish a new dendrite arm spacing. The secondary arm spacing can be used to estimate the local solidification time of the directionally solidified alloy if the melting range of the alloy and the cooling rate are known. The secondary arm spacing is proportional to the cube root of the local solidification time [16] and can be used to compare samples from different batches. Assuming similar alloy compositions, materials with similar secondary arm spacings can be assumed to have been produced under similar local solidification conditions for the same compositions.

2.2 Effects of different alloying elements

Table 1 shows the allowable composition ranges for GTD-111 DS. Each element plays a specific role in the formation of the microstructure. For example, Ti and Al partition preferentially to γ'. Heavier elements such as W, Ta, and Mo, partition to the matrix and aid solid solution strengthening [17]. Since the diffusivities of these three elements in Ni are relatively low, coring cannot be completely eliminated during most commercial homogenization treatments. W tends to segregate to the dendrite core, whereas Ta and Ti segregate to the interdendritic channels [17]. A major consequence is that Ta-rich MC carbides are formed in these channels and along grain boundaries.

The presence of these carbides can greatly influence the mechanical properties of the material. Chromium and Al increase corrosion resistance. Aluminum that is not associated with γ' can diffuse to the surface to form a protective Al_2O_3 scale which protects the alloy from further oxidation [17]. However, the formation of this scale is often accompanied by the loss of γ' in the region adjacent to the scale due to the depletion of Al and Ti. Chromium promotes corrosion resistance, but is also responsible for the formation of MC carbides that,

Table 1: Nominal composition range of GTD-111 DS

	Cr	Co	Al	Ti	Mo	Ta	C	Zr	B	Ni
Min	13.7	9	2.8	4.7	3.5	2.5	0.08	0.005	0.005	Bal.
Max	14.3	10	3.2	5.1	4.1	1.7	3.1	0.12	0.04	Bal.

much like $M_{23}C_6$ carbides, are important to consider when examining mechanical behavior. Hafnium is sometimes added to superalloys to control the shape of the carbides. Hafnium forms a stable MC carbide that remains blocky as opposed to the script morphology of the other carbides.

2.3 The strengthening phase γ'

The precipitation of γ' can occur by both continuous and discontinuous reactions. The term discontinuous is related to the fact that there is an abrupt orientation and composition change across the interface between the particles and the matrix. The process is dependent on short-circuit or grain boundary diffusion (Figure 2). The continuous reaction follows classic precipitation of a second phase from a supersaturated matrix and is dependent on volume diffusion in the solid.

The importance of the continuous precipitation reaction in nickel based superalloys is well known since the product precipitates serve as a strengthening agent. The importance of the discontinuous reaction, however, is unclear in these alloys. Mixed reports by several researchers [3, 4, 18, 19, 20] have suggested that discontinuous precipitation can increase ductility while decreasing the tensile strength. This study will attempt to characterize the discontinuous reaction and clarify its role on tensile and fracture behavior of GTD-111.

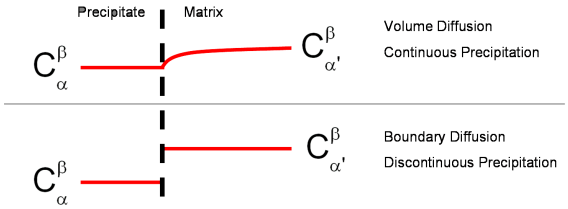

Figure 2: Figure comparing the composition profile across the interface of a reaction dominated by volume diffusion, which is continuous (top) and boundary diffusion which is discontinuous (bottom).

2.3.1 Continuous Precipitation (CP) of γ'

The primary strengthening agent in many nickel-based superalloys is γ' particles [6]. These particles are ordered consisting typically of $Ni_3(Ti, Al)$ with an $L1_2$ crystal structure. Depending on the particle size, volume fraction and temperature during deformation, the particles may be sheared by moving dislocations or looped. The particle size controls the transformation from shearing to looping and is dependent on the volume fraction of γ' and on temperature. As the volume fraction increases, the particle size at which the transformation occurs also increases. It is a general practice to design microstructures that consist of a bimodal distribution of large and small particles to optimize shearing and looping in many superalloys. The evolution of γ', like most precipitates, occurs in three stages: nucleation, growth, and coarsening. Nucleation occurs as γ' precipitates out of a supersaturated solution. Growth of γ' is a diffusion controlled process in which particles become larger as solute is drawn from the super-saturated matrix. The volume fraction of γ' is not constant during either the nucleation or the growth stage. Growth continues until the supersaturation is diminished and the matrix achieves an average solute composition. The composition in equilibrium with each particle is a function of particle size and provides the necessary composition gradient from a small particle to a larger particle that runs the coarsening process.

2.3.1.1 Growth of γ'

Mullins and Sekerka [21] explained the growth of a spherical particle in detail in the mid 1960s. A perturbation placed onto the surface of a sphere can evolve in one of two ways. First, growth can be enhanced by the perturbation reaching out into a solute rich environment. Second, the spherical shape can be restored if the curvature at the interface increases. It was found that a particle must reach a critical size before the perturbation will grow. Below this critical size, curvature is too large and the spherical shape is stabilized [21].

The growth of a cuboidal particle is a diffusion controlled process similar to the case of a spherical particle. However, the concentration of solute surrounding a sphere is radially symmetric. That is, all points along the sphere will see the same amount of solute. A cube

will see higher levels of solute at the corners than at the faces. Protrusions grow out from the particle as a result of these corners being preferentially supplied with solute [22].

2.3.1.2 Coarsening of γ'

Coarsening is a redistribution of solute between particles of different sizes. Redistribution occurs at a constant temperature and constant volume fraction over a given period of time. The driving force for coarsening is the reduction in free energy. The difference in the local composition surrounding particles of different sizes provides the mechanism for this reduction. Figure 3 shows the free energy diagrams for two particles with radii such that r_1 is greater the r_2. The particle with r_2 has a higher free energy and thus has the greatest concentration of solute surrounding it. The result is a flow of solute from smaller particles to larger ones. As coarsening continues, this solute flow eventually leads to the disappearance of the smaller particles. The time needed to complete the first two stages varies from long times for some systems to approaching spontaneity in other systems.

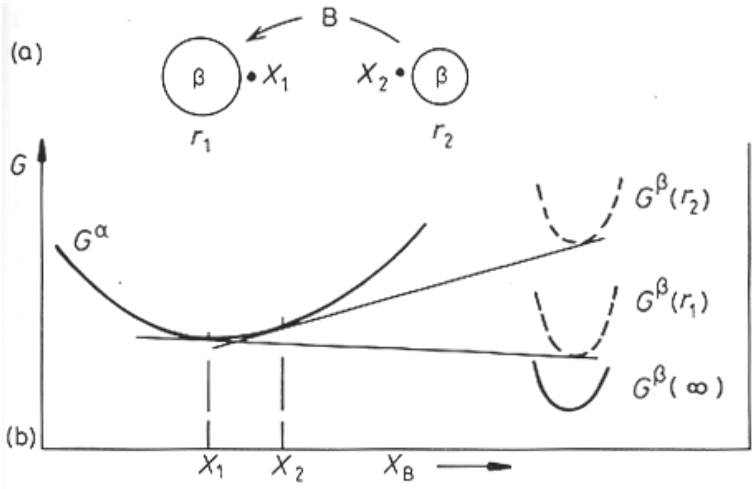

Figure 3: Free energy diagram illustrating particle coarsening. Particle r_2 has a higher free energy and higher solute concentration [2].

During coarsening, the size and shape of γ' particles depends on interfacial energy, antiphase boundary energy, surface tension and elastic strain energy that is present due to a mismatch (δ) between the precipitate and matrix phases. All of these factors are controlled by composition. The partitioning of different alloying elements to either the matrix or γ'

affects the lattice parameters that can result in mismatch and is responsible for an increase in elastic strain energy as misfit increases. Small additions of elements to either phase can cause changes in lattice parameters a_γ and $a_{\gamma'}$. For example, Ti and Ta segregate to γ and γ' [17]. Titanium can increase a_γ up to 0.00042 nm/at% and $a_{\gamma'}$ up to 0.00025 nm/at%. Likewise, Ta can increase a_γ up to 0.00016 nm/at% and $a_{\gamma'}$ up to 0.00025 nm/at%. δ can be calculated from known values of a_γ and $a_{\gamma'}$ using the following equation [17]:

$$\delta = 2\frac{a_\gamma - a_{\gamma'}}{a_\gamma + a_{\gamma'}} \tag{1}$$

It is also possible to empirically estimate the change in mismatch ($\Delta\delta$) as a function of overall composition using x-ray diffraction measurements. An example is given in the equation below [17]:

$$\Delta\delta = -10 - 3(4.6Al + 1.7Mo + 2Ti + 0.9(W + Cr) + 0.5Ta \tag{2}$$

As the mismatch between the two lattice parameters increases, the driving force for coarsening becomes greater. Also, shape transitions occur as the misfit increases from spheres to cubes, doublet of plates, octets of cubes, and finally, thin plates. The transition as a function of particle size and misfit is depicted in Figure 4.

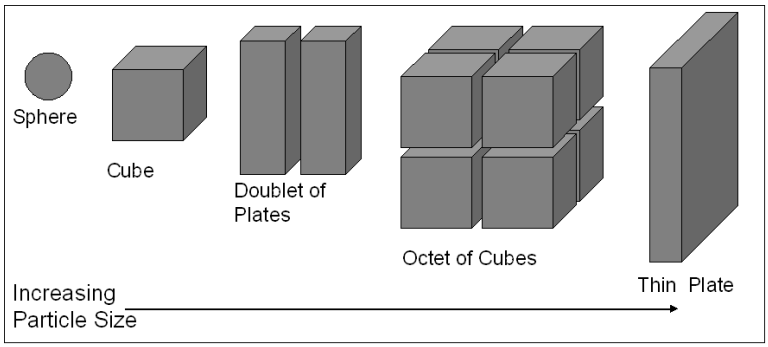

Figure 4: Equilibrium shape of γ' in nickel based superalloys

According to Khachaturyan [23], in Ni-Al systems the shape of γ' can be related in terms of free energy (ΔF) such that there are two competing factors, interfacial tension (σ)

and elastic free energy (ΔE_C):

$$\Delta F = \Delta E^c + \sigma S \tag{3}$$

where S is the surface energy of the precipitate and the elastic energy is given by:

$$\Delta E^c = E_1 V \frac{(4I_1 + 54\Delta I_2)}{(3c_{11} - 2\Delta)} \tag{4}$$

where I_1 and I_2 are dimensionless geometric integrals that depend on the shape and distribution of particles. Δ is an anisotropy factor given by:

$$\Delta = c_{11} - c_{12} - 2c_{44} \tag{5}$$

where c_{11}, c_{12}, and c_{44} are elastic constants. V is the volume of the precipitate. And E_1 is the modulus given by:

$$E_1 = \frac{-0.5\beta^2 \Delta \epsilon_0^2}{c_{11}(2c_{11} - \Delta)} \tag{6}$$

β is the bulk modulus as given by:

$$\beta = c_{11} + 2c_{12} \tag{7}$$

At small particle sizes, σ dominates and leads to the formation of spheres and cubes. As particle size increases, elastic strain energy dictates that cubes are less favorable and octets are formed. The critical radius (r_0) and critical spacing of these particles at which this transformation takes place can be determined using numerical methods. Since coarsening occurs at nearly constant volume fractions, there is an increase in the separation between particles as the radii increase. The particles in turn separate into an octet of smaller cubes rather than forming one large cube when the separation reaches a critical value [23]. In terms of antiphase boundary energy, the separation of cubes to octets is a simple case of energy minimization.

An antiphase boundary (APB) is formed when the lattice registry is not identical when two ordered particles coalesce. Figure 5 shows the formation of an APB in Cu_3Au, another $L1_2$ crystal similar to γ'. Typically, a single ordered particle that contains an APB will separate into two ordered particles of equal area if the APB energy $> 2\sigma$, where σ is the interfacial energy. Under this condition, a single APB will have a higher energy and will

be less favored. The result is the formation of two new γ/γ' interfaces that have a lower energy.

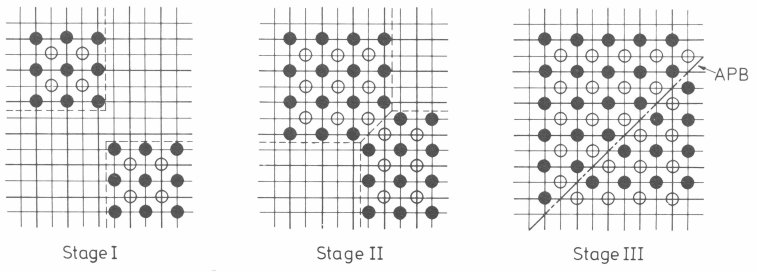

Figure 5: Formation of an antiphase boundary in Cu_3Au where Cu and Au are represented as black and white circles respectively [2].

A model by Wang *et al.* [24]is capable of predicting this behavior by defining four different ordered domains that occur during $L1_2$ ordering. The model defines particles of like compositions, which have good lattice registry, as being in-phase and those of dislike compositions to be out-of-phase. APBs are formed when two out-of-phase particles coalesce [24]. The model shows the decomposition of a single particle into two new particles based on the minimization of energy. The model is also able to predict that the inverse of this process occurs if two in-phase ordered particles begin to coalesce. The particles first join at corners and then grow into one ordered particle without an APB.

The models of Wang and Khachaturyan [24, 23] offer ways to examine the shape transition of only a few γ' particles as a function of free energy. However, the models yield no larger scale information such as the average radius of all particles as a function of time. If it is assumed that the volume fraction of γ' is negligible and that there is no elastic interaction between particles, a simpler model developed by Lifshitz and Slyozov (1961) [25] and Wagner (1961) [25] [LSW], may be applied. LSW theory predicts that the variation of the average radius of coarsening particles as a function of time can be related as:

$$\overline{r}_t^3 - \overline{r}_0^3 = \frac{8D_\sigma V_m t}{9RT} \tag{8}$$

where t is time, T is temperature, D is the diffusion coefficient, γ is the interfacial energy,

N_σ is the chemical solubility, and V_m is the molar volume. The distribution of particles predicted by this method was found to have a maximum particle size of $R = 1.5r$. Therefore, particles larger than $1.5r$ will not be observed after a significant amount of coarsening has occurred [25]. Low values of one, or a combination, of the parameters D, γ, and N_σ will decrease the amount of coarsening experienced by the particles. Alloys are often designed to have reduced interfacial energies. However, lattice mismatch is found to decrease as interfacial energy is lowered. This allows low energy shapes, such as spheres, to exist at particles sizes that are larger than in cases where mismatch is high [22].

Ardell investigated the effects of volume fraction on LSW theory. To modify the assumption that the volume fraction of γ' is not negligible, a parameter *k(fv)* is added to the equation above such that the equation (8) becomes:

$$\overline{r}_t^3 - \overline{r}_0^3 = \frac{8k(fv)D_\sigma V_m t}{9RT} \tag{9}$$

k(fv) depends solely on the volume fraction of the particles and is used to ensure that the coarsening rate will increase with increased volume fractions. A review of this modification found large amounts of scatter when the coarsening rate is plotted as a function of volume fraction for $Ni - Ni_3X$ materials. Experimentally, the dependence of coarsening rate on volume fraction was not supported in many Ni-Al alloys [25]. However, the effect of volume fraction on Al-Li alloys is well pronounced. These mixed results suggest that coarsening in systems with finite volume fraction is complex and is still not completely understood.

2.3.1.3 Gamma Prime (γ') shapes resulting from coarsening followed by growth at higher temperatures

Cubic γ' precipitates with extended corners are often observed. This can be due to increase in temperature when the material is in the coarsening stage. During coarsening, cubes and octets of cubes are formed according to their interfacial energy, antiphase boundary energy, surface tension and elastic strain energy as discussed above. If this coarsened microstructure is then re-heated, some of the γ' can be dissolved and taken back into solution, which

supersaturates the matrix. Since there is now a degree of supersaturation, growth may reoccur when the temperature decreases. Following Mullins and Sekerka [21], the cubes formed during coarsening will now grow through the extension of the corners. The growth of these extensions will ultimately lead to a dendritic shape of the γ' particles. In addition, small spherical particles may also grow upon cooling from the elevated temperature. The importance of this is that microstructures observed at room temperature may not be identical to those at test temperatures. For example, a specimen tested at 871°C (1600°F) may develop small spherical particles as it cools from the test temperature. At 871°C (1600°F), having more solute and fewer particles affects the mechanical properties. Therefore, care should be taken when considering the existence of small spherical particles at room temperature compared to their existence at elevated test temperatures.

2.3.2 Discontinuous Precipitation (DP) of γ'

Discontinuous reactions have been widely studied in systems such as Pb-Sn, Al-Zr, and a variety of superalloys. The evolution of this research over the past thirty years has been summarized by Williams and Bulter [3] in the 80's, and most recently by Manna *et al.* [4] in 2003. For consistent terminology, both reviews use the method first proposed by Thompson [3] that divides discontinuous reactions into three types. Figure 6 summarizes the reactions in terms of their equations and resulting structure. Type 1 involves a lamellar structure growing from a supersaturated matrix in which no continuous precipitation is occurring. Type 2 involves the same structure except that continuous precipitation now takes place in the matrix. (Note: in types 1 & 2 reactions the discontinuous and continuous γ phases are identical). For type 3 reactions, the discontinuous products are comprised of a third phase, δ, that is different from the matrix and continuous precipitates. This is commonly observed as $M_{23}C_6$ carbide formation in steels and superalloys. For this study only types 2 and 3 are observed and will be considered.

2.3.2.1 Initiation of discontinuous γ' precipitation

Possible initiation sites for discontinuous reactions include grain boundaries, which are the most favorable due to their high diffusivity, and other free surfaces such as matrix/precitpate

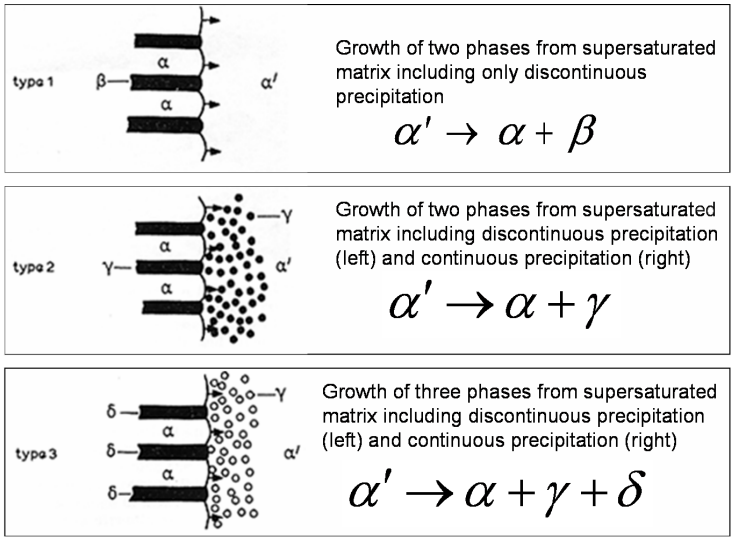

Figure 6: Thompson's categories for discontinuous precipitation [3].

boundaries. Two classic initiation mechanisms include Tu and Turbull's pucker model [26] (Figure 7) and Nes and Biddal's model (Figure 8)for fan growth [3]. The pucker model involves grain boundary deflection when a precipitate is formed. The deflection is an attempt to maintain a small interfacial energy after the precipitate is formed. The final discontinuous structure is formed after several cycles of this process.

The fan structure explained by Nes and Biddal [3] involves precipitation nucleation on a boundary. As the precipitate grows, the boundary moves forward and new precipitates form on either side of the cusp (Figure 9). As growth continues, there is a branching of the initial precipitates to minimize the interface energy. The growth direction of the fan can either be in one direction away from the boundary or in both directions. Figure 19 shows the S-shape mechanism proposed by Fournelle and Clark [3].

Some attempts have been made to relate aging temperature to the occurrence of 1-D and 2-D growth (Figure 11). In general, if the aging temperature is greater than half the melting temperature, then growth is in one direction. Likewise a relationship is such that if the aging temperature is less than half the melting temperature, 2-D growth is favored. These relationships are very general and are not without exceptions. The S-mechanism by Fournelle and Clark assumes that the initiation boundary is S-shaped. This configuration

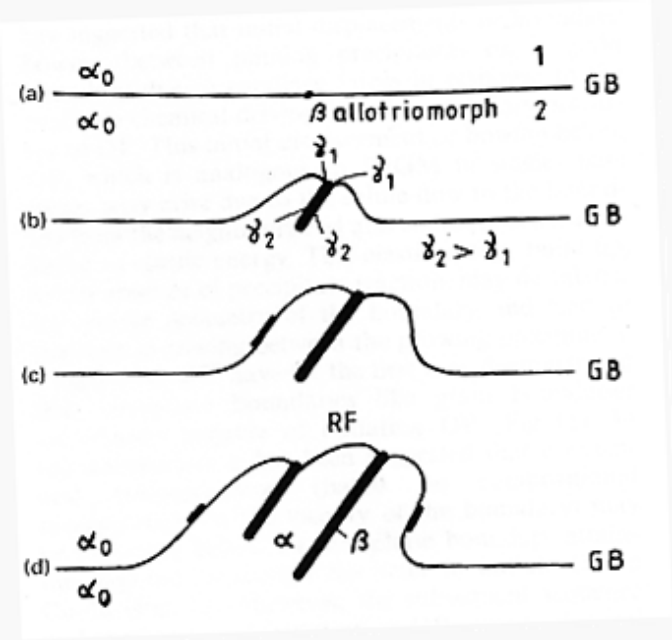

Figure 7: Tu and Turnbull's pucker model of discontinuous precipitation [3].

is highly unlikely as curved boundaries are unfavorable in fully solutionized alloys.

In the case of type 2 dubbed by Manna [4] as discontinuous coarsening (DC), the initiation site is the boundary between the matrix and eutectic structures often found in grain boundaries. Figure 12 shows how the lamellar eutectic structure becomes larger as discontinuous coarsening progresses. A study involving Inconel 713 has shown that discontinuous reactions can be suppressed by changing the casting condition to eliminate the eutectic, the initiation site for DC, formed during the end of solidification.

2.3.2.2 Driving Forces

In terms of free energy, William and Butler [3] have proposed that the variation in free energy for initiation of discontinuous precipitation is given by:

$$\Delta G_I = \Delta G_P + \Delta G_{GB} + \Delta G_D + \Delta G_\epsilon \tag{10}$$

where P,GB,D, and ϵ relate to precipitation, grain boundary, deformation, and strain energy contributions to free energy, respectively. For growth during DP, the free energy is comprised

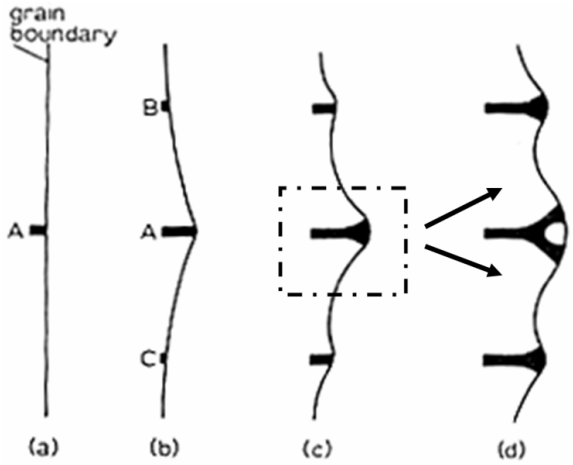

Figure 8: Nes and Billdal's model for fan growth. The initial precipitate branches to reduce the interfacial energy (c) [3].

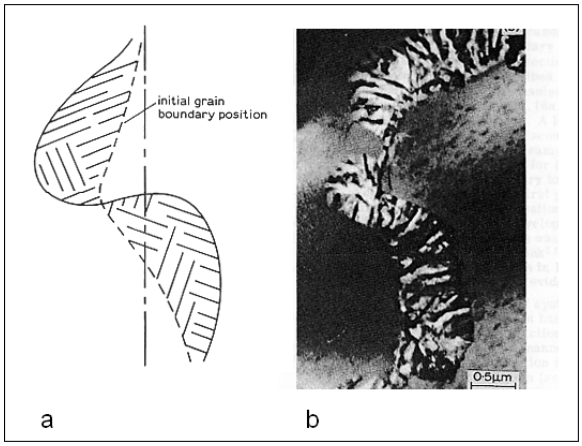

Figure 9: Tu and Turbull's model for growth in both directions (a) and experimental observation in a Pb-Sn bicrytsal (b) [3].

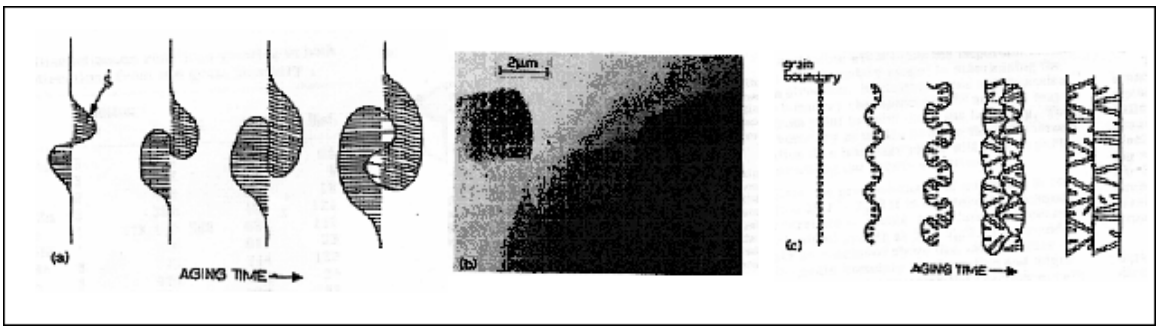

Figure 10: Fournelle's S-mechanism (a), as observed in Al-Li (b), and Frebel and Schenk's modification of the S-mechanism (c) [3].

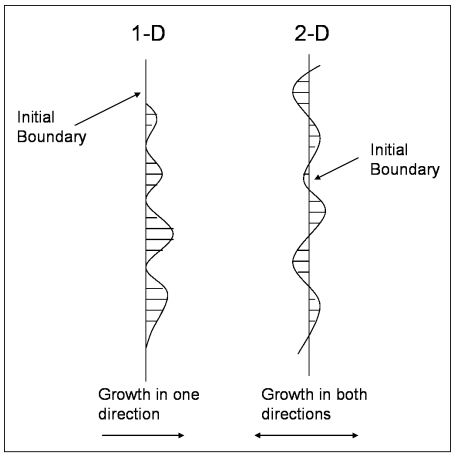

Figure 11: Examples of 1-D and 2-D discontinuous growth. The 1-D case involves cellular structure growing outwardly from the grain boundary in only one direction. In the 2-D case, however, there is growth outwardly on the sides of the grain boundary. [3]

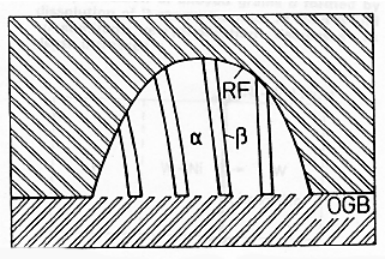

Figure 12: Schematic of discontinuous coarsening of existing eutectic lamellae into a new structure with a larger lamellae spacing [3].

of two terms, the chemical free energy (ΔG^C_{DP}) and the interfacial energy, (ΔG^γ_{DP})

ΔG^γ_{DP} is given by:

$$\Delta G^C_{DP} = RT(X_0 ln\frac{X_0}{X_{AV}} + (1 - X_0)ln\frac{1 - X_0}{1 - X_{AV}}) \tag{11}$$

Where X_0 and X_{AV} are the compositions of parent phase and the precipitate phase, respectively [3].

Using this expression one can see that the driving force for DP is inversely proportional to temperature. The upper bound for temperature T_{DP} has been defined as the highest temperature at which DP occurs and can be experimentally determined using the lamellar

spacing, λ [4]. T_{DP} is below the solvus temperature and it has been found that a temperature hysteresis is observed between discontinuous precipitation and a process called discontinuous dissolution.

Discontinuous dissolution involves a lamellar structure returning to a supersaturated matrix phase (Figure 13). The lowest temperature at which dissolution occurs is denoted as T_{CR}. Figure 14 shows the hysteresis with respect to temperature and the reaction front velocity. Note that T_{DP} is not equal to T_{CR}. At temperatures at or near the solvus temperature, volume diffusion affects dissolution by suppressing discontinuous dissolution altogether since at the solvus all precipitates, including those continuously precipitated, will be taken into solution. The implication of this is that dissolution at temperature around T_{CR} can be used to eliminate the discontinuous structure without altering the continuously precipitated phase.

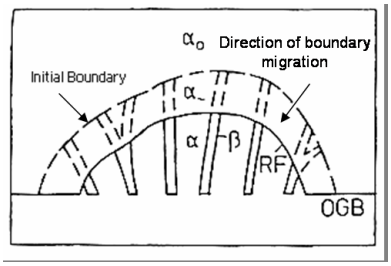

Figure 13: Schematic of discontinuous dissolution. The dashed line shows the initial boundary of the structure. As the structure dissolves, the reaction front (solid line) moves toward the original grain boundary [3].

Since figure 14 relates to the reaction front velocity v, it is helpful to mention that the velocity of the reaction front can be estimated by determining the spacing between lamellae, λ, in the DP structures.

2.4 Interdendritic structures

The interdendritic region is comprised of carbides as well as products of discontinuous precipitation. These phases are largely associated with mechanical properties such as fatigue life and tensile strength. They may help retard crack growth, as in the case of DP products, or initiate cracks in the case of carbides. It is crucial to understand the formation, evolution,

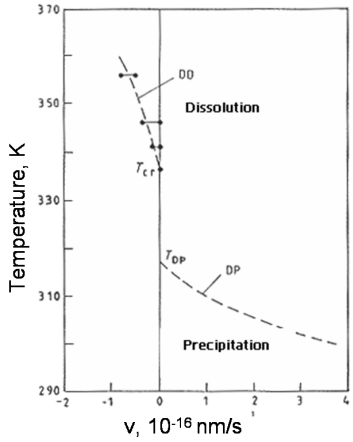

Figure 14: Hysteresis with respect to temperature and the reaction front velocity for a Pb-Sn alloy [4].

and mechanical roles of these features to study mechanical properties.

2.4.1 Carbides

Ta-rich MC carbides are considered to be primary carbides that form during solidification of the alloy. Cr-rich $M_{23}C_6$ are secondary carbides that form from the degeneration of the MC carbides at temperatures between 760°C (1400°F)- 980°C(1796°F) [27]. It was originally suggested that the degeneration of MC proceeded according to the following equation.

$$MC + \gamma \rightarrow M_{23}C_6 + \gamma'[6][27] \tag{12}$$

However, a recent paper by Lvova and Norsworthy [28] suggests that γ' is too chemically dissimilar from MC carbides to be a reaction product. A new mechanism has been proposed in which a degenerated MC gives up carbon, which combines with the Cr in the matrix to form products of secondary carbides and a carbon deficient MC phase ($MC_{deg.}$) This irreversible reaction is written:

$$MC + \gamma \rightarrow M_{23}C_6 + MC_{deg}[28] \tag{13}$$

The significance of these reactions is that when MC carbides degenerate, continuous chains of brittle $M_{23}C_6$ form, making crack propagation easier. Since the process is dependent on the diffusion of carbon the reaction is more favorable at grain boundaries, which is also the preferred path for crack growth.

2.4.2 Discontinuous Precipitation Products (DPP)

It has been observed in several studies that these DPP are more ductile than the matrix. Frebel and Otte [29] have suggested that these structures may be detrimental to high temperature properties of DS Sn-Pb alloys. Scarlin [19] examined this in superalloys and subsequent work by Gasko, Janowski and Pletka [30] found that as the amount of DPP decreases, the yield strength of specimens increases while overall ductility decreases. It has been generally concluded that the presence of the DPP helps to retard crack growth by making the path more tortuous. Therefore, the absence the eutectic phase makes it easier for the carbides or other casting defects to initiate cracks which grow to a critical size and cause failure [18]. Fatigue life also decreases as the amount of eutectic phase decreases [31]. Additionally, DPP have been found to lead to passivation breakdown in steels since elements that usually form protective layers are tied up in the precipitate phase. The result of the breakdown leads to crack formation in regions around the DPP [32].

2.4.3 Interdendritic failure

Fracture paths in DS alloys can lead to some confusion over what distinguishes interdendritic failure from intergranular failure. The problem arises in that all intergranular failures are interdendritic. The reverse is not necessarily true. So what then identifies failure as being intergranular? A grain can be defined as a collection of primary dendrites that share a common orientation in the transverse plane. A grain boundary exists between collections of different orientations. Each grain is made up of similar interdendritic features, often making it difficult to distinguish these boundaries using standard techniques. The answer may be found in the use of electron backscattered diffraction (EBSD) techniques in which grains can be mapped based on orientation. The fracture paths can also be altered by changing the DPP volume fraction. In conventionally cast alloys, tensile crack paths have often been

observed following interdendritic DPP. Studies show that at lower volume fractions of DPP, the path changes from an interdendritic path to a grain boundary path. In DS materials a similar effect should be seen in longitudinally (the loading axis is parallel to the columnar grains) loaded specimens [18].

2.5 Corrosion

Any study of the high temperature materials used in land-based turbine engines would be incomplete without discussing corrosion. Two important corrosion problems that are typically encountered include oxidation and, in the case of Integrated Gasification Combined Cycle (IGCC), attack from H_2S gas.

2.5.1 Steam Turbines

Oxidation is a major corrosion factor in steam turbine components. The formed oxides can lead to crack initiation and failure either through oxide layer spallation and/or oxide spiking in which oxide fingers penetrate into the alloy. An excellent starting point for studying oxidation of complex commercial nickel superalloys is the ternary Ni-Cr-Al system. This system has been extensively studied by Giggins and Pettit [5] who have shown that, depending on composition, these alloys can be sorted into three groups, which are shown in Figure 15. Group I alloys form an outer layer of NiO under which is a subscale comprised of both Al_2O_3 and Cr_2O_3. Group II is characterized by an outer scale of Cr_2O_3 which may be accompanied by subscale internally oxidized (Al_2O_3). Group III alloys have one continuous outer layer of Al_2O_3. Alloys such as Rene 80, Inconel 718, and GTD-111 all belong to group II [6, 7].

Figure 16 shows the typical microstructure of oxidized Inconel 718. There are four clear regions in the figure. These include a Cr_2O_3 scale, internally oxidized Al_2O_3 particles, a γ' free zone, and the base alloy consisting primarily of γ' precipitates in a γ matrix. The Al_2O_3 and Cr_2O_3 oxides form due to the diffusion of O_2 from the surface as well as the outward diffusion of Cr and Al. The formation of the outer Cr_2O_3 eventually limits diffusion of O_2 which serves to protect the alloy from further oxidation. The lack of continuous O_2 is also the reason why the Al_2O_3 sub scale remains as isolated particles rather than forming

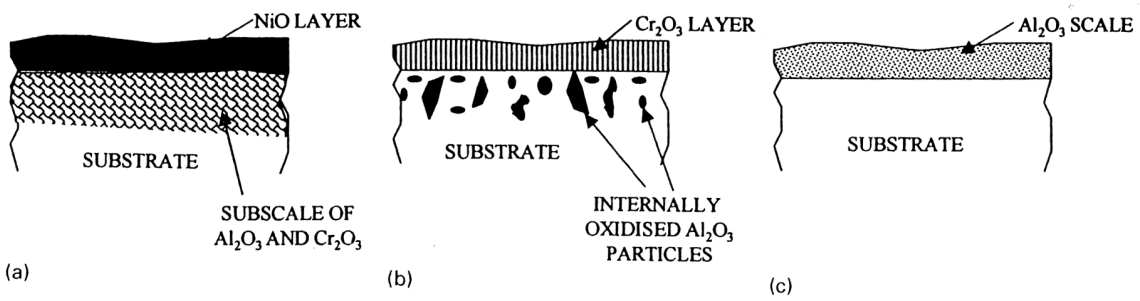

Figure 15: Diagram of groups 1 (a), 2 (b), and 3(c) as described by Giggins and Pettit for the Ni-Cr-Al system [5].

a second continuous layer. The γ' free zone is formed as the local Al concentration drops below the concentration needed to form γ' precipitates.

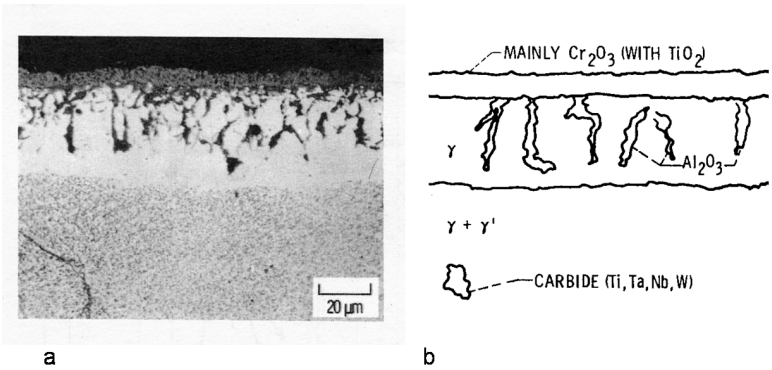

Figure 16: Micrograph (a) and schematic(b) of Inconel 718 [6]

The formation of a protective passive layer can be tracked by measuring the growth of oxide layers as a function of time and temperature. The various oxidation behaviors include linear, parabolic, and exponential. Parabolic behavior is indicative of formation of a protective layer. Several group II alloys, including Inconel 718 and GTD-111, are known to gain weight parabolically as oxidation continues. Cheruvu [33] has compared these two alloys and found that GTD-111 is less resistent to oxidation due to its poor scale adherence which causes spallation. Additionally, at temperatures greater than 1000°C, the Cr_2O_3 layer can evaporate causing further corrosion damage which further complicates oxidation in steam turbines.

2.5.2 Integrated Gasification Combined Cycle Turbines (IGCC)

In the case of IGCC engines, corrosion of superalloys is complicated by the addition of syngas, the product of coal gasification. Syngas is quite corrosive as it is comprised of large amounts of H_2S and coal particulates. For laboratory experiments, the syngas can be simulated using N_2 with 100 ppm H_2S. In reality, the coal particles add a large wear factor to corrosion rate that cannot be currently addressed. Sulfur attack in superalloys is far more aggressive then oxygen attack as is seen in Figure 17 which shows that rates of corrosion in sulfur are often orders of magnitude greater than those in O_2. The reasons for this are summarized by Khanna into five points [7]:

1. Higher diffusion rates
2. Low melting eutectic formation
3. Low solubility
4. Similar energies of formation
5. High dissolution pressure

Environment	*Parabolic rate constant (Kp) $gm^2cm^{-4}s^{-1}$*			
	Ni	*Co*	*Fe*	*Cr*
Oxidation	9.1×10^{-11} 1000°C	1.6×10^{-9} 950°C	5.5×10^{-8} 800°C	4.5×10^{-12} 1000°C
Sulphidation	8.5×10^{-4} 650°C	6.7×10^{-6} 720°C	8.1×10^{-6} 800°C	8.1×10^{-7} 1000°C

Figure 17: Rate constants for various metals [7].

CHAPTER III

CHARACTERIZATION OF DIRECTIONALLY SOLIDIFIED (DS) GTD-111

3.1 Introduction

A typical turbine blade made of GTD-DS is shown in Figure 18. The blade has been etched to reveal the directionally oriented grains. Figure 19 shows a common slab of GTD-111 DS that is representative of the material studied in this work. Results of both grain size and secondary dendrite arm spacing measurements (SDAS) of the turbine blade and slab C19-1801 are summarized in Table 2.

Table 2: Grain size and secondary dendrite arm spacings measurement of GTD-111 DS.

Sample	Grain Width (cm)	Grain Length (cm)	SDAS (μm)
Bucket	0.58 ± .07	17.25 ± 3.1	104.7 ± 9.3
slab C19-1801	0.51 ± .06	13.97 ± 2.00	104.1 ± 6.8

The grain dimensions were measured directly from the macro-etched bucket and slab. The SDAS was measured using polished metallographic samples using stereographic techniques outlined by Gokhale *et al.* [34] The average grain widths and lengths as well as SDAS's are similar between the slab and the bucket. It can then be assumed that the local solidification conditions including local solidification times are similar in accordance with theory suggested by Kurtz [16].

3.2 SEM metallography on bulk material

Metallographic samples were polished using silicon carbide papers through #4000 grit, followed by 1 μm alumina suspensions. An etchant consisting of 60% Lactic acid, 38% Nitric acid, and 2% Hydrofluoric acid was then used to reveal the microstructure. Analysis was performed using both optical and scanning electron microscopy to quantify microstructural features such as volume fraction of γ', carbides and discontinuous precipitation products

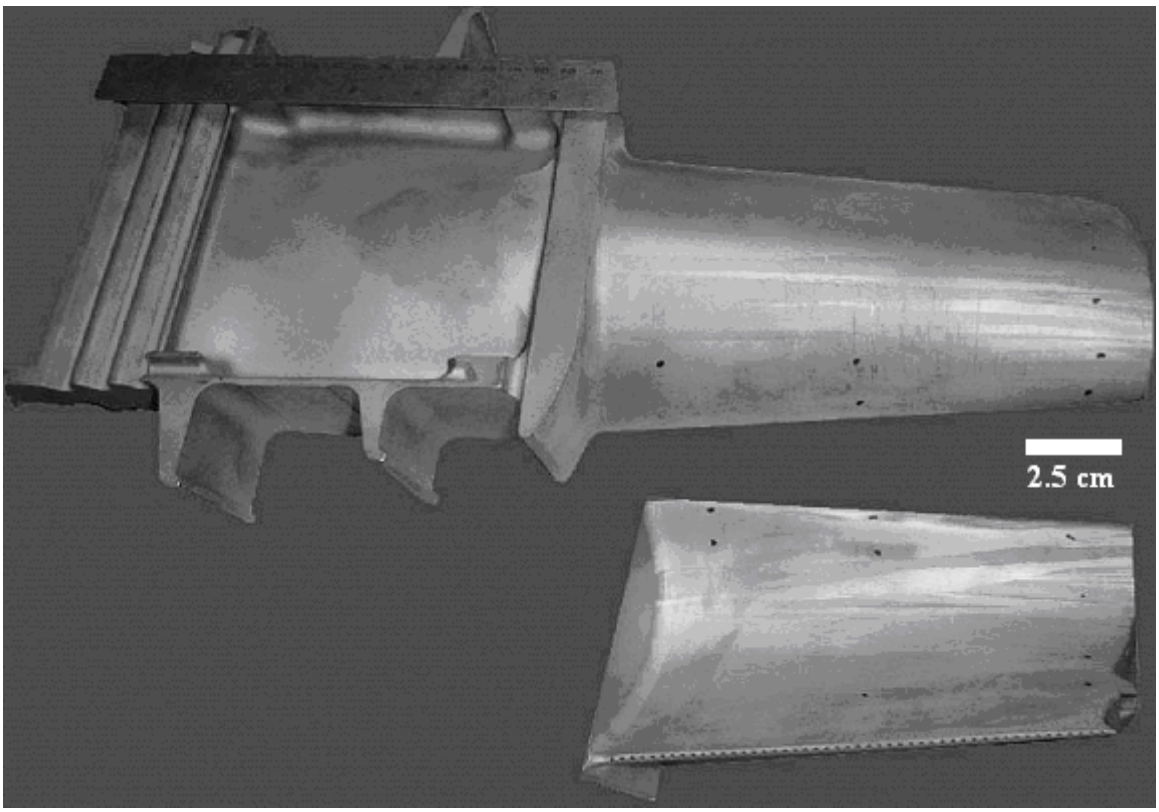

Figure 18: Image of macro-etched bucket provided by GE.

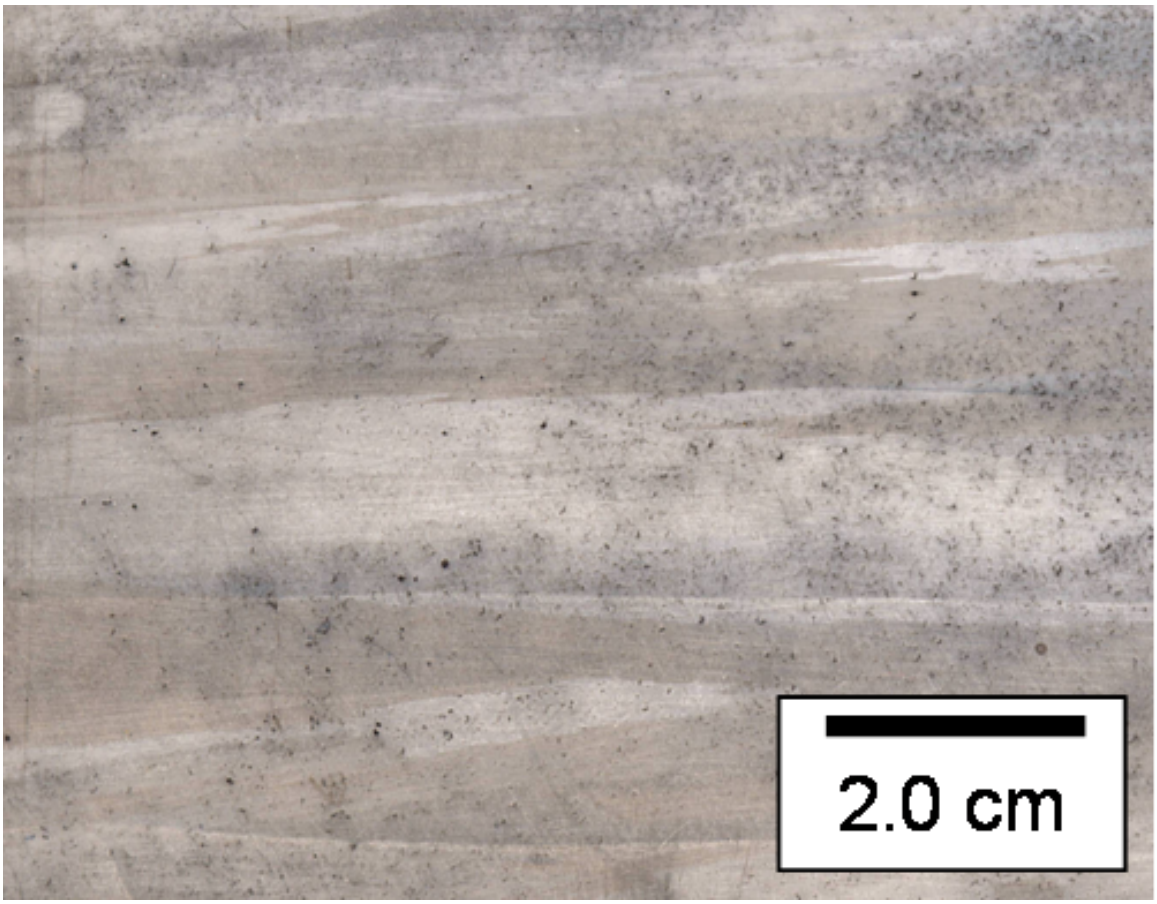

Figure 19: Image of macro-etched slab provided by GE.

(DPP). It is important to note that while most authors simply refer to these products as eutectics, it is unclear that they indeed formed from the liquid (eutectic-like is perhaps a better term). As a result, the term DPP will be used. Figure 20 shows optical micrographs of heat-treated GTD-111 DS and material from a retired turbine blade. A highly cored dendritic microstructure is observed. The variation in contrast corresponds to differences in both the size and distribution of γ' precipitates. The volume fraction of γ' was found to vary between 50-60%. The particles in the dendrite cores are small and spherical with a size of 0.1 μm. As the distance out from the core is increased, the particle size increases to 1.0 μm and the shape changes to octets (see figure 44). The γ' in the interdendritic region is much larger and in the form of a γ/γ' DPP, which is commonly observed in superalloys. This is in agreement with other studies that have found similar microstructural features when characterizing GTD-111 [35, 36].

The image analysis software package Image Pro Plus was used to determine the volume fraction of carbides and DPP. The volume fraction of carbides was found to be less than 2.0%. The volume fraction of DPP was found to be 6%. There does not appear to be any significant changes in the volume fraction or shape of the DPP across the samples from the as-cast to bucket material. This would suggest that their properties are solely dependent on the casting conditions. Figure 22 shows an example of two DPPs in an as-cast sample. It appears that the growth direction occurs on both sides of the boundary. Further examination is needed to determine the true nature of the growth direction.

Both MC and $M_{23}C_6$ carbides have been identified using scanning electron microscopy techniques, although MC carbides are more abundant. An EDS detection system identified the Cr-rich carbides and Ta-rich MC carbides. Carbides at or near the surface of samples can expand upon heating. This expansion either by itself or in conjunction with oxidation can serve as a crack initiation mechanism [37].

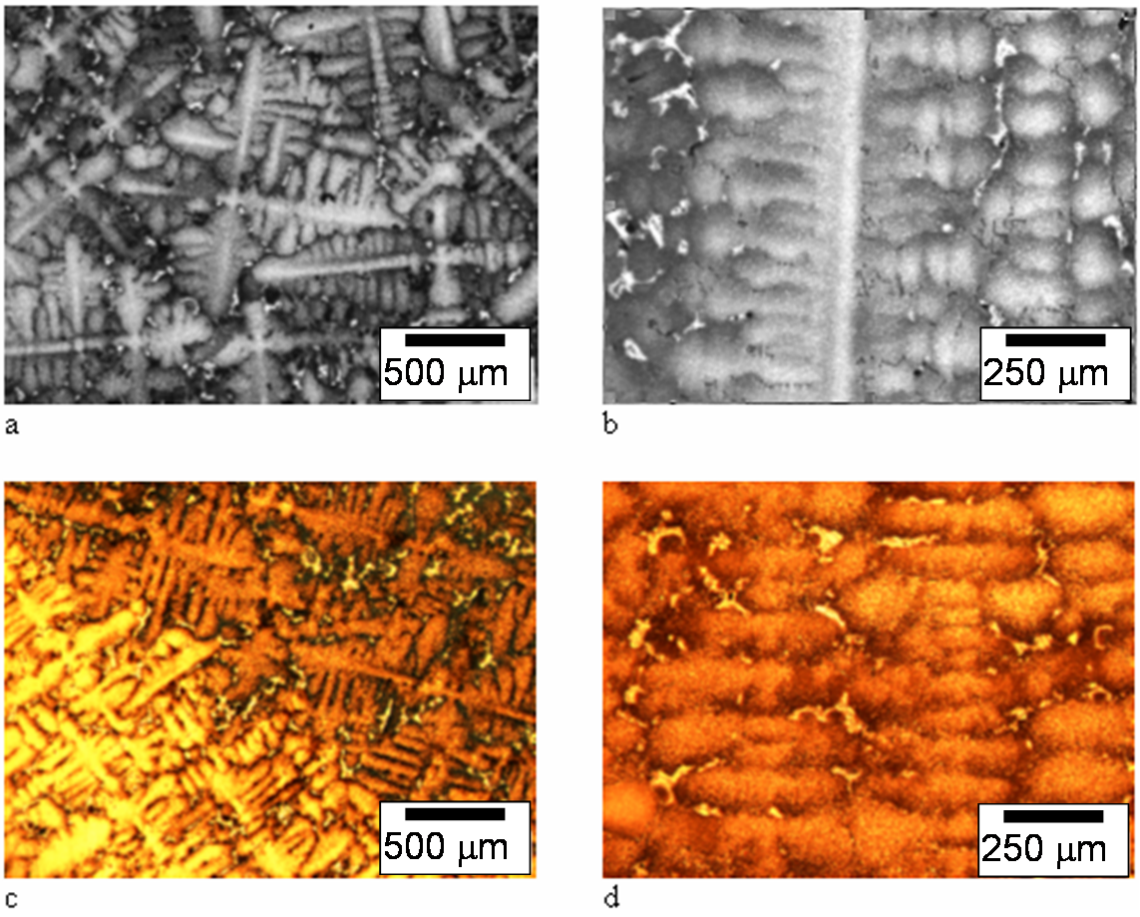

Figure 20: Optical micrographs of as-received GTD-111 (a,b) and root section (c,d).

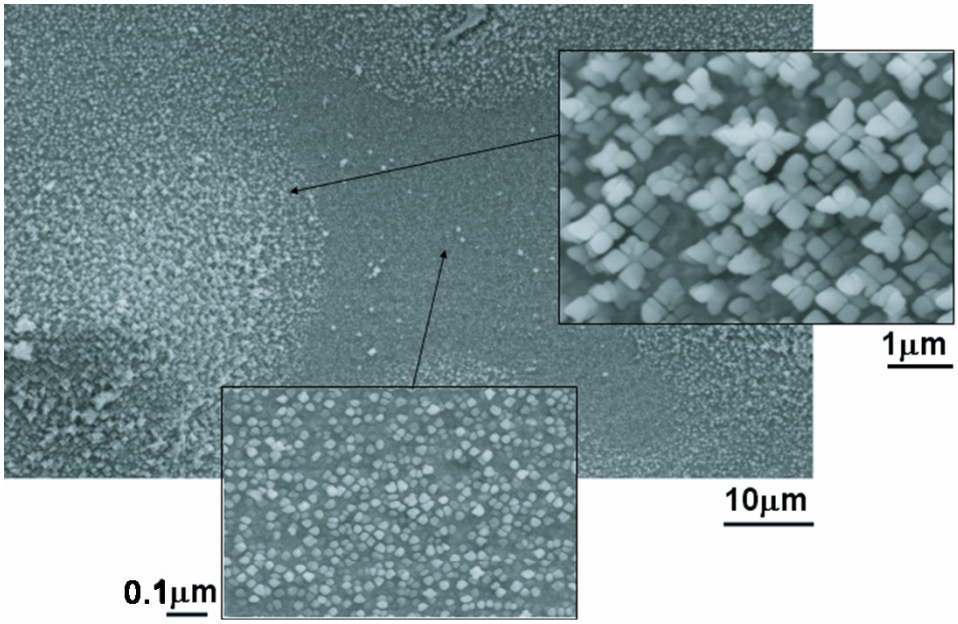

Figure 21: Cored dendrite structure from as-cast GTD-111.

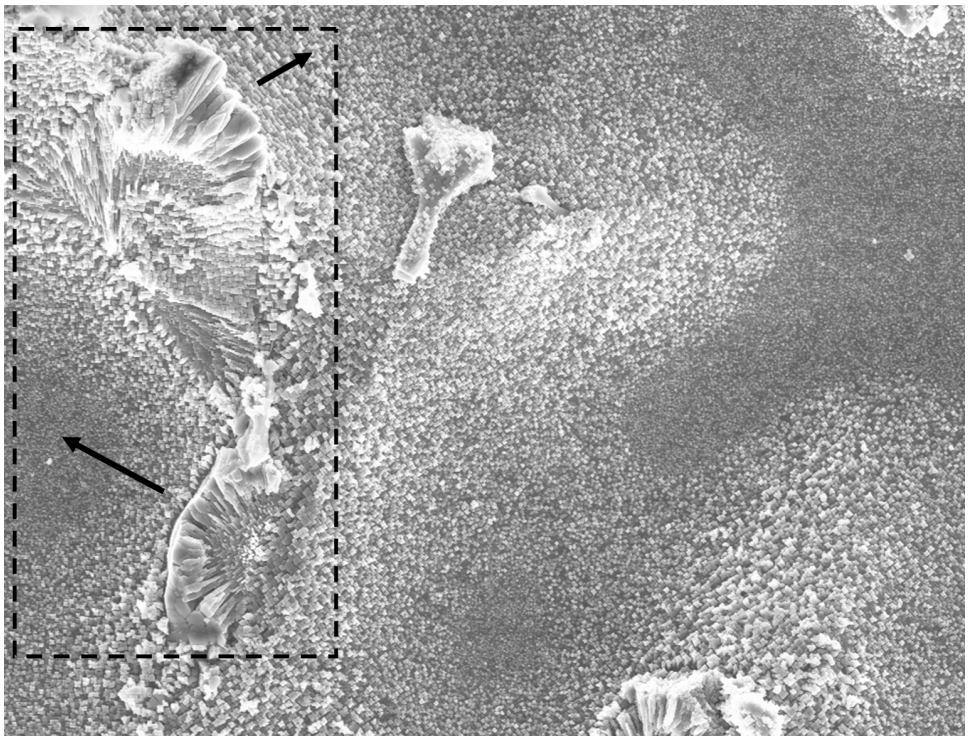

Figure 22: Discontinuous structures from as-cast GTD-111. The arrows show the growth directions of the structures.

CHAPTER IV

MECHANICAL PROPERTIES AND FRACTOGRAPHY

This chapter will discuss quantitative metallographic and fractographic methods that were used to determine that the fracture path during tensile tests of GTD-111 DS superalloy as influenced by the presence of (Ti,Ta)C carbides. Combined profilmetric and confocal microscopic techniques were used to determine the true surface areas of the fracture surfaces of both longitudinally and transversely oriented tensile specimens. The results show that the true area fraction of carbides on the longitudinally oriented fracture surfaces of specimen tested over a range of temperatures is up to five times greater than the bulk volume fraction of carbides in the material. The transverse case also shows higher area fractions than the bulk material, although to a lesser extent. The results show that the longitudinal samples exhibits a stronger preference to failing at carbides when compared to the other orientation. Additionally, the carbides were observed to fail by cracking rather than debonding from the matrix phase.

4.1 Background

4.1.1 Mechanical tests

Tensile tests were conducted by Ibanez [8] at several temperatures ranging from room temperature to 871°C (1600°F). The tests were given the designations LT and TL. The LT designation refers to the longitudinal orientated specimens (L) in which the loading axis was parallel to the columnar grains. Crack growth in the LT designation was such that growth occurs in the transverse (T) direction which is perpendicular to the columnar grains. The TL label refers to the transversely (T) oriented specimens that are loaded perpendicular to the columnar grains. Crack growth in these specimens is longitudinal (L), parallel to the columnar grains [8]. Figures 23 and 24 show the plotted results of yield stress, ultimate tensile stress and final elongation, versus temperature respectively. Both the yield strength and ultimate tensile stress show a maximum around 760°C (1400°F). This has been observed

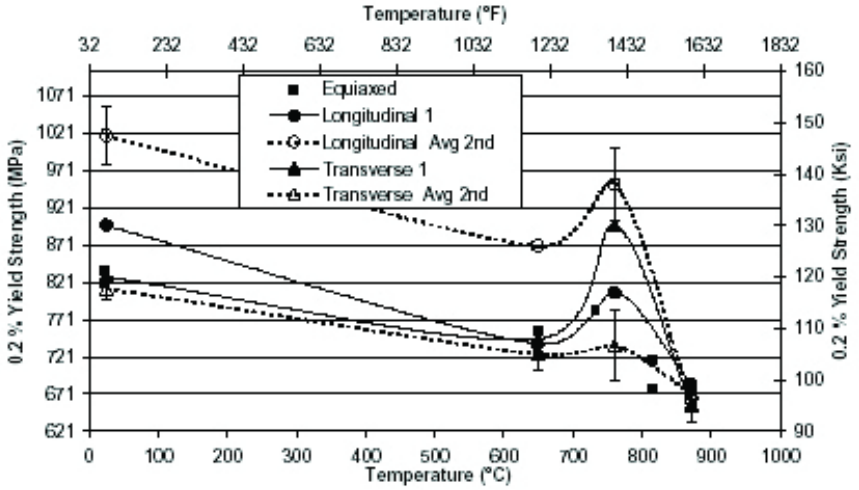

Figure 23: Yield Strength as a function of temperature for the different batches of DS GTD111 in the longitudinal and transverse orientations [8].

in other DS superalloys [20].

It has been suggested that the increase in strength, , with increasing temperature, dubbed as anomalous behavior, is attributed to the high ($> 50\%$) volume fraction of γ' [38] as γ' experiences an increase in strength as temperature is increased as shown in Figure 25. The strength gain is attributed to a change in deformation mechanisms from octahedral slip of the precipitate phase, γ', at temperatures below 600°C to cubic slip at temperatures greater than 600°C [38].

The fracture surfaces of each specimen were analyzed using a scanning electron microscope equipped with a backscattered electron detector. To determine if the crack showed any preference to a certain phase, such as carbides, a random plane beneath the fracture surface was sectioned and polished for each sample and stereographic measurement were made to determine the area fractions of each phase.

Calculated values of fracture toughness (tests also conducted by Ibanez [8]) are plotted in Figure 26. According to Ibanez, there is little change observed between room temperature and 649°C (1200°F) where there is an abrupt drop in fracture toughness. The fracture toughness curve reaches a minimum at 760°C (1400°F) and then increases with increasing temperature until 871°C (1600°F). The toughness values found in the TL orientation are

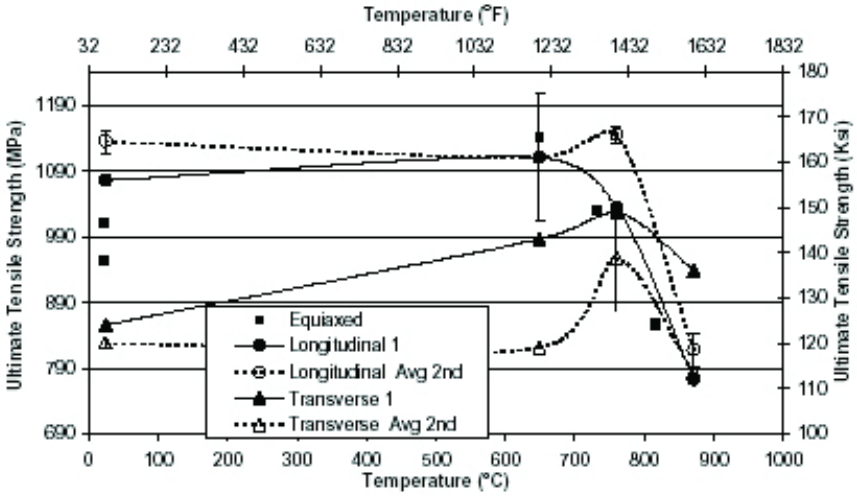

Figure 24: Ultimate tensile strength as a function of temperature for the different batches of DS GTD111 in the longitudinal and transverse orientations [8].

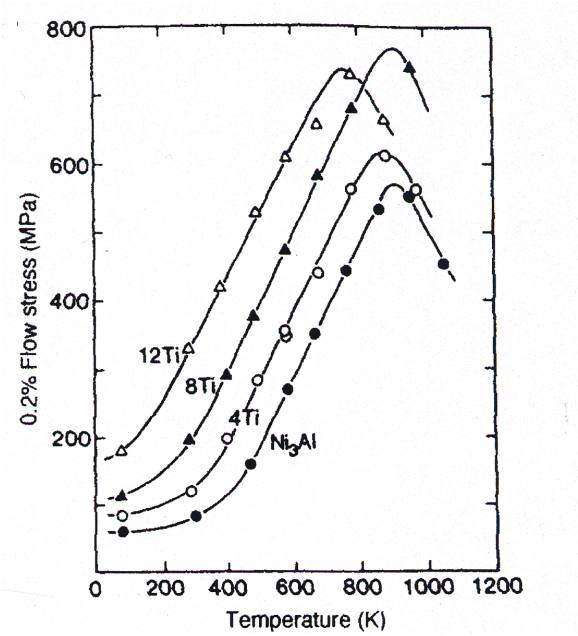

Figure 25: Flow stress of Ni_3Al as a function of temperature. Note that the addition of Ti to the precipiate increases the mass flow stress up to 8% Ti [8].

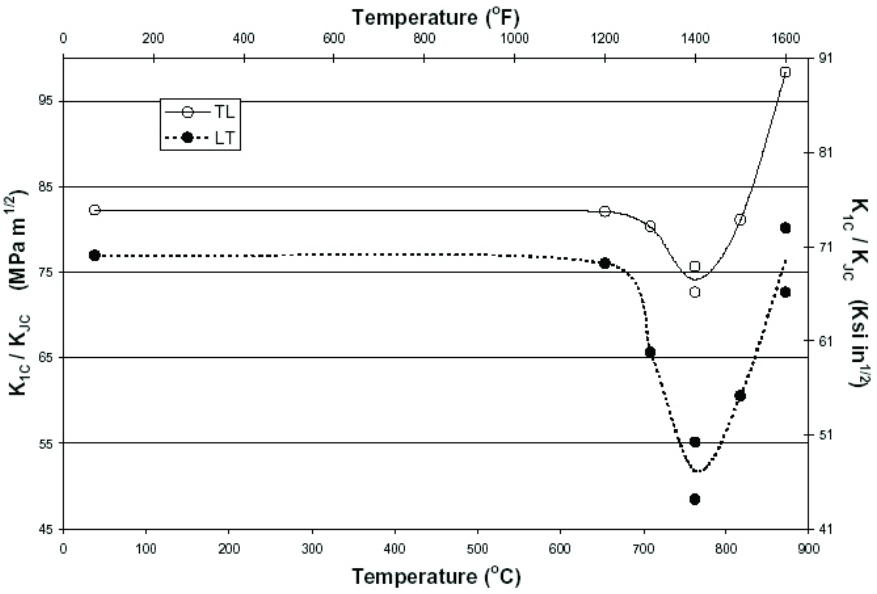

Figure 26: Fracture toughness values for DS GTD111 as a function of temperature in the LT and TL orientations [8].

higher than those in the LT orientation for every temperature considered.

The drop in fracture toughness again is attributed to a change in deformation mechanisms from octahedral slip of the precipitate phase, γ' at temperatures below 600°C to cubic slip at temperatures greater than 600°C [38]. This can be further supported by plotting fracture toughness as a function of yield strength (Figure 28), which shows that as the yield strength of GTD-111 increases as a function of temperature, the fracture toughness decreases.

The results of the fracture surface analysis indicate that Ta-rich MC carbides play an important role during fracture. While some surfaces show little to no ductility, other fracture surfaces show large amounts of brittle fracture, associated with interdendritic carbides that are surrounded by small areas of ductile fracture. Figure 27 shows a comparison of a fracture surface with a random plane of polish just below the fracture surface. Clearly, there is a higher concentration of carbides at the fracture surface than in the plane of polish. Furthermore, Figure 29 shows secondary cracking beneath the fracture surface of a tensile specimen tested at 760°C (1400°F). The crack path appears to follow several carbides, which are the bright particles in the BSE image. This suggests that the carbides

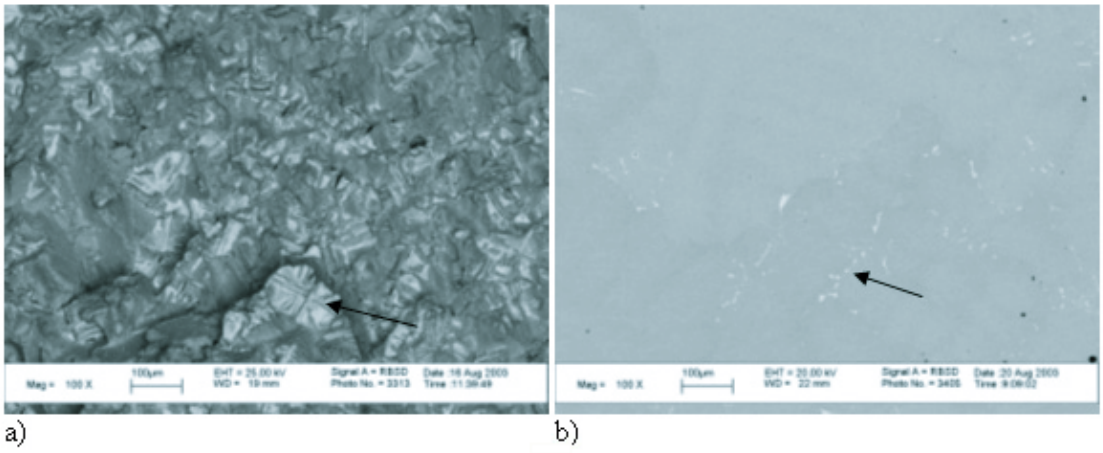

Figure 27: BSE images of a fracture surface (a) and plane beneath fracture (b.) The arrows point to carbides and the test temperature was 760°C (1400°F).

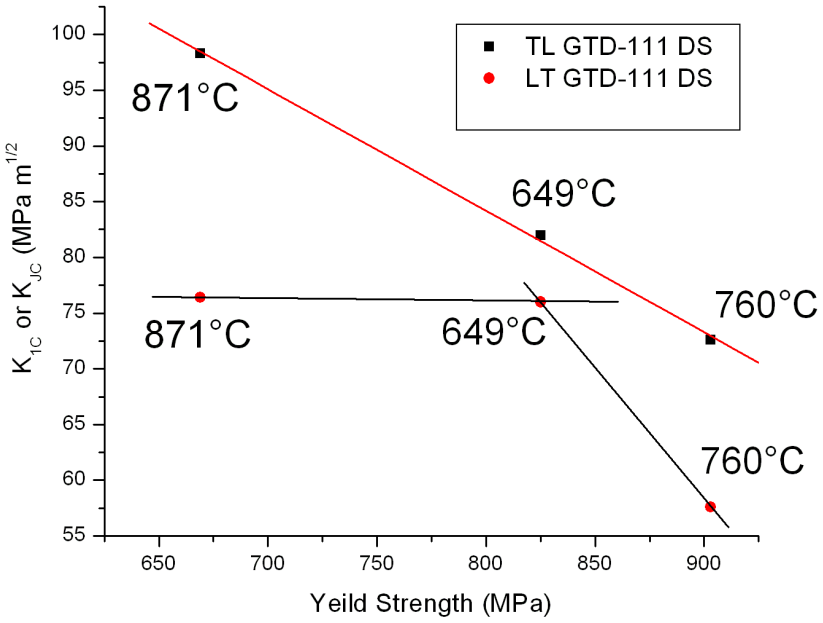

Figure 28: Plot of fracture toughness as a function of yield strength for both TL and LT GTD-111 DS samples tested at 649°C (1200°F) 760°C (1400°F, and 871°C (1600°F)).

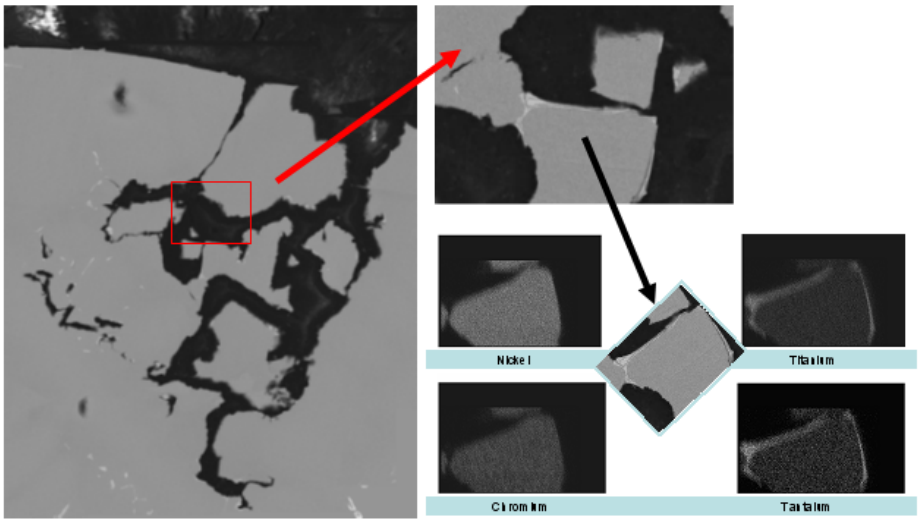

Figure 29: BSE image and x-ray map of secondary crack in a tensile specimen tested at 760°C.

greatly influence the fracture behavior of the material.

4.1.2 Stereology

As has been discussed previously in chapter 2, directional solidification creates an oriented structure. The large grain dimensions of GTD-111 DS lead to property variations between the longitudinal and transverse directions. This anisotropy can be quantitatively described by counting the number of intersections between a system of lines with the orientated microstructure. Quantitative stereology has already been employed to determine the volume fractions of phases present in bulk GTD-111 DS. Using additional techniques one can compare these bulk features to three-dimensional fracture surfaces.

4.1.2.1 Oriented structures

Figure 30 shows Saltykov's [9] classification of partially oriented structures. Figure 30b most accurately describes the columnar grain of GTD-111 DS. The majority of the grain surface is along the longitudinal direction, which is parallel to the growth axis. In a transverse plane the grain surface can be assumed to be arranged isometrically. Saltykov designated this type of structure as being linearly oriented.

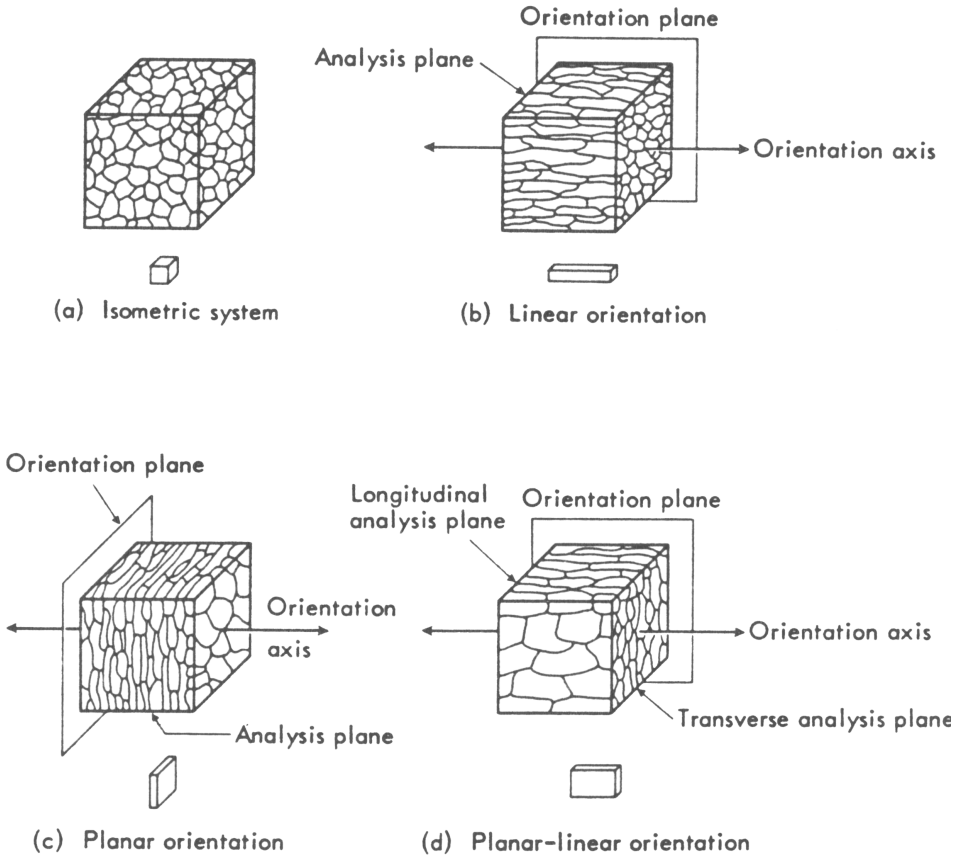

Figure 30: Types of partially oriented structures as classified by Saltykov [9].

Other linearly oriented structures that share this type of partial orientation include rolled materials that are elongated along the rolling direction. The mechanical properties of such a structure depend greatly on the orientation. A key reason for this is that inclusions or other features occur randomly throughout the material, but parallel to the orientation axis, cause failure. Example of such occurrences are bands of δ ferrite in rolled 304L steel [39] and the creation of non-metallic stringers [40, 41]. In the case of δ ferrite, researchers found that crack initiation is promoted when the loading axis in perpendicular to the δ ferrite (ie. the rolling direction) [39].

When sectioning mechanical test specimens from partially oriented, large grained materials, such as DS materials, there is often great variability in the number of grains per specimen, particularly between the longitudinal and transverse directions. Figure 31 shows the relative size of a tensile test sample to the slab from which it was machined. It can be seen that if the sample is machined in the direction perpendicular to the growth direction a larger amount of grains are included in the sample than if the specimen is cut parallel to the growth axis. In fact it is possible that the longitudinally cut samples may not intersect any grain boundaries at all. Figure 31shows how the partial orientation of a slab GTD-111 DS affects the number of grain in a particular tensile test specimen machine in either the longitudinal or transverse direction. A similar situation has been seen in the sampling of a rolled material with oxide stringers, as shown schematically in Figure 32.

A set of parallel test lines placed perpendicular to the rolling axis have the most intersections with the linear features (oxide stringers), whereas a test set parallel to the feature may not have any intersections. In Figure 32, the linearly oriented features are the oxide stringers. In this work, the linear features are the grain boundaries of GTD-111 DS.

It has been show that strength increases as the number of grain boundaries perpendicular to the loading axis is decreased [6]. The quantified number of grain boundaries per unit length can be determined by counting the number of intersections between the grain boundaries and an overlayed set of parallel tests lines on the slab of GTD-111 DS in both the longitudinal and transverse directions, as seen in Figure 33. This is important if one assumes grain boundaries that are perpendicular to the loading axis are weaker than grain

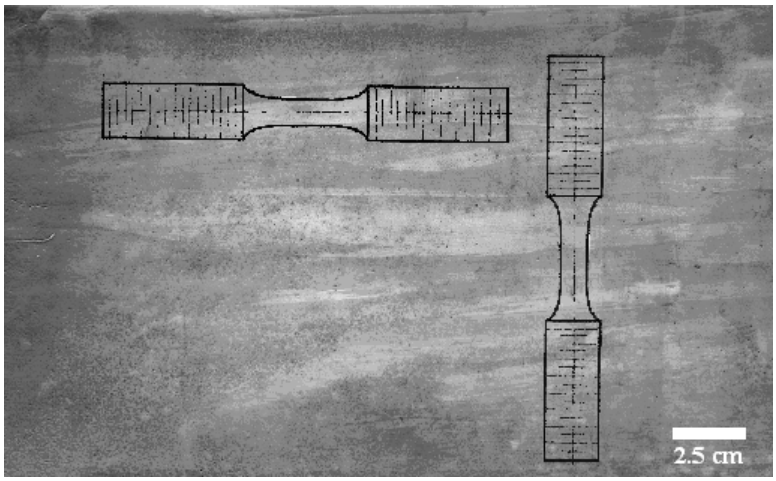

Figure 31: Slab of GTD-111 DS with tensile specimen outline in both the longitudinal and transverse directions. Tensile sample dimensions were 7.62 cm long with a 2.54 cm gauge length. The gauge diameter was 0.4 cm [9].

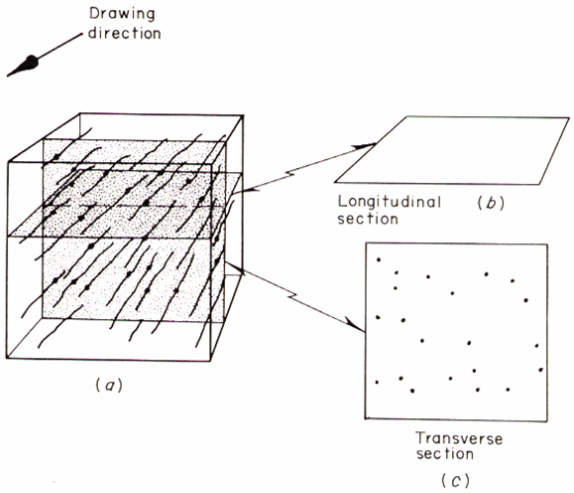

Figure 32: Schematic of linear oriented oxide stringers (a) intersected by test planes both parallel (b) and perpendicular (c) to the rolling direction by Saltykov [10].

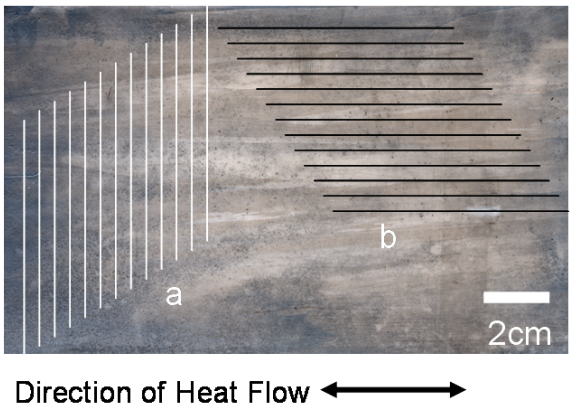

Figure 33: Test lines both perpendicular (a) and parallel (b) to the growth direction of a slab of GTD-111 DS

boundaries parallel to the loading axis and are therefore more likely to cause failure. The relative strengths of the grain boundaries in either direction can be estimated using creep ductility data [6] obtained by Ibanez [8] and shown in Figure 34. The creep ductility of the longitudinally oriented samples is higher than that to the transversely oriented samples, which supports the assumption that transversely oriented grain boundaries are weaker. especially at temperatures above 1200°C.

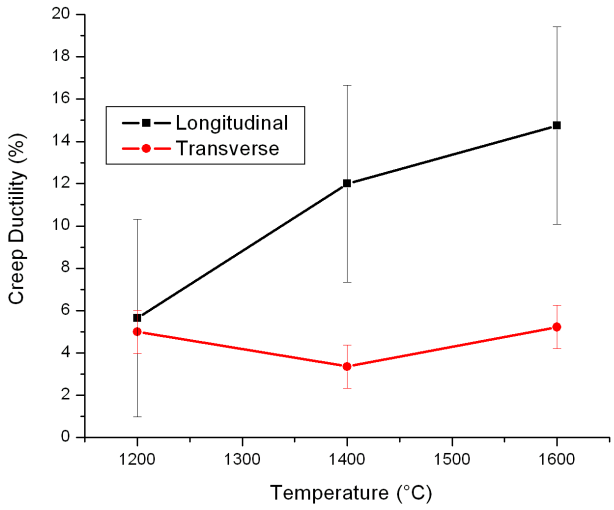

Figure 34: Creep ductility (%) as a function of temperature DS GTD 111 in the longitudinal and transverse directions [8].

4.1.3 Quantitative Fractography

Quantitative fractography was employed to connect fracture behavior to the key microstructural features in the tensile specimens already studied. These will include the interdendritic DPP and carbides discussed earlier. The goal of the technique was to provide quantitative information on the role of each constituent with respect to fracture path. It has been observed that the relative amount of carbides on the fracture surface appear to be larger than the amount in the bulk material. This suggests that the carbides largely affect crack path. The role of eutectic structures can be similarly characterized for comparison in an attempt to identify a dominant feature. Two methods, profilemetry and an SEM based technique were used to explore this phenomena quantitatively. A brief discussion follows.

4.1.3.1 Profilemetry

Fracture surfaces, when intersected by a vertical plane or section, yield a line profile of that fracture surface. A trace of the x and y coordinates of this profile can easily be collected using digital image analysis. From these data, several parameters can be determined to characterize the fracture surface. These include: fracture surface roughness, surface anisotropy, and the fraction of the profile through a given microstructural feature [42].

The experimental procedure for obtaining fracture profiles is fairly straight-forward. First, a vertical section perpendicular to the loading axis was chosen. The fracture surface must be plated with metal or polymer to protect the surface during sectioning. The sectioned sample was then mounted, polished, and etched using standard metallographic techniques. Optical and scanning electron microscopy were then then used to study the profile.

The profile roughness parameter R_L is defined as:

$$R_L = \frac{\lambda}{L}, \tag{14}$$

where λ is the total length of the fracture profile and L is the projected length of the profile. The surface roughness parameter was instrumental in allowing the use of SEM based

techniques as part of this work [42]. Another attribute that was useful is the fraction of the profile that passes through specific microstructural features, P_f. The following example illustrates the benefits of such measurements. A two phase material consists of β particles in an α matrix. The volume fraction of β in α is 2.0%. P_f for the fracture profile is 25.0%. Clearly, the fracture path is preferentially following β particles. Use of this parameter enables the connection of specific features to the fracture path. Based on qualitative results, it is proposed that cracks preferentially follow the interdendritic regions of the microstructure. More specifically, the role of carbide versus DP structures in these region was quantitatively determined through profilemetry.

4.1.3.2 SEM based method

While profilemetry alone is a powerful tool, it can easily be combined with an SEM approach to provide even more information. Most stereological methods can be applied to SEM fractography. However, it is vital to realize that SEM images are merely a projection of a 3-dimensional surface. As a result, the surface area of SEM images cannot be taken as the true surface area of the fracture surface [42]. A correction must be made to account for the lost of 3-D information due to the projection. An analog to the profile roughness parameter, R_L, is the surface roughness parameter, R_S, which is the true surface area divided by the apparent projected area.

$$R_S = \frac{S}{A}, \tag{15}$$

To experimentally determine R_S, the data generated by the profilemetry was used. This is done using:

$$R_S = R_L \cdot \psi \tag{16}$$

where R_L is the profile roughness and ψ is the profile structure factor. The equation depends on the average of the product of the R_L and ψ over several vertical sections. The number of

vertical sections needed to accurately determine R_S ranges between one and three [43]. For isotropic fracture surfaces it has been shown that only one section is needed. For structures with a preferred orientation, such as DS materials, the number of sections needed depends on the loading direction of the fracture specimen.

A DS material loaded in the longitudinal direction will crack across randomly oriented grains yielding an isotropic fracture surface. When loaded in the transverse direction, however, the fracture surface is anisotropic. More specifically, the dendritic structure of the DS material will yield what is referred to as a ruled surface [43]. In such cases it has been shown that an accurate value of R_S can be determined using only three vertical sections oriented 120 degrees from one another.

Determining R_L has already been described. The structure factor can also be calculated from the profile data. ψ is given by:

$$\psi = \int [(sin\alpha + \frac{\pi}{2}) - \alpha cos\alpha] f(\alpha) d\alpha, \tag{17}$$

where α is the angle between a line segment and the vertical axis such that α is between 0 and π, and $F(\alpha)d\alpha$ is the distribution function of all line segments having an orientation in the range of α to $(\alpha + d\alpha)$. Since distribution functions are often calculated in a histogram, a method has been developed to solve the integral using a discretized summation [42].

$$\psi = \sum a_i h_i, \tag{18}$$

where a_i is a coefficient and h_i is the fractions of line segments that have an orientation angle, α, in the range between 10(i-1) and 10i. The values for i and a_i can be found in existing tables.

Once R_S is determined, the projected images acquired in the SEM can be corrected to give the true surface area. SEM analysis can then be used to determine area fraction of the carbides on the fracture surface.

The volume fraction of carbides in the bulk material have been determined to be 2% using BSE imaging and the point counting method. The fracture surfaces of each specimen was imaged using this same BSE technique as BSE imaging yields better compositional contrast [44] prior to sectioning. This was done since sectioning for profilemetry destroys the fracture surface. An areal analysis performed on the SEM fractographs will yield the area fraction of carbides per apparent area. The roughness parameter can then be used to correct this value to the area fraction of carbides per true area (F):

$$F = \frac{R_S}{(R_S)_\beta} A_a, \tag{19}$$

where $(R_S)_\beta$ is the surface roughness parameter of the specific inclusion and A_a is the projected area fraction from the SEM image.

Similarly, the number density of carbides on the fracture surface N_f can be determined using:

$$N_f = \frac{N_s}{R_S} \tag{20}$$

where N_s is the number density of carbide found in the SEM micrograph. This must also be corrected by dividing by the roughness parameter R_s. Once again, if the values of F and N_f of a given feature are higher than the values in the bulk material, then a preference for crack path can be observed. In the rare case where the area fraction of the feature is less than in the bulk, the feature may retard crack growth [42].

4.2 Experimental

4.2.1 Metallography

The grip sections of each tensile specimen were sectioned after tests in the both the transverse (perpendicular to the loading axis) and longitudinal (parallel to the load axis) directions. The sectioned samples were mounted in edge-retaining bakelite mount and were mechanically polished using 320 to 4000 grit abrasive SiC paper. Final polishing occured

using alumina suspension in steps from 1.0 to 0.05 μm. The samples were then rinsed in ethanol and etched using a 60% lactic acid, 38% nitric acid, and 2% hydrofluoric acid solution to reveal the microstructure. The precipitate phases were identified using a scanning electron microscope (SEM) equipped with an electron dispersive spectroscopy system. To quantitatively characterize the volume fractions of these phases, both optical and SEM imaging were used in conjunction with digital image analysis using standard stereological techniques [34].

4.2.2 SEM Fractography and Surface Roughness

To examine the relationship between fracture behavior and precipitate phases, the fracture surface of each tensile sample was examined in the SEM. An image montaging technique was used to provide high magnification images of the entire fracture surface. Once both mating surfaces were imaged using SEM, the values of Rs, were determined using profilemetry and confocal microscopy. The directionally solidified nature of the sample oriented parallel to the loading axis allows accurate quantitative measurements using a single vertical section [42]. To preserve the fracture surface profile during sectioning, an edge retaining mounting material was applied to the sample prior to cutting. The vertical sections were then polished using the previously described method. Key fractographic parameters such as the linear roughness parameter (R_L), profile structure factor (ψ), apparent area fraction (A_A),surface roughness parameter (R_s), and the true volume fraction of phases (F), were determined using well established fractographic methods [34].

Using profilemetry on the transversely oriented samples proved to be impractical given the experimental difficultly of sectioning such small fracture surfaces. To avoid difficulties the true surface roughness was determined using a Leica laser scanning confocal microscope (LSCM) to obtain the true surface areas of fracture specimens in both the transverse and longitudinal orientation. The use of LSCM to characterize surface roughness of material is well documented in the literature [42, 45]. To normalize all of the results, a calibration curve was used to relate the roughness values obtained by LSCM to those determined by profilemetry.

4.3 Results and Discussion

Figure 35 depicts a micrograph of a grip section of a tensile sample. The transverse sections of the columnar grains can be seen including a great deal segregation that occurred during casting. The major strengthening phase present is Ni_3Al precipitates range in size from 0.1 μm to 1.0 μm. The volume fraction of γ' in GTD-111 was determined to range between 50-60%. This has also been observed in other studies [36, 35].

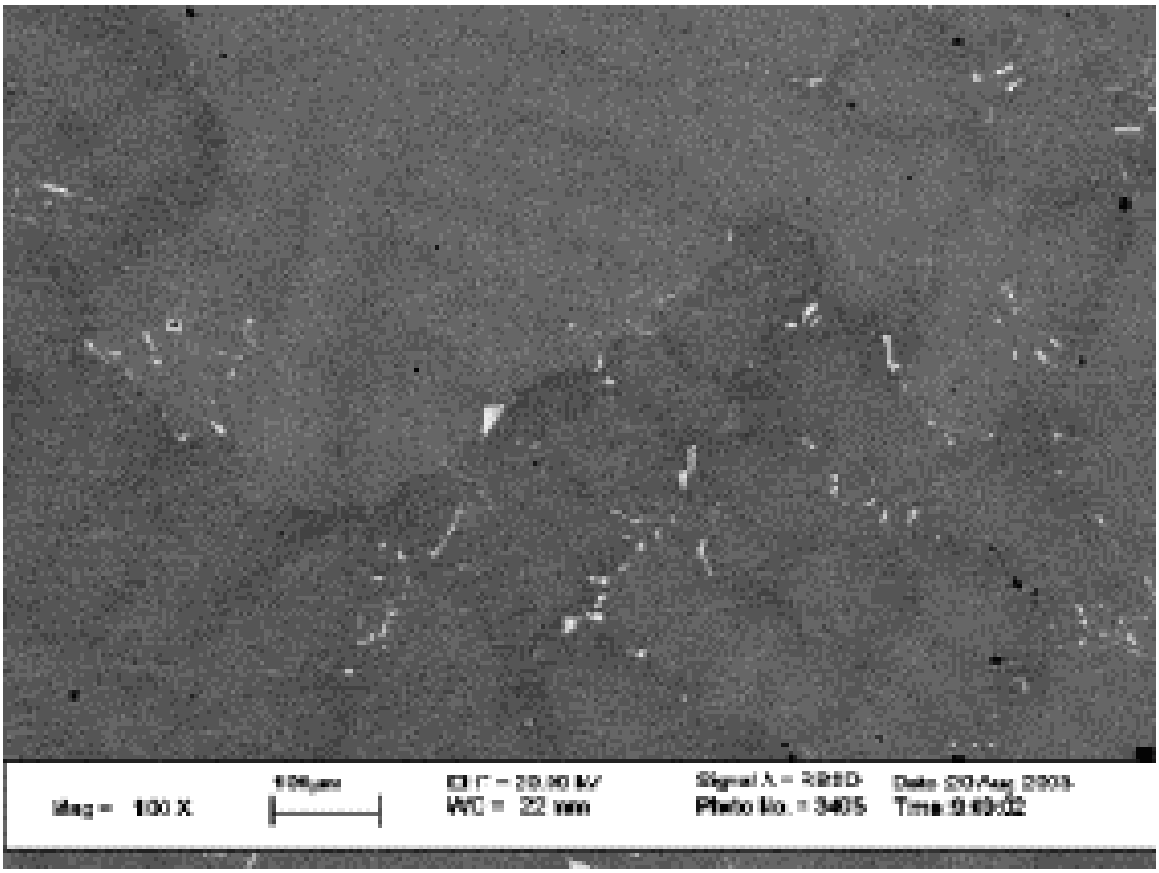

Figure 35: SEM micrograph of a tensile grip section showing the segregated columnar grains

In addition to γ', (Ti,Ta)C carbides are found, mostly in the interdendritic regions of the material. This can be attributed to the fact that these carbides form early in the casting process and are free to float within the melt [27]. They are then trapped between dendrite arms when the last of the liquid solidifies. The shapes are often referred to as the "Chinese script" morphology due to the fact they resemble Chinese characters [6]. This

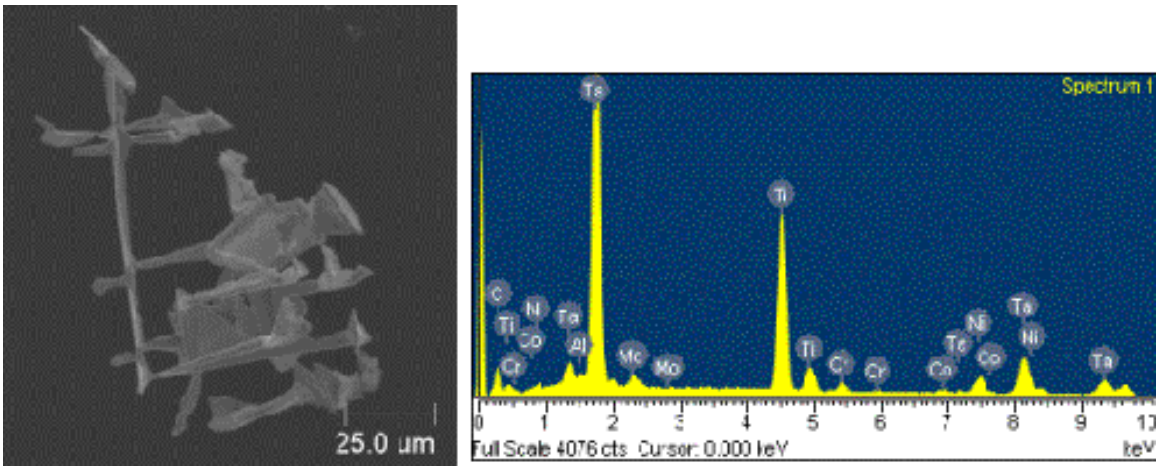

Figure 36: SEM micrograph of a "script" carbide chemically extracted from the matrix in accordance with ASTM standards (left) and the corresponding EDS spectra confirming (Ti,Ta)C composition.

can be illustrated best in Figure 36 which shows an individual carbide that has be removed from the matrix using a chemical extraction technique in accordance with ASTM standards [46]. The average volume fraction of carbides in bulk GTD111 DS was determined to be 0.02 and the number density of the carbide was $1.5\text{x}10^{-4}m^{-2}$.

4.3.1 Oriented Structure Characterization: Number of Grain Boundaries per Unit Length

By placing a set of parallel test lines over the slab shown in Figure 19, the number of grain boundaries per unit length was determined to be 0.563 cm^{-1} in the longitudinal direction. In the transverse direction, the number of grain boundaries per unit length was determined to be 2.378 cm^{-1} suggesting that samples that in the transverse direction with respect to the growth axis will have approximately 4 times as many grain boundaries per unit length than longitudinally oriented samples.

4.3.2 Fracture Surfaces

Identifying key microstructural features that may influence the fracture behavior in an SEM can be difficult due to lack of contrast when using secondary electrons. However, using backscattered electron imagining, the compositional contrast between the Ti,Ta -rich carbides and the Ni matrix makes it easy to identify fracture surface carbides [44].

Figure 37 compares two SEM micrographs. The left image is a secondary image (SE) and the right is a BSE image. In the SE image it is often difficult to distinguish the boundaries between carbides and the matrix. The BSE imaging, however, provides the distinction of clear boundaries of the particle. This is due to the fact that the backscattered coefficient, η (the number of backscattered electron/number if incident electrons), increases monotonically with atomic number. This serves as the basis for compositional contrast [44]. Heavier elements, such as Ta will appear brighter than lighter elements, such as the nickel matrix, which will appear dark. The distinct compositional contrast therefore makes it easy to quantify the carbides. This is true in polished samples as well as on the fracture surfaces and was used to quantify these features.

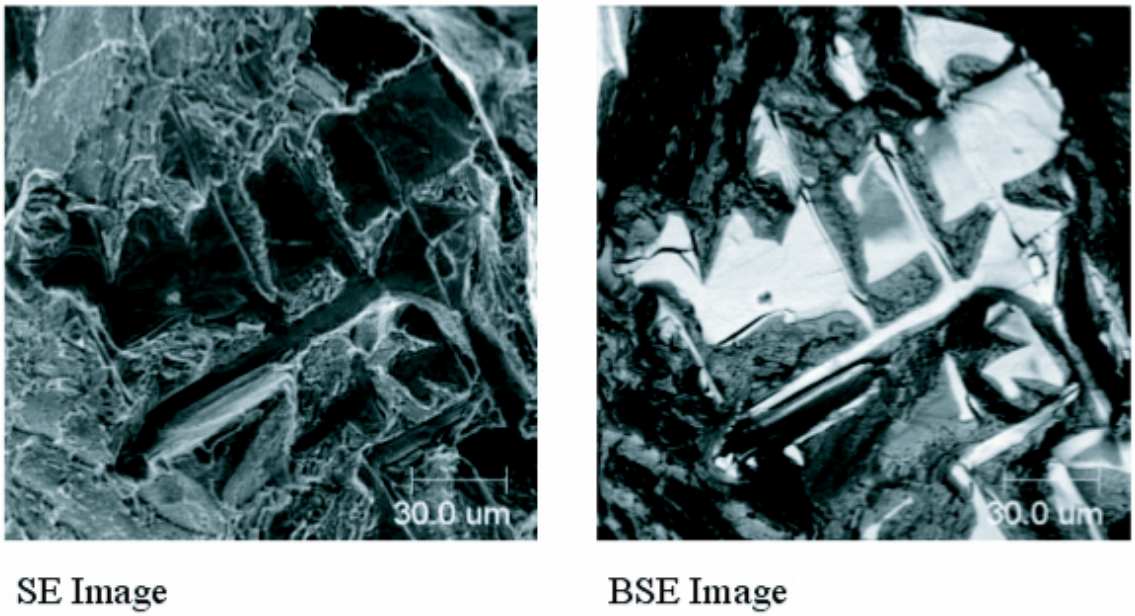

Figure 37: SEM images of fracture surface of tensile specimen tested at 760°C.

To confirm that these features are Ti,Ta carbide, EDS mapping was employed to mapped the relative amounts of Ti, Ta, Ni, Cr, and C. Figures 38 and 39 show that the areas that are rich in the carbide forming elements (Ti,Ta, and C) are also deficient the matrix forming elements (Ni and Cr).

The results for longitudinal samples (Table 3) show that the true area fraction, F, and number density N_f on the fracture surfaces at each of the test temperatures is significantly

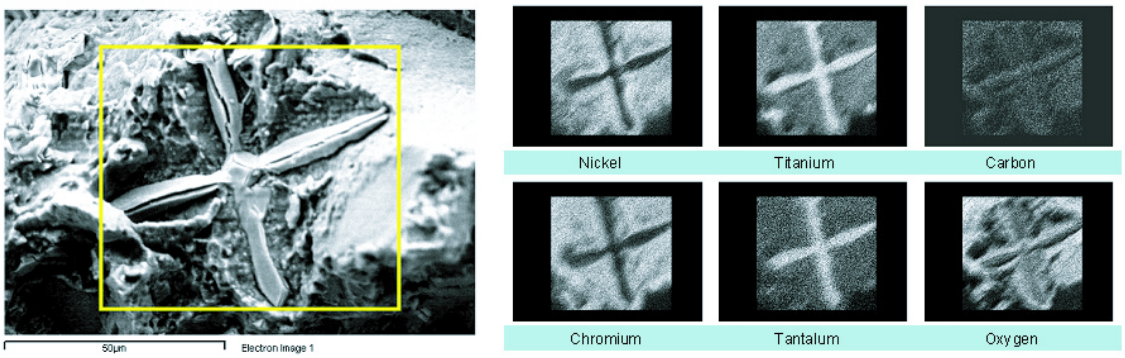

Figure 38: X-ray map of fracture surface carbide.

higher than the bulk volume fraction and number density. This suggests that the carbides are greatly affecting the tensile fracture behavior of the longitudinally oriented GTD-111 DS. The average difference between the apparent carbide area fractions (A_s) and the true area fractions (F) was approximately 2% indicating that a fairly low degree of error is introduces when using only the apparent area fractions from the SEM images.

Table 3: Summary of the fractographic parameters obtained from longitudinally oriented samples to determine the true area fraction of carbide on the fracture surface, F. The values for F at all temperature is significantly higher that 0.02, the volume fraction of these carbides in bulk GTD-111 DS.

Temperature		Fractography Parameters				
°C	°F	R_l	ψ	R_s	A_s	F
21	70	3.686	1.022	3.767	0.118	0.091
649	1200	2.714	1.258	3.413	0.133	0.132
760	1400	2.663	1.245	3.314	0.123	0.118
871	1600	2.058	1.217	2.504	0.114	0.085

Figure 40 shows the relationship between the roughness parameters determined by the LSCM and those determined for profilemetry. A linear relationship was observed and was used to convert the roughness value into similar terms for comparison. Table 4 summarizes all of the results obtained in this study. Both orientations show higher area fractions of carbides on the fracture surfaces than what can be found in the bulk material. However, on average, the longitudinal orientation shows approximately four times as much carbide

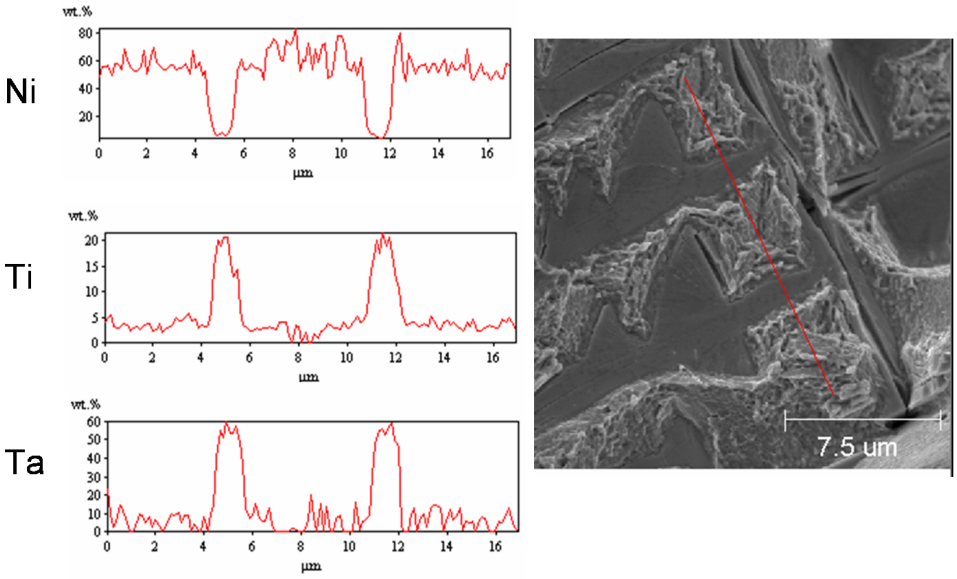

Figure 39: X-ray line scan of fracture surface carbide.

area as does the transversely oriented case. The number density also follows a similar trend showing that the greater amount of carbides per unit area is found on the fracture surface of the longitudinally oriented specimen.

This can be explained by recalling that grain boundaries are weaker when they are oriented perpendicular to the loading axis, as is the case with transversely oriented samples [27]. In this case the dominant cause of failure is the grain boundary itself, so failure is less likely to be caused by the carbides, resulting in fewer carbides being found on the fracture surface. In the longitudinally case, however, the grains are perpendicular to the loading axis, which maximizes the grain boundary resistance to failure. Now, the grain boundary itself is not the dominant cause of failure; the carbides are responsible for fracture, which explain the greater area fractions of carbides on the fracture surfaces. In summary, the relative likelihood that either orientation or the presence of carbides causes failure would follow: transverse grains, carbides, and longitudinally oriented grains, with transverse grain boundaries being the most detrimental and longitudinal grains being the most beneficial, which is well documented in the literature [6, 17, 27]

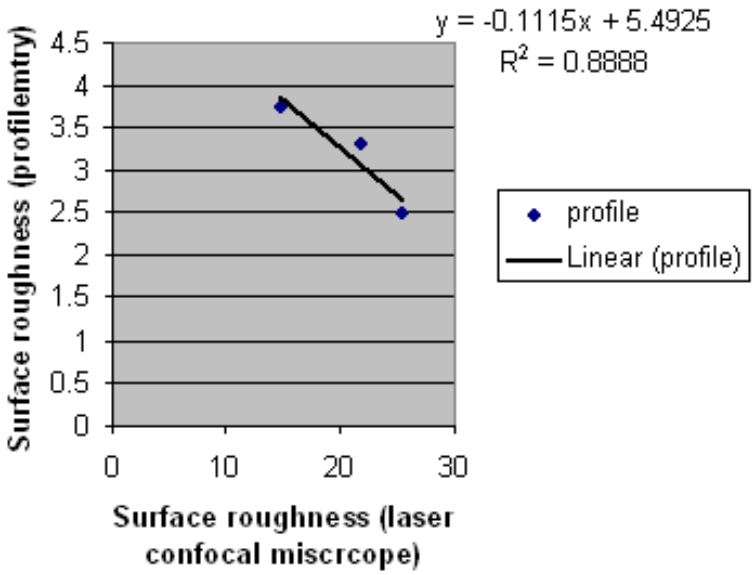

Figure 40: Correction curves for normalized surface roughness of transverse to longitudinal specimen using laser scanning confocal microscopy.

Table 4: Summary of the area fraction of carbides and number per unit area of carbides μm^{-2} for both longitudinal and transverse orientations. The values for F and N_f at all temperatures is significantly higher in bulk GTD-111 DS.

Temperature		Area fraction of carbides (F)		Number per unit area (N_f)(μm^{-2})	
°C	°F	Longitudinal	Transverse	Longitudinal	Transverse
21	70	0.118	0.038	6.46E-04	1.33E-04
649	1200	0.133	0.016	4.65E-04	2.93E-05
760	1400	0.123	0.063	4.64E-04	6.04E-05
871	1600	0.114	0.031	7.73E-04	7.99E-05

4.3.3 Carbide fracture behavior

The results of the fractography clearly show that carbides are affecting the fracture behavior of the material. To identify the mechanism by which this fracture occurs, the SEM montage of each set of mating fracture surfaces were examined side-by-side. The benefit of this is that one can clearly see if the carbides are debonding from the matrix or are themselves cracking into two halves that can be observed on both surfaces. For the material in this study, it is clear that the latter case occurs. Figure 41 shows a typical set of mating fracture

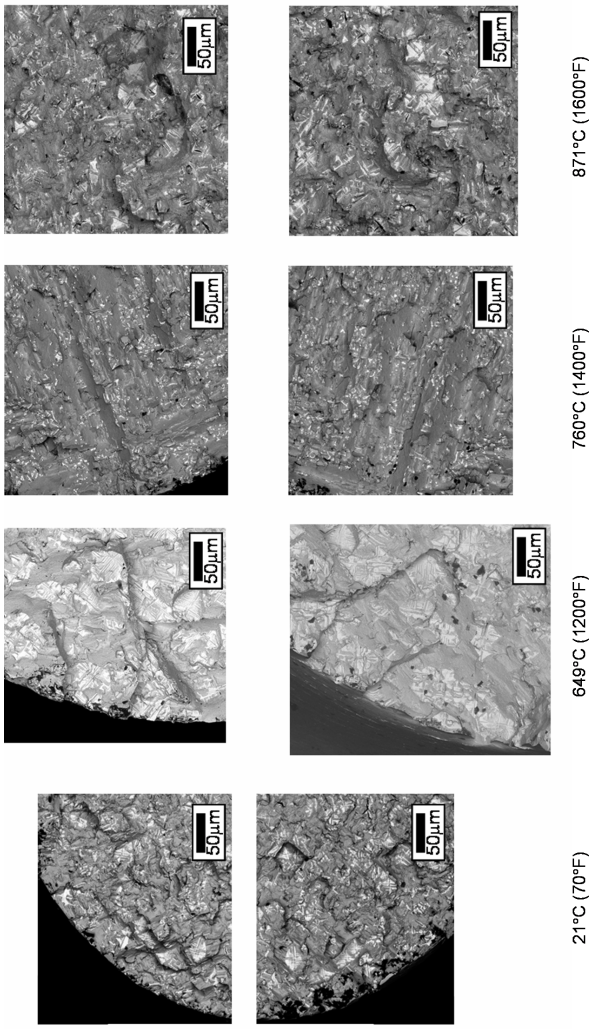

Figure 41: BSE images of mating surfaces of a longitudinal tensile specimens 25, 649, 760, and 871°C.

surfaces. The carbides of interest can be seen on both sides of the fracture indicating that they have indeed cracked rather than debonded.

4.4 Conclusions

Statistical scatter in tensile tests performed by Ibanez [8], as well as a qualitative observation of an abundance of carbides on the fracture surfaces of each specimen has led to the need to quantify the anisotropy of GTD-111 DS as well as the role of carbides on fracture for both orientations of tensile tests. The major points of this chapter are:

1. Due to the partially oriented structure of GTD-111 DS, samples sectioned in the transverse direction with respect to the growth axis will have approximately 4 times as many grain boundaries per unit length than longitudinally oriented samples. These grain boundaries are perpendicular to the loading axis and based on creep elongation data, are weaker than longitudinally oriented grain boundaries.

2. Profile analysis has shown that for tensile tests conducted at temperatures of 25, 649, 760, and 871°C, the true area fraction of carbides on the fracture surface is significantly higher than, the volume fraction of carbides found in the bulk material (2%) for longitudinally oriented samples.

3. For transversely oriented samples, where profilemetry could not be easily used, laser confocal microscopy was employed to determine the surface roughness number of the samples and calculate the true area fraction and number density of carbides on the fracture surface. Again, these values are 3-5 times greater than those found in the bulk material. This indicates that the carbides clearly influence the fracture of the material in both orientations, although there was a greater amount of carbides found in the longitudinal case. This is attributed to the fact that transversely oriented grains are weak and cause failure, whereas as failure of longitudinally oriented boundaries, which are stronger, must be assisted by the presence of the carbides.

4. Examination of mating fracture surfaces of tensile specimen shows that carbides are cracking rather than debonding from the matrix.

CHAPTER V

DETERMINATION OF THE γ' SOLVUS AND HEAT TREATMENTS

The results obtained in the previous chapter seem to indicate that interdendritic carbides are influencing fracture path in tensile samples. However, care must be taken when trying to tie the fracture path solely on the carbides as they are not the only microstructural feature that are found in the interdendritic regions. The interfaces of larger discontinuous precipitated γ' may also serve as nucleation sites for fracture. This chapter attempts to clarify the role of the carbides by eliminating the DPPs that are found in the interdendritic regions, through heat-treatments.

5.1 Background

Recall that the as-cast microstructure of GTD-111 DS is comprised of primary Ni (γ) dendrite stalks, which grow approximately anti-parallel to the flow of heat along the $\langle 100 \rangle$ directions. These dendrites are accompanied by secondary arms that grow perpendicular to the primary $\langle 100 \rangle$ directions and tertiary arms that are perpendicular to the secondary arms and parallel to the primary arms. The size of the arms decreases from primary to tertiary arms during solidification and the composition of the arms varies due to coring effects. Because the composition varies across the γ dendrite arms, the morphology of the phases (e.g.$Ni_3(Ti, Al)$) vary in a systematic way across the arms.

The large size range and compositional variation between particles makes dissolution a complex process. It is often observed in as-cast superalloys that the solvus temperature of the $Ni_3(Ti, Al)$ phase (γ') does not occur at a single temperature, but instead it occurs over a range of temperatures since the as-cast microstructure consists of an inhomogeneous distribution of particle sizes and shapes [17]. Smaller particles will dissolve at lower temperatures, whereas the dissolution of larger particles will be sluggish as these particles are energetically more stable. This effect is not observed in well-solutionized microstructures where all of the γ' particles are of similar size and shape. In addition to γ', high temperature

(Ta,Ti)C precipitates are also present in the microstructure. While the presence of these carbides has been found to increase creep resistance [17], it has been suggested that they may also serve as crack initiation points during fatigue conditions [27].

It is known that γ', an ordered $L1_2$ $Ni_3(Ti, Al)$ phase, controls the overall mechanical properties of materials in this class of superalloys and that the casting process creates a highly inhomogeneous distribution of γ' particles due to coring [27]. Depending on the particle size, volume fraction and temperature during deformation, the γ' particles may be sheared by moving dislocations or act as nucleation sites for dislocation bowing (Orowan loops). The ideal microstructure for mechanical properties would be a uniform distribution of starting solute to control the spatial distribution of particles. However, this is not often achieved as the solution heat treatment times needed to completely remove the segregation and create a uniform particle distribution are exceedingly long to be commercially practical. The common compromise is to design a microstructure that consists of a bimodal distribution of γ' particles. This is achieved using a super solvus heat treatment [27]. The super solvus heat treatment involves heating the material to a temperature above the γ' solvus temperature and holding for shorter times periods ($\sim$ 2h) to dissolve the smaller γ' particles. However, largest particles, including any γ/γ' eutectic, remain since the hold time is insufficient to homogenize the alloy. Upon cooling to a lower (i.e. aging) temperature, γ' particles begin to nucleate and grow. After aging, as the alloy is cooled to room temperature new, smaller particles continue to nucleate, which creates a bimodal distribution of γ' in a FCC Ni (γ) matrix [27, 17]. Treatments like this require only a broad sense of the solvus temperature and can lead to inefficiencies in the heat treating process. To completely homogenize the microstructure or at least to tighten the control of the heat treatment, the temperature at which the γ' particles dissolve must be defined to ensure a successful homogenization and optimization of the microstructure. To determine the solvus range of γ', three techniques including differential thermal analysis (DTA), conventional heat treatment coupled with metallography, and dilatometry were investigated in this study.

The DTA technique is commonly used to follow microstructural changes such as precipitation reactions in superalloys [47, 48, 49]. DTA uses a small sample size which can create

difficulties in obtaining representative post-analysis metallographic samples. The benefit of the traditional metallographic technique is that microstructural changes can be followed visually as the dissolution process occurs. However, this method can be quite tedious in terms of experimental time and sample preparation. Using dilatometry, the solvus of the γ' precipitates can be determined by observing changes in the coefficient of thermal expansion (CTE) of the alloy as a function of temperature [50]. Dilatometry is a faster, less tedious method than metallography and utilizes relatively large samples and is therefore more representative of the bulk microstructure in comparison with the DTA technique. This is particularly true when microstructural features (i.e. dendrite arm spacing) are relatively large. The first section of this chapter utilizes these three techniques for the purpose of determining the solvus temperature of γ' for GTD-111 DS for heat treatment applications and evaluates the applicability of the dilatometry technique to as-cast alloys.

5.2 Experimental Procedure

5.2.1 Determination of γ' solvus boundary

Figure 42 illustrates how the sizes of the three testing samples compare and shows a section of an as-cast slab with long columnar grains that are approximately 2 cm in diameter. The metallographic technique has a variable range of sample size depending on the type of characterization technique being used, but it is on the order of the outline in region 1 (Figure 42). Region 2 shows the relative size of a dilatometry sample to the as-cast microstructure. In the direction perpendicular to the columnar grain structure (as shown in Figure 42) the specimen is large enough to sample several grains. For this reason, samples were sectioned primarily from this orientation. The DTA samples are outlined in the Figure as region 3.

5.2.1.1 Differential thermal analysis

DTA was performed using a Perkin Elmer DTA-7 with alumina crucibles and a flowing argon atmosphere. Samples weighing approximately 200 mg were heated at a rate of 10°C/min to 1450°C and cooled to room temperature at the same rate. Data collected on cooling was used to determine the γ' solvus temperature since DTA cooling results are considered to be more accurate than heating results due to kinetic concerns [51]. Typically, DTA

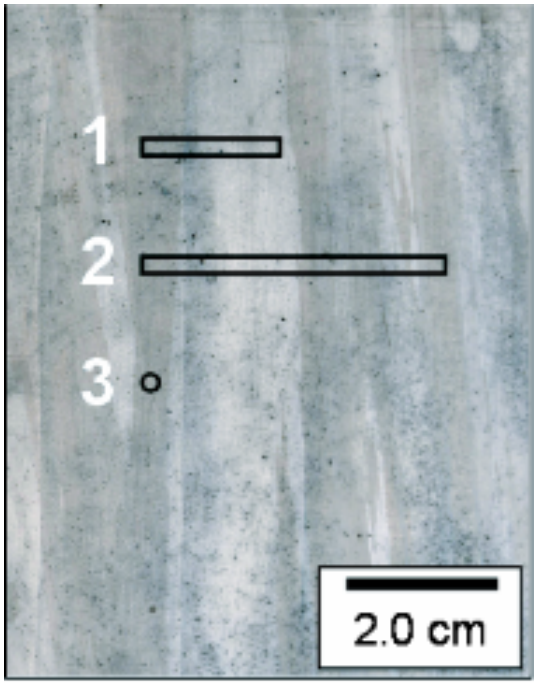

Figure 42: Relative sample sizes for traditional metallographic (1), dilatometry (2), and DTA (3) outlined on an as-cast slab of GTD-111 DS.

reactions signified by endotherms/exotherms can be identified using x-ray analysis of the quenched DTA sample before and after the endotherm/exotherm [47]. Since this study used two additional methods to identify the reactions, x-ray analysis was deemed unnecessary. The possible DTA reactions for each endotherm/exotherm were identified using data from other researchers [27, 17, 47] and confirmed using scanning electron microscopy and energy dispersive spectroscopy.

5.2.1.2 Heat treatment/metallography

Samples (3 x 3 x 16 mm) were placed in an infrared (IR) gold image furnace, which is capable of rapid heating and cooling rates [51] and heated in flowing argon to the temperature of interest (1180°C, 1200°C, 1250°C, and 1300°C). Samples were held at temperature for 2 h and then quenched at a rate exceeding 100°C/min. The rapid quench essentially freezes the microstructure at the given hold temperature and limits the growth of γ', which commonly occurs with slower cooling rates. After each heat treatment, samples were examined using standard optical microscopy techniques [34].

5.2.1.3 Dual-pushrod horizontal dilatometry

The solvus temperature of the alloy was determined by applying a dilatometry technique as described by Hermann *et al.* for wrought alloys [50]. A sample weighing approximately 10 g was cut into a rectangular prism (3 x 3 x 35 mm) with flat, parallel ends and placed in a dual-pushrod horizontal dilatometer with a sapphire reference. The sample temperature was measured with a thermocouple junction floating roughly 2 mm above the midpoint of the alloy specimen. An argon gas atmosphere was used to prevent excessive oxidation of the sample during the test. The sample was heated at a rate of 3°C/min to 1300°C and then cooled at a rate of 3°C/min to 300°C. Linear expansion and temperature data were acquired upon heating and cooling. The experiment was repeated five times; the first run was performed to homogenize the sample and omitted from analysis [50]. The instantaneous CTE (α_T) of the alloy was calculated by taking the derivative of the linear expansion data according to

$$\alpha_T = \frac{1}{l_0}\frac{dl}{dT} \tag{21}$$

where l is the sample length at temperature T and l_0 is the sample length at 20°C. The numerical derivative was calculated from the raw Δl versus T data by linear regression over ranges of 11 data pairs. In a similar manner, the inflection points of the CTE versus T plots were determined by numerically calculating the 2^{nd} derivative of the CTE versus T data set and finding the temperature at which it was equal to zero [11].

5.2.2 Dissolution of γ'

Circular samples (diameter = 12.7 mm) were placed in an infrared (IR) gold image furnace, heated in flowing argon to 1300°C), held for varying amounts of time (0, 15, 30, 60, 120, 240, 480, 720 minutes), and quenched at a rate exceeding 100°C/min. Again the rapid quench essentially freezes the microstructure at the given hold temperature and limits the growth of γ'. After each heat treatment, samples were examined using standard optical microscopy techniques [34] to follow the dissolution of γ' as a function of time.

5.3 Results and Discussion

5.3.1 Determination of γ' solvus boundary

Figure 43 shows the typical microstructure found in as-cast GTD-111. A highly cored dendritic microstructure containing both γ' and (Ta,Ti)C particles in a FCC Ni matrix (γ) was observed. The variation in contrast within dendrite arms was attributed to differences in both the size and spatial distribution of γ' precipitates. The particles in the dendrite cores were spherical with a size of approximately 0.1 μm. As the distance from the core increased, the particle size increased to approximately 1.0 μm and the shape changed to octets of cubic particles (Figure 44). The γ' located in the interdendritic region was much larger and in the form of a γ/γ' eutectic, which is commonly observed in superalloys [17]. This as-cast structure was found to be similar to other studies characterizing GTD-111 [36, 35].

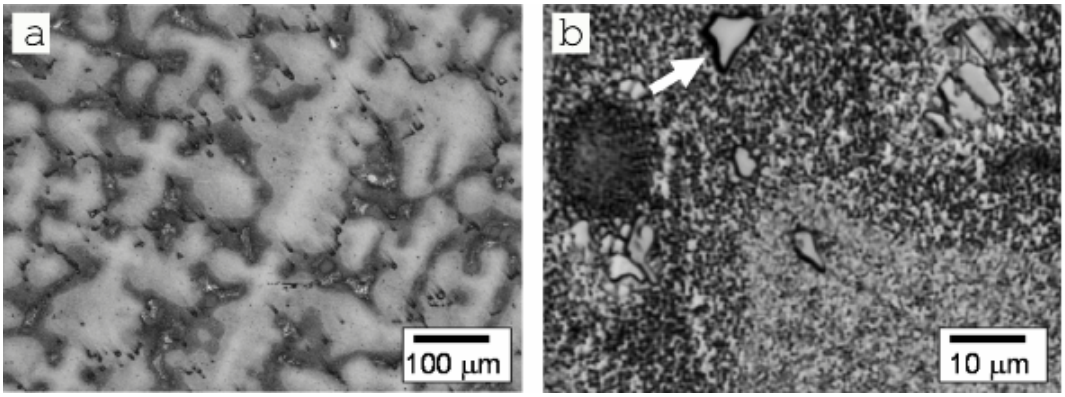

Figure 43: Optical micrograph showing the as-cast microstructure of GTD-111 DS. The variation in contrast (a) corresponds to differences in both the size and distribution of γ' precipitates. The arrow (b) indicates a (Ta,Ti)C particle as identified by energy dispersive spectroscopy.

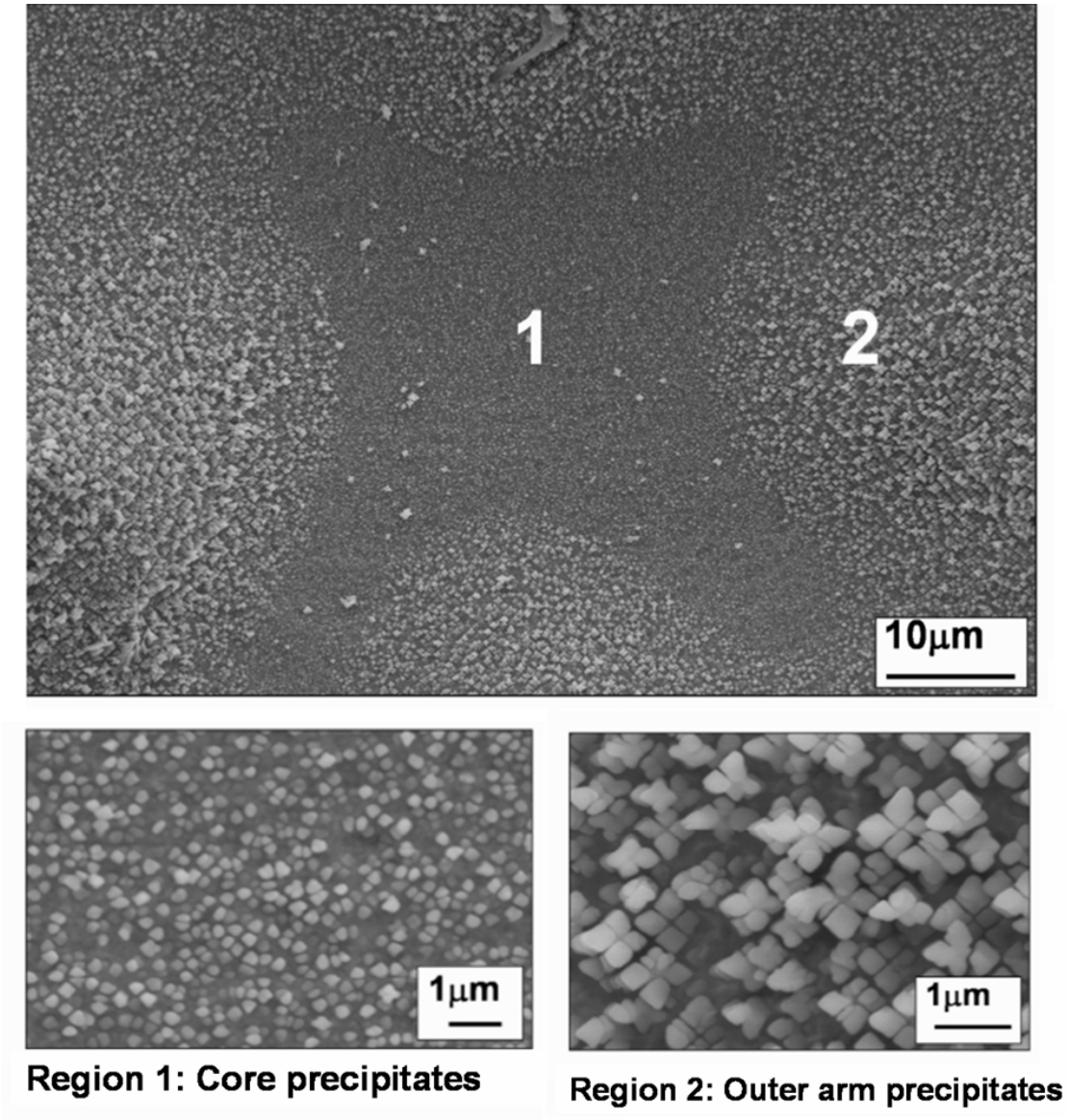

Figure 44: SEM image of cored dendrite structure from as-cast GTD-111 DS. Note the variation in both size and shape of the γ' particles from small spherical particles to larger octets of cubes moving from the dendrite core (region 1) outward into the dendrite arm (region 2).

5.3.1.1 DTA

Figure 45 shows a DTA cooling trace with various endotherms/exotherms. The DTA peaks can be matched to their specific reactions by knowing the phases present in the microstructure and the approximate temperatures at which these phases form. The reaction occurring at each peak was identified based on current literature [17, 47]. Four peaks of interest are highlighted in Figure 45. A small initial peak (1) at 1385°C corresponds to the formation of (Ta,Ti)C carbides. This high temperature carbide phase is often observed in superalloys and is described by having a "script" morphology [27]. Since the (Ta,Ti)C carbides form at a temperature that is higher than the melting temperature of the γ matrix, it is clear that these structures cannot be completely removed from the alloy using heat-treatment, without significant risk of incipient melting [17]. Peak 2 (1352°C) indicates the temperature at which the matrix starts to solidify. Peak 3 (1332°C) represents a eutectic transformation taking place in which the volume fractions of both γ and the carbide phases are increasing; this was also observed by Zupanic *et al.* [47]. The small final peak (4) at approximately 1211°C corresponds to the precipitation of γ'. The average value of the γ' solvus temperature over four samples was determined to be 1193 $\pm$ 10.7°C.

5.3.1.2 Heat treatments

Micrographs taken after the heat treatments (Figure 46) show γ' dissolution over a range of temperatures. There is a clear increase in the extent of dissolution as a function of hold temperature for the same 2 hour hold time. The rapid quench ($>$ 100°C/min) that was achieved by using the IR furnace prevented any substantial particle growth during cooling, which allowed for comparison of the microstructure that is present immediately after heat treatment. The dissolution begins at 1200°C and can be observed at the center of the dendrites by noting the "cleared" areas (marked by arrows in Figure 46) where γ' particles were no longer present. The smaller particles are the first to dissolve (Figure 46b) followed by the larger particles (Figure 46c-d) moving outward from the core. The area fraction of the "cleared" regions increases with hold temperature up to 1250°C where only the largest γ' particles remain. At 1300°C, the dendritic features in the microstructure can

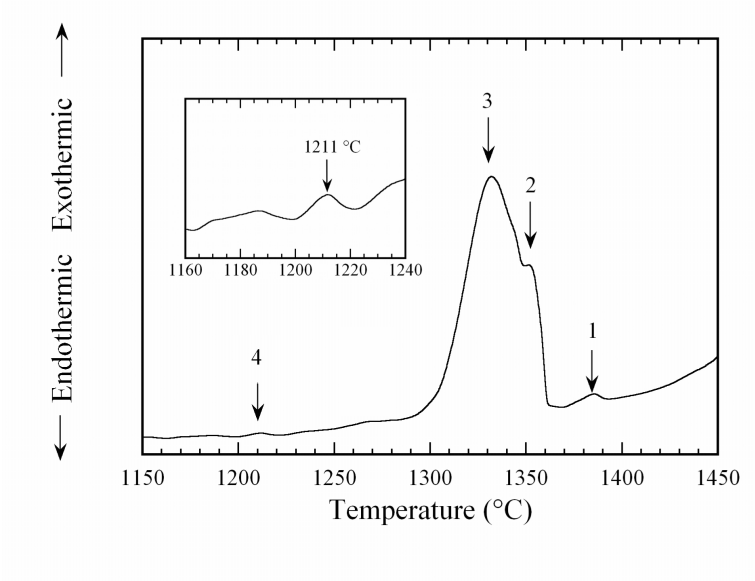

Figure 45: DTA cooling curve showing the various reactions that occur upon cooling from 1450°C including the precipitation of (Ta,Ti)C carbides (1), Ni matrix formation (2-3) and γ' precipitation (4).

no longer be seen as the last of the largest γ' has been dissolved and taken into solution by the matrix. Figure 46(d) shows a microstructure that appears to contain only the "script" carbides in a super-saturated γ matrix. However, at higher magnifications ultra-fine γ' particles ($<0.1\mu$m) are observed. These particle are nucleated during the final cooling step and cannot grow significantly due the rapid quench.

5.3.1.3 Dual-pushrod horizontal dilatometry

An example of a CTE measurement on GTD-111 is shown in Figure 47, which shows that the alloy displays a rapid change in CTE at the point at which the γ' precipitates begin to dissolve. The average solvus temperature was determined to be 1204°C on heating and 1183°C on cooling. The differences between the solvus temperature determined upon heating and cooling can be attributed to energy barriers that are present as energy is required to nucleate new particles upon cooling [2]. This was also found in wrought Ni-alloy experiments [50].

Table 5 summarizes the results obtained by each of the methods. The DTA experiments indicated the temperature range of interest for identifying the γ' solvus. Additional results

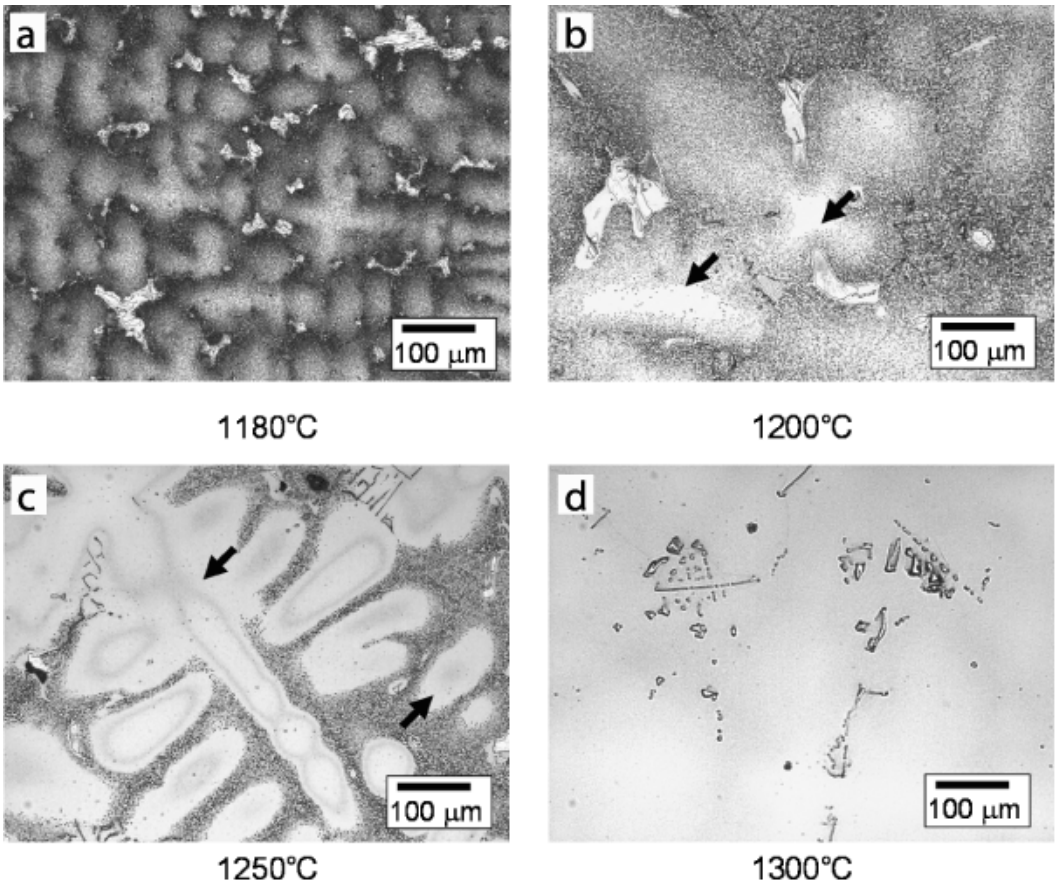

Figure 46: Optical micrographs of heat treated samples showing the dissolution of γ' particles at 1180°C (a), 1200°C (b), 1250°C (c), and 1300°C (d). Areas of interest are denoted by arrows and reflect the dissolution of particles of increasing size as a function of temperature. The smaller particles dissolve first at 1200°C and the largest particles are dissolved after holding at 1300°C.

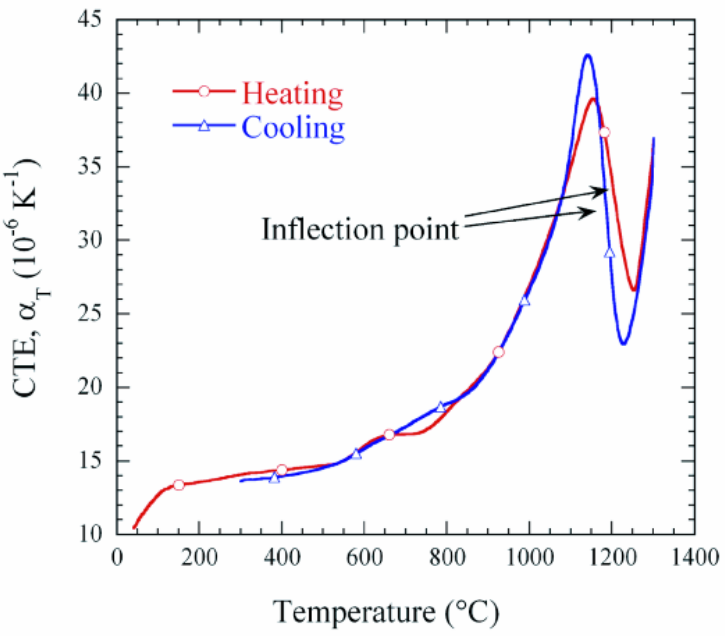

Figure 47: Dilatometry CTE versus T curve showing the difference between heating and cooling for GTD-111 DS [11].

from the DTA yielded several other important temperatures of interest such as the melting temperature of the alloy and the temperature of formation of (Ta,Ti)C. Both the traditional heat treatment/metallography technique and the dilatometry technique identified γ' solvus temperatures that complemented the DTA results. All three methods determined the solvus temperature to be approximately 1200°C.

Table 5: γ' solvus temperatures determined by metallography, dilatometry and DTA.

	γ' Solvus Temperature (°C)			
	Metallography	Dilatometry		DTA
Run	Heating	Heating	Cooling	Cooling
1	-	1207	1181	1211
2	-	1204	1185	1185
3	-	1204	1182	1191
4	-	1202	1183	1185
Average	1200	1204.3	1182.8	1193
Standard Deviation	-	2.1	1.7	10.7

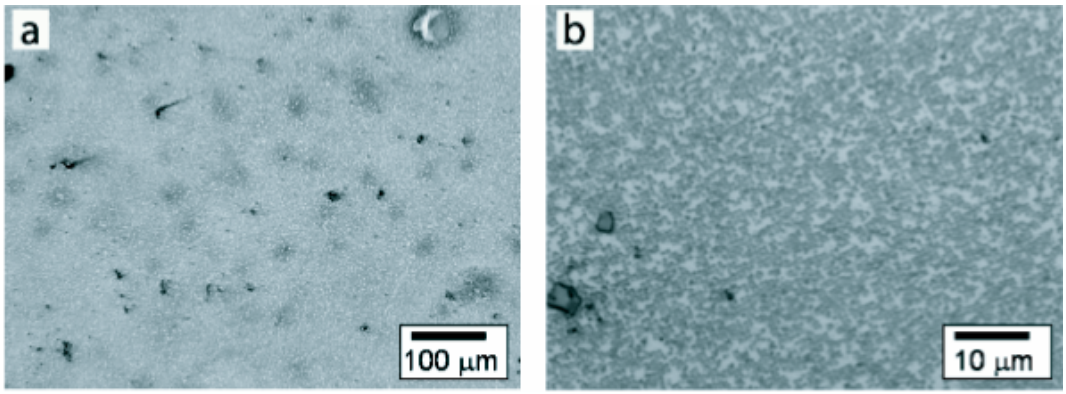

Figure 48: Optical micrographs of a dilatometry sample showing the absence of the as-cast cored dendrite structure (a) and a distribution of small (0.1 μm) γ' particles (b). The interdendritic DPPs were eliminated by the heat-treatment while the carbide remained unaffected.

Figure 48 shows a micrograph taken from a dilatometry specimen after five heating/cooling cycles. The γ' particles are arranged in a uniform distribution of 0.1 μm particles. The micrographs in Figure 48a (dilatometry) and in Figure 46d (traditional heat treatment) show similar microstructures. However, while both show a uniform distribution of γ' particles (i.e. no dendritic variations), the particles in Figure 48a are larger. This is explained by again noting that the cooling rate of the dilatometry specimen was lower than that in the IR furnace (3°C/min and $<$ 100°C/min, respectively), which allowed time for the γ' particles to grow. In terms of convenience, it is clear that dilatometry has several advantages over DTA and traditional metallographic techniques. DTA is useful for rapid estimation of regions of interest provided that the occurring reactions are known and that an ample sample size can be obtained. The dilatometry technique has the benefit of a larger sample size (10 g),as compared to the small DTA sample size (200 mg). This allows the true bulk properties to be measured This is supported by the large difference in uncertainties for dilatometry (1.7°C) and DTA (10.7°C). Dilatometry also provides the opportunity to examine the sample post-tests for microstructural characterization as the larger samples can be sectioned and polished whereas in the case of DTA samples, this kind of sample preparation is difficult due the small sample size. The ability to detect the delayed onset of precipitation reactions, and therefore provide an indication of the barrier to nucleation,

is another benefit of the dilatometry technique over the other techniques primarily because metallography can be overly tedious, and DTA cannot detect the delayed onset due to the sample size and heating/cooling rate sensitivity of the technique.

5.3.2 Dissolution of γ'

Figures 49 and 50 show the microstructures that result after various hold times at 1300°C. It's clear that even after 15 minutes the smaller γ' spherical particles as well as the octets are completely dissolved. The the volume fraction of the larger DPPs however slowly diminishing until hold time exceeds 240 minutes. Figure 51 shows the change in volume fraction of DPPs as a function of time which indicates that a heat treatment at a temperature of 1300°C for 240 minutes is sufficient to "clean up" the interdendritic region to leaves only carbides in these areas.

The Figure also demonstrates that volume fraction of carbides does not change significantly over the range of hold times, which was expected since the carbides are formed at much higher temperatures than 1300°C. This was confirmed by DTA results. The small decrease in carbide volume fractions at the shorter hold time is attributed to the fact that digital analysis on the microstructure can sometimes confuse DPPs with carbides based on how the images are thresholded to isolate the carbide from the matrix. Therefore, as the DPPs are dissolved, the volume fraction of carbides determined through image analysis will be slightly affected.

Another concern when heat treating GTD-111 DS was that the heat treatment itself may destroy the columnar grain structure by homogenizing the material to the point where the secondary dendrites are dissolved or changed through some type of recrystallization process leaving either an equiaxed grain structure or the creation of a single crystal. These circumstances are unlikely due the fact that recrystallization must usually be accompanied with some type of mechanical deformation, and in order to form a single crystal the primary dendrite, which are the most stable, would have to either rotate and align in similar orientation or remelt and grow into a single crystal. Remelting of primary dendrites is not possible as the temperature required would exceed 1350°C. Localized or incipient melting

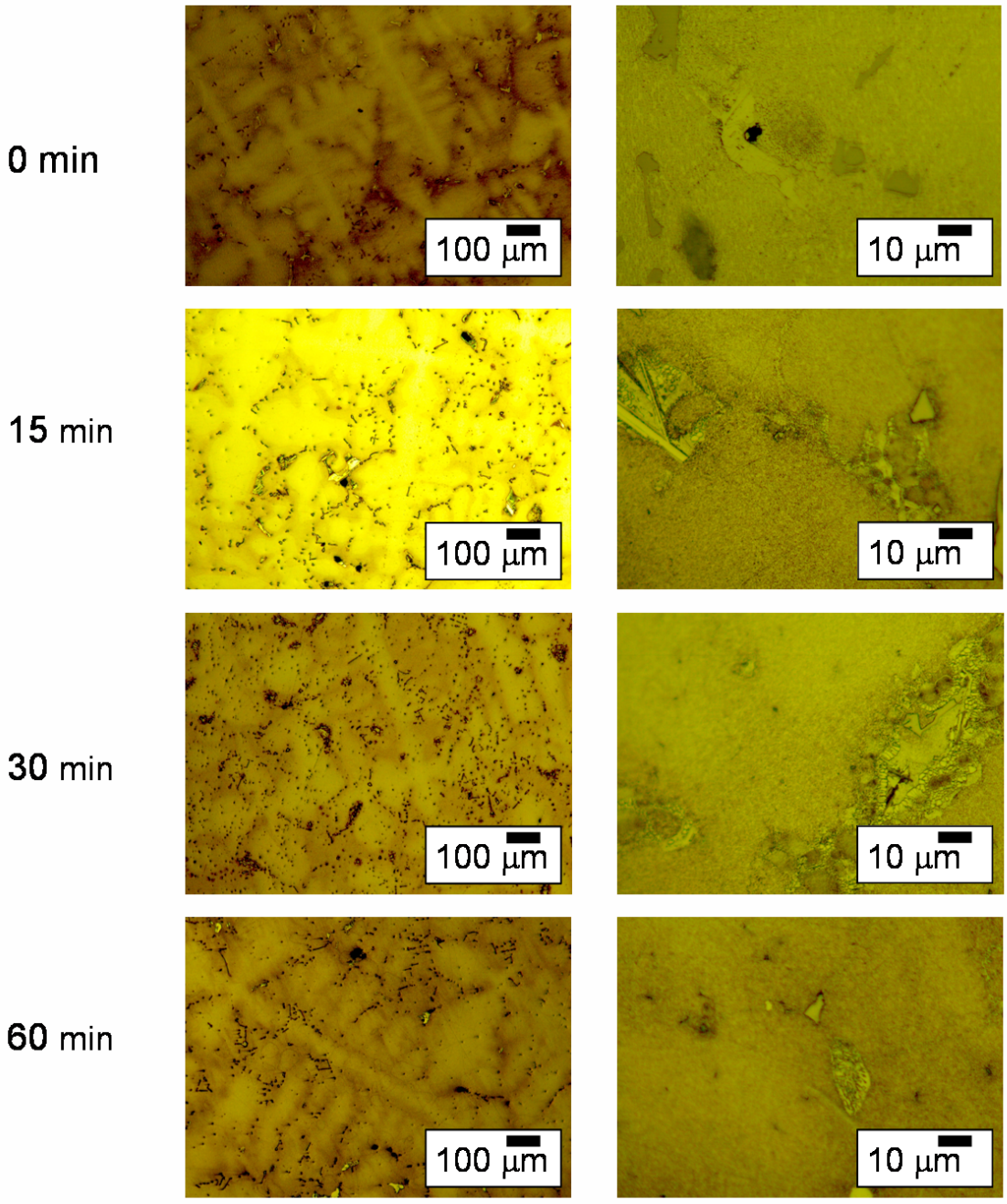

Figure 49: Optical micrographs of GTD-111 DS samples held at 1300°C for 0, 15, 30, 60 minutes, which shows that the DPPs were not eliminated after 60 minutes

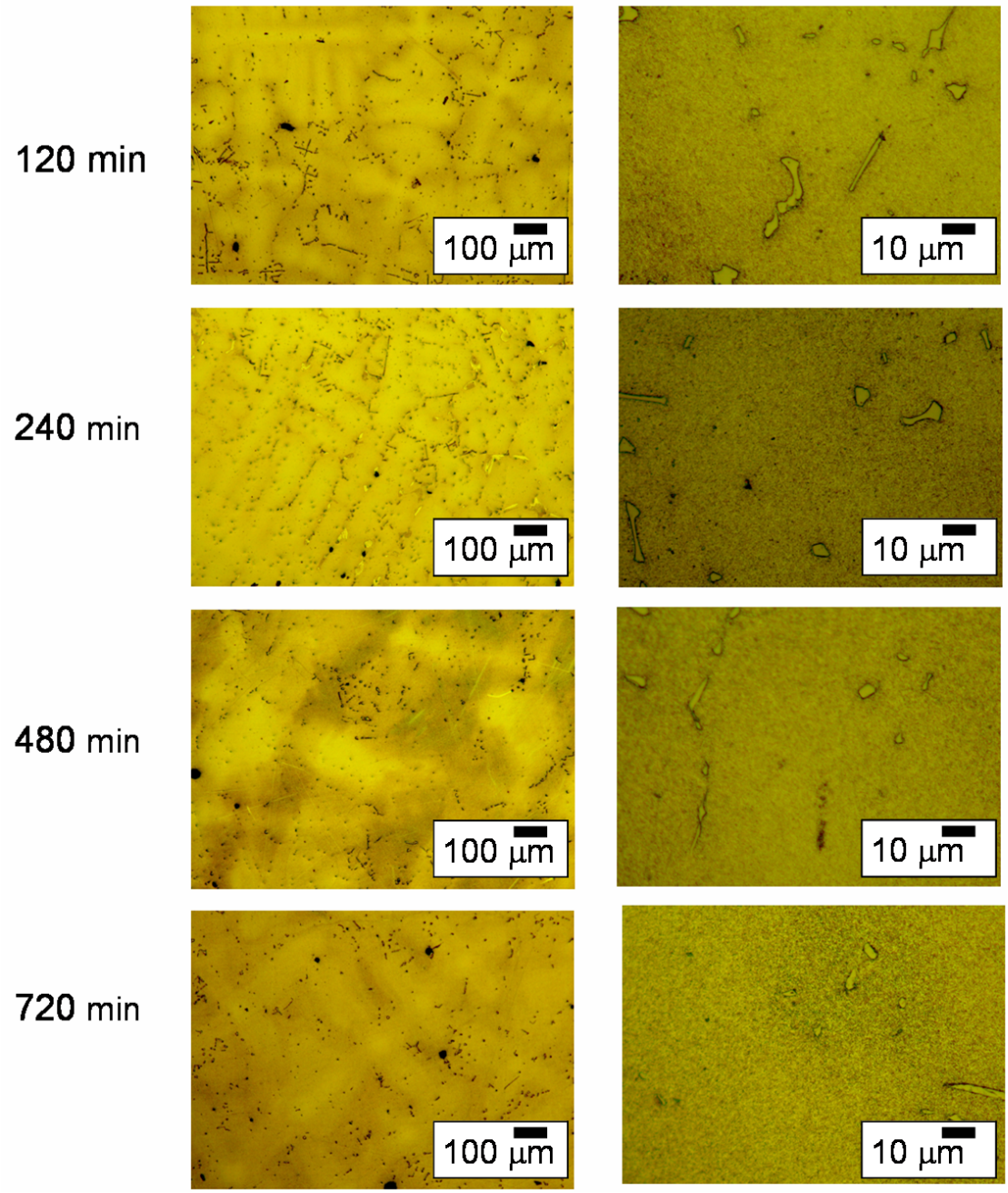

Figure 50: Optical micrographs of GTD-111 DS samples held at 1300°C for 120, 240, 480, 720 minutes, which shows that the DPPs can be eliminated after 240 minutes

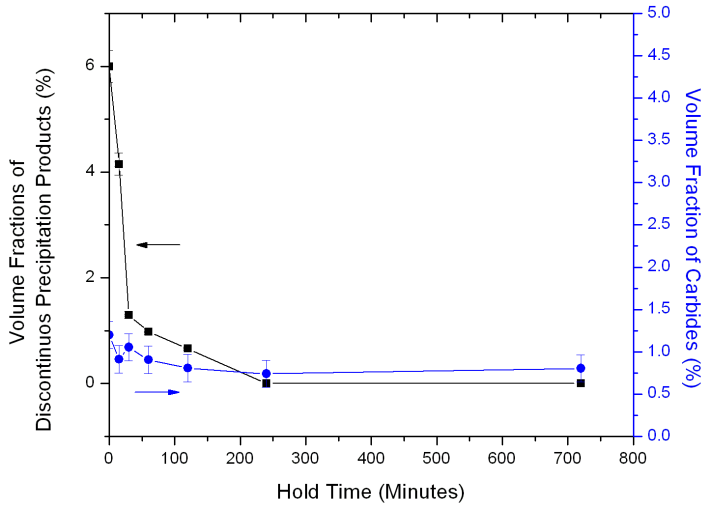

Figure 51: Optical micrographs of GTD-111 DS samples held at 1300°C for 0, 15, 30, 60, 120, 240, 480, and 720 minutes, which shows that the DPPs can be eliminated after 240 minutes.

can be observed in many superalloys [17] which would be able to melt the secondary dendrite arms, however, no incipient melting was observed in this work. It has been shown by Last *et al.* [52] that the columnar structure of twinned, single phase cast Al-Si alloys can be removed through heat treatment after 3 days. In a similar alloy, one that has a multi-phase component such as precipitates in the interdendritic regions, the columnar twins remained stable even after seven days [52]. The reason for this stability was attributes to the pinning of gains boundaries by the non deformable precipitates [52]. It is possible that in GTD-111 DS the non deformable carbide phase serves similar means to preserve the columnar structure of the material. Figures 52 and 53 shows low magnification micrographs of each of the heat treated samples. In each case the primary dendritic structure remains unaffected by the heat-treatments, thus preserving the macro dimensions of the DS grains.

The overall effect of the treatment is to dissolve all the γ' present after the standard industrial heat treatment, including all DPPs, without affecting the columnar grain structure or affecting the volume fraction of carbides. The new microstructure will allow tensile tests to show role of the carbides during failure without the possibility of the DPPs causing

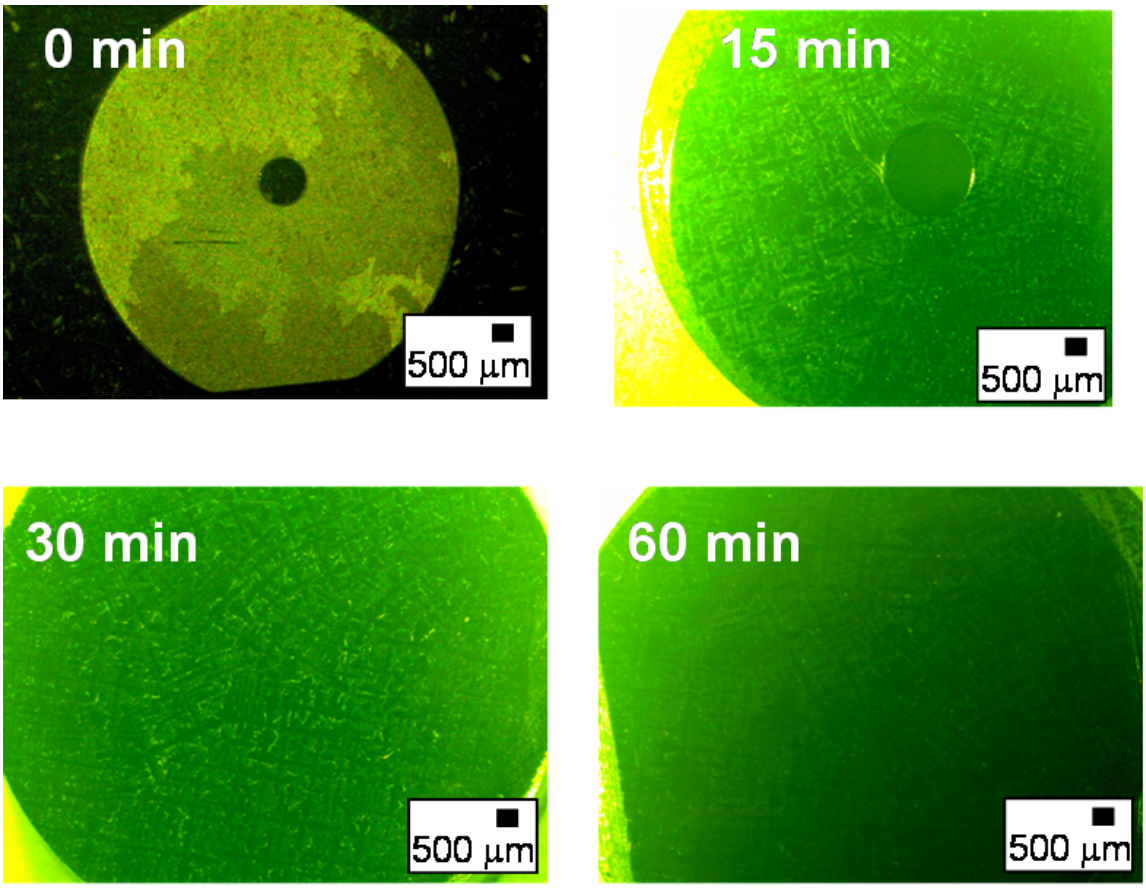

Figure 52: Optical micrographs of GTD-111 DS samples held at 1300°C for 0, 15, 30, and 60 minutes, which shows that the columnar grain structure remains intact throughout all heat-treatments.

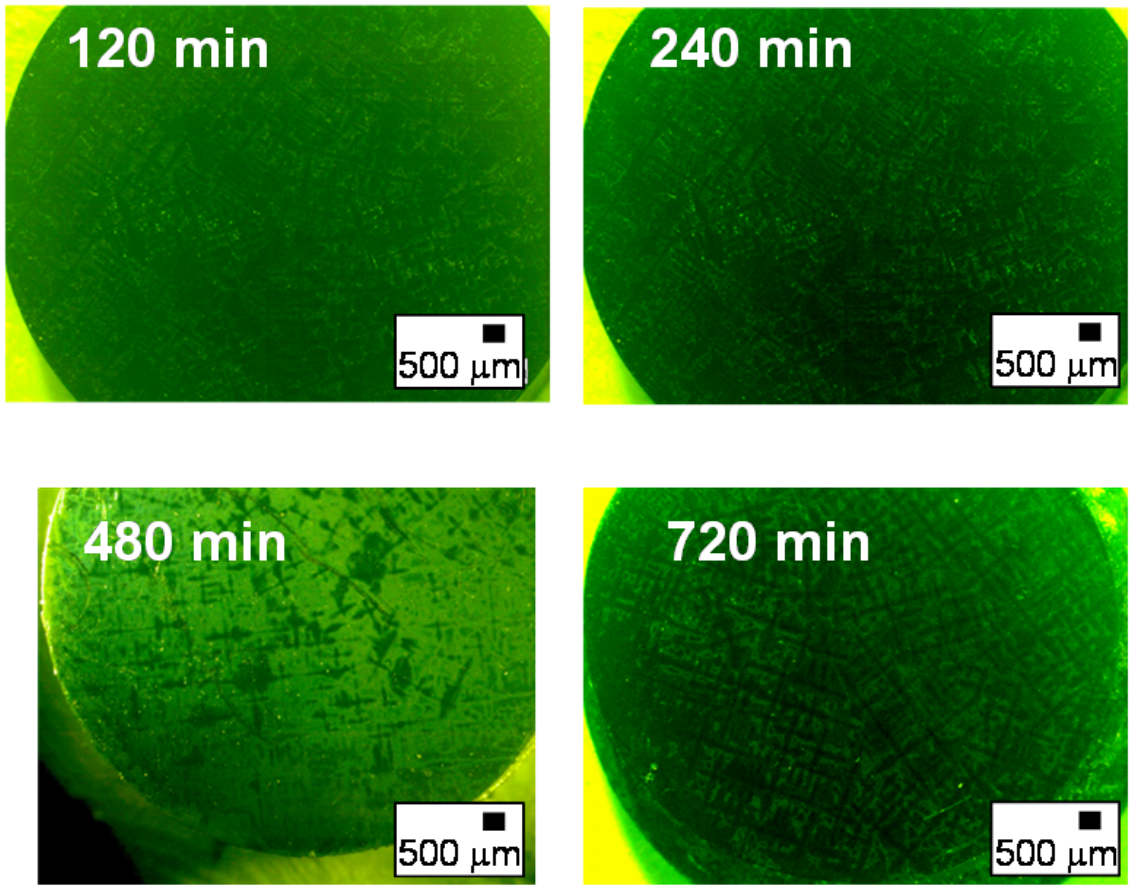

Figure 53: Optical micrographs of GTD-111 DS samples held at 1300°C for 120, 240, 480, and 720 minutes, which shows that the columnar grain structure remains intact throughout all heat-treatments.

fracture. It is expected that the heat-treated sample will exhibit higher strength, due to the uniform γ' particles. However, ductility will suffer as the DPPs, which are mostly responsible for the ductility, are absent. Failure will occur at the brittle carbide phases. This type of study has been observed by Huron *et al.* [20] and Janowski *et al.* [18].

5.4 Conclusions

Three different methods were used to determine the solvus temperature of GTD-111 DS, differential thermal analysis, metallographic observations, and dilatometry techniques. Heat-treatments above this solvus temperature were employed to study the dissolution of γ' and any subsequent effects on the carbide volume fraction and the overall columnar grain structure. The key findings of this chapter are:

1. Each of the three methods used to determine the solvus temperature suggest that the solvus temperature is approximately 1200°C. This validates dilatometry as a method of investigation of as-cast superalloys.

2. Dilatometry also has the ability to detect the delayed onset of precipitation reactions, and therefore the barrier to nucleation

3. Heat treatment at 1300°C after 240 minutes eliminates the DPPs preserving the columnar grain structure and the volume fraction of carbides.

CHAPTER VI

HIGH TEMPERATURE CORROSION KINETICS

The previous chapters have focused on the effect that the columnar grain structure of GTD-111 DS on tensile fracture paths. This chapter evaluates the stress free corrosion properties of GTD-111 DS in both air and H_2S atmospheres. In the case of H_2S, a dependence of the number of grain boundaries and their orientation on the extent of corrosion damage was observed, thus reinforcing the importance of the underlying microstructural features on GTD-111 DS in an IGCC turbine system.

6.1 Background

6.1.1 Oxidation

Stress free oxidation/sulfidation testing on GTD-111 was performed by Gordon *et al.* [12]. These tests were done in a horizontal tube furnace, where disc samples were exposed to both oxidizing and sulfur rich atmospheres for different amounts of times. The samples were sectioned and examined metallographically. Gordon's results for the oxidation tests (Figure 54) show that GTD-111 DS is a chromia (Cr_2O_3)-forming alloy. This chromia layer serves as a protective barrier to further oxidation, which gives rise to parabolic oxidation behavior. Beneath the chromia layer is a thin compact film of rutile (TiO_2), followed by a region of internally oxidized alumina (Al_2O_3) particles. Based on Ellingham data (Figure 55), alumina should be the dominant scale as it is the most stable oxide. However, most of the Al needed to form the scale is in solid solution with the (γ') phase. To form both TiO_2 and Al_2O_3, the Al and Ti are stripped from the γ', which is a less stable phase as shown by the $Ni_3(Ti, Al)$ lines in Fig. 55, leaving a precipitate free zone between the scales and the base metal.

Figure 56 shows an example of the temperature dependence of parabolic oxidation of Co. The dependence of the parabolic rate constant (k_p) is an Arrhenius relationship,

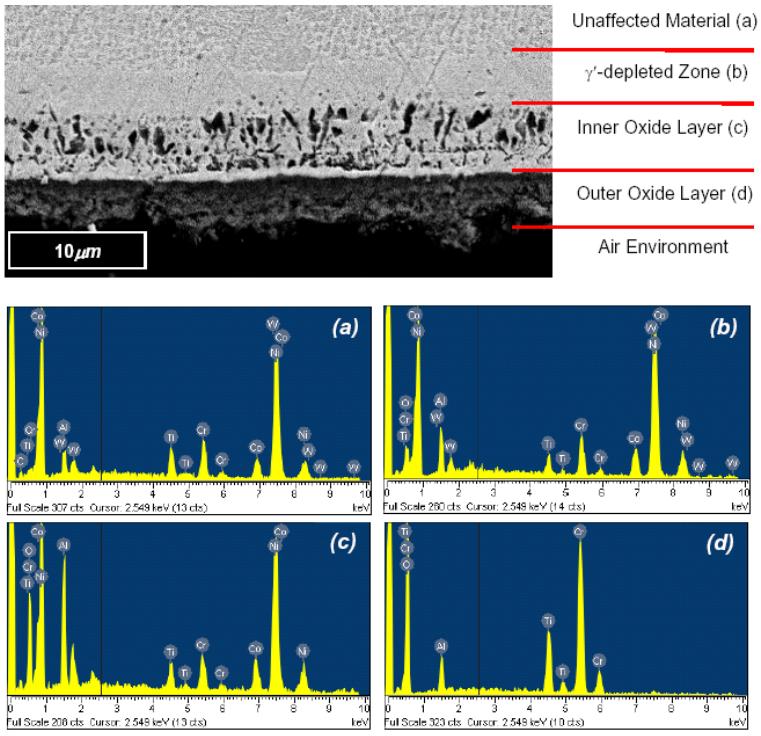

Figure 54: SEM/EDS analysis on a cross section of GTD-111 DS exposed in air at 982°C for 312 hours [12].

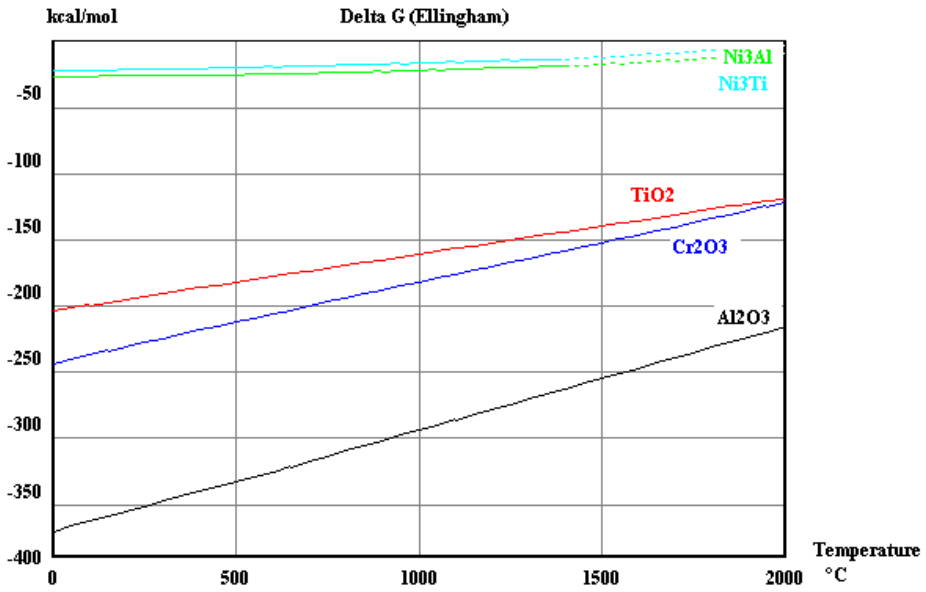

Figure 55: Ellingham diagram showing the relative stabilities of oxides scales compared with γ' (Ni_3(Ti,Al)) Diagram was calculated using HSC 5.1 software [13].

$$k_p = k_0 e^{\frac{-Q}{RT}} \tag{22}$$

where k_0 is a constant, Q is the activation energy, R is the gas constant, and T is temperature. Figure 56 is a log plot of k_p versus 1/T. The activation energy can be determined by the slope of the lines according to equation 22. The figure also illustrates how the partial pressure of O_2 affects k_p and Q. As P_{O_2} increases, k_p increases. However, there is little change in the slopes of the plots which indicates that the activation energy (Q) is independent of oxygen partial pressure [14].

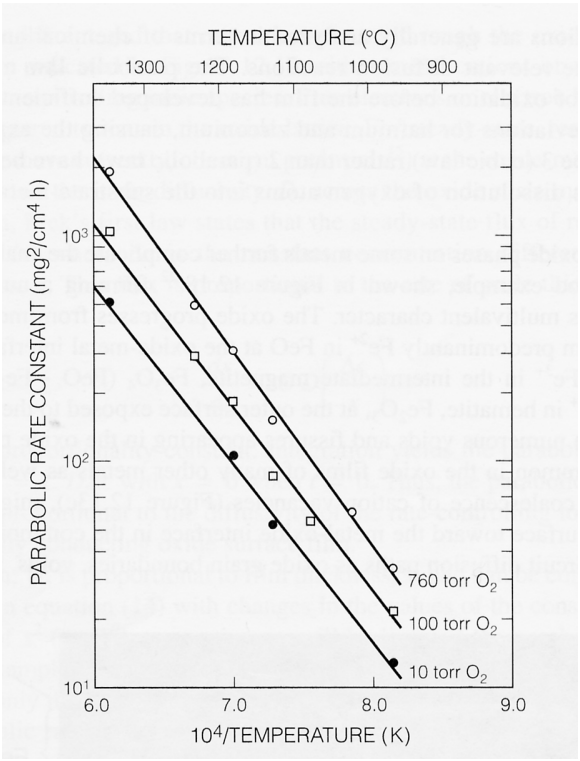

Figure 56: Log of parabolic rate constants versus 1/T for cobalt at different oxygen pressures [14].

6.1.2 Sulfidation

In IGCC systems the syngas environment is composed of mostly H_2, CO, CH_4, H_2O and H_2S in various amounts depending on the combustible material used to drive the turbine (ie. coal, black liquor etc). When considering corrosion, the key effluent gas is H_2S. This

is due to the fact that the other components are not largely corrosive gases and break down during combustion to form CO_2 and water vapor. While these gases do not participate in the corrosion reactions, they will dictate the partial pressure of H_2S gas, which will affect the extent of corrosion. For this work a H_2S concentration of 100 ppm was chosen. The corrosion behavior of nickel alloys in H_2S is known to be aggressive as was stated in Chapter 2. The leading cause for this poor corrosion resistance is the formation of a low melting eutectic (figure 57) such as Ni_3S_2 which melts at 745°C, and NiS, which melts at 975°C [14]. Formation of liquid films further dissolves the Ni base metal and enhances metal loss through liquid metals corrosion mechanisms [53]. The addition of water vapor to H_2S adds

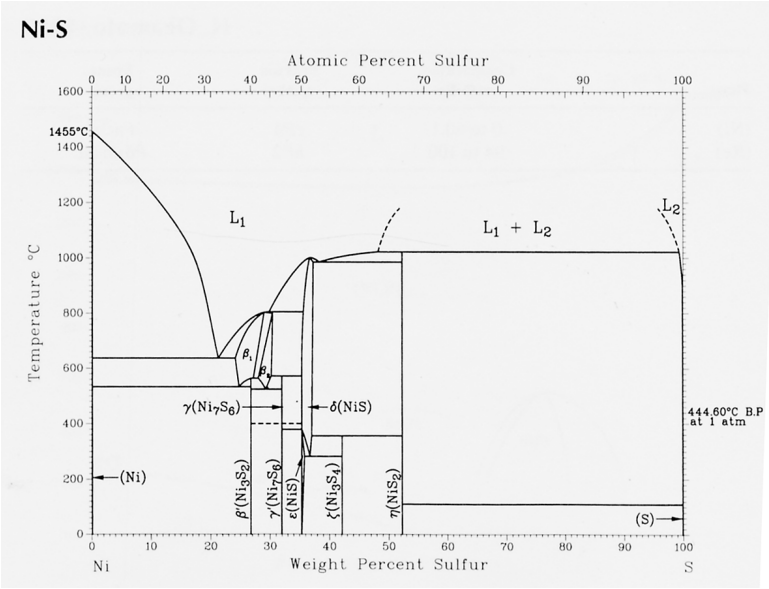

Figure 57: Ni-S phase diagram [15]

a competitive nature to the corrosion process. The water vapor provides ample O_2 to form protective oxide films. However, in cases where molten sulfides are able to form, the oxides are destroyed and corrosion continues. Figures 58 through 60 show phase stability diagrams at three temperatures. As temperature increases, the partial pressure of S needed to form Ni_3S_2 decreases. It can also be seen that Ni_3S_2 is the first nickel sulfide to be formed.

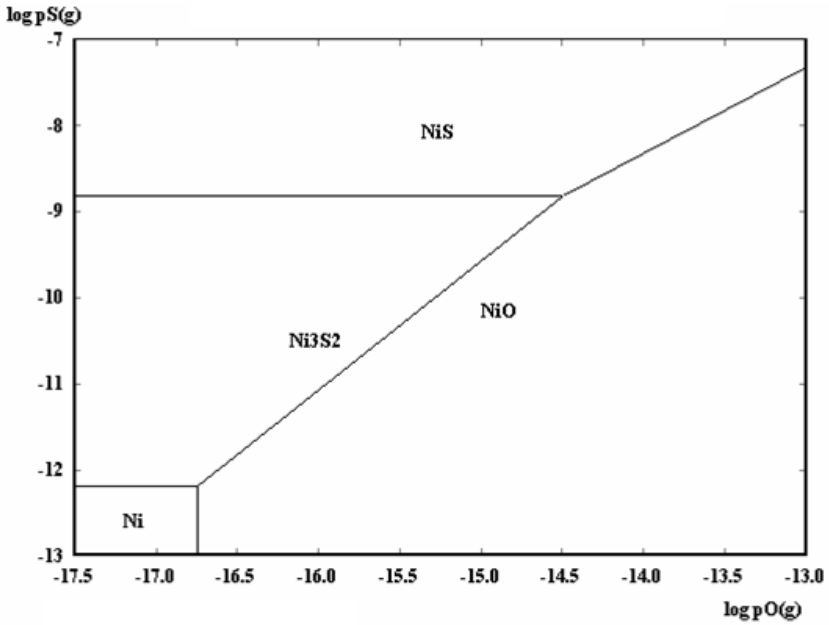

Figure 58: Ni-S-O stability diagram at 760°C (1400°F). Diagram was calculated using HSC 5.1 software [13].

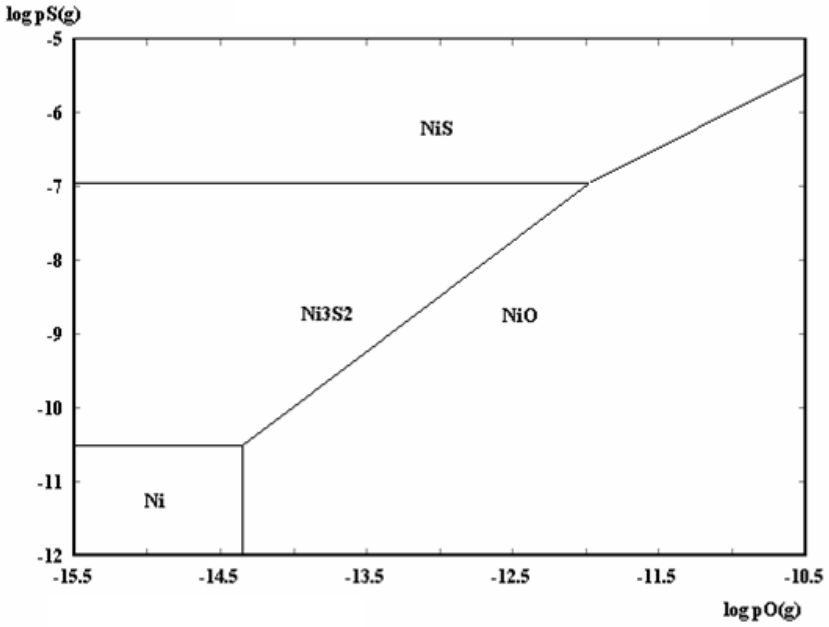

Figure 59: Ni-S-O stability diagram at 871°C (1600°F)Diagram was calculated using HSC 5.1 software [13].

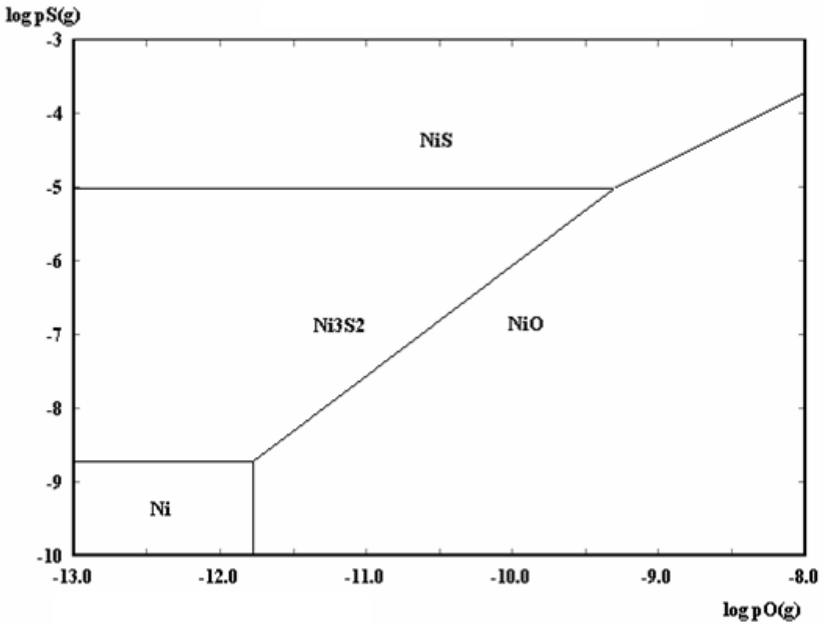

Figure 60: Ni-S-O stability diagram at 1038°C (1900°F. Diagram was calculated using HSC 5.1 software [13].

6.2 Experimental Procedure

6.2.1 Thermogravimetric Analysis

To study high temperature corrosion of GTD-111 DS in atmospheres similar to those found in steam and IGCC turbine systems, continuous TGA studies were conducted. Rectangular samples weighing between 4 and 6 (1.27 x 1.27 x 0.5 cm) grams were cut and polished to #600 SiC grit. A Cahn microbalance was used to continuously monitor the weight change as a function of time. Samples that were hung inside of a vertical tube furnace using Pt wire as shown in Figure 61. Three test temperatures were selected for this work, 760°C, 871 °C, and 1038 °C. In the case of the high temperature tests (1038 °C) it is important to note that a temperature shift of ± 15°C was measured after the tests were completed. It was determined through comparison that tests repeated in this range showed no significant difference in oxidation behavior, and thus, results can be considered valid tests with little concern of error. Four test atmospheres were chosen. These include both dry air and dry N_2 with 100 ppm H_2. The two remaining atmospheres included water vapor, since water almost certainly present in any in-use system. Water was introduced in these tests by

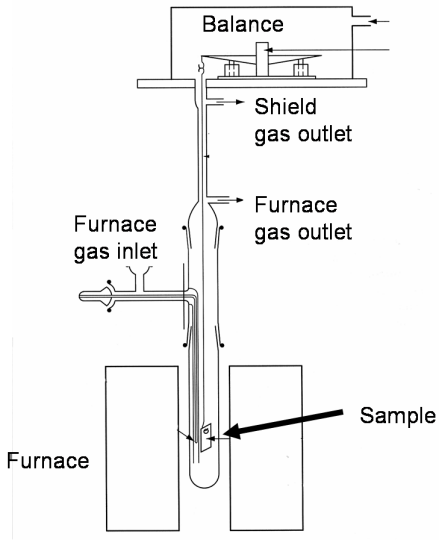

Figure 61: Diagram of a TGA capable of tests in corrosive gases [7].

bubbling through distilled water prior to being passed into the TGA. Table 6 is a list of all samples tested and their respective test atmospheres, which will be refered to as "dry" and "wet" conditions for the remainder of this chapter. The duration of each test was 100 hours.

Table 6: Test matrix for TGA tests

°C	°F	Atmosphere
760	1400	Dry Air
871	1600	Dry Air
1038	1900	Dry Air
760	1400	Air + H_2O
871	1600	Air + H_2O
1038	1900	Air + H_2O
760	1400	N_2 w/100 ppm H_2S
871-1	1600	N_2 w/100 ppm H_2S
871-2	1600	N_2 w/100 ppm H_2S
871-3	1600	N_2 w/100 ppm H_2S
1038	1900	N_2 w/100 ppm H_2S
760	1400	N_2 w/100 ppm H_2S+H_2O
871	1600	N_2 w/100 ppm H_2S+H_2O
1038	1900	N_2 w/100 ppm H_2S+ H_2O

6.2.2 X-Ray Diffraction and SEM Metallographic Analyses

After each TGA test the sample was removed from the furnace and placed in a Phillips x-ray diffractometer to identify the surface scales that formed during the test. SEM imaging and EDS x-ray mapping were used on sectioned samples to map the outer scales and identify any sub-scales or internal oxidation.

6.3 Results and Discussion

6.3.1 Oxidation

The weight gain as a function of time for GTD-111 DS samples exposed to dry air is shown in Figure 62. For each test temperature there is a parabolic trend to the weight gain. A plot of weight gain squared versus time (Figure 63) shows a straight line for each test temperature. The slope of each line is the parabolic rate constant, k_p, at the given test temperature. Figures 64 through 66 are SEM micrographs accompanied by EDS linescans that identify the major oxide scales formed after 100 hours in dry air. The outer most surface is a chromia (Cr_2O_3) layer followed by a thin compact film of rutile (TiO_2). It is suggested that the rutile (TiO_2) layer plays a major role in protecting the alloy especially at higher temperatures ($> 1000°$C) where Cr_2O_3 volitizes to form CrO_3 gas and can no longer protect the alloy [7]. Internally oxidized alumina (Al_2O_3) particles are present beneath the other oxide scales.

Similar micrographs (Figure 67) were obtained for samples oxidized in wet air and show the same oxide scales. Figure 68 is an example of an x-ray map confirming the presence of a thin rutile (TiO_2) layer between the outermost Cr_2O_3 layer and the internally oxidized Al_2O_3 particles. Overall, the results suggest that Cr_2O_3 is major protective scale supported by the (TiO_2) layer. At temperatures greater than 1000°C there is a competitive process where the growth rate of the Cr_2O_3 scale must be greater than rate of volitizion. In such cases the role of TiO_2 in protecting the alloy is enhanced to preserve the parabolic oxidation kinetics.

Figure 69 shows the oxidation behavior for samples tested in wet air that was obtained when dry passed through distilled water prior to being introduced to the furnace. Figure 70

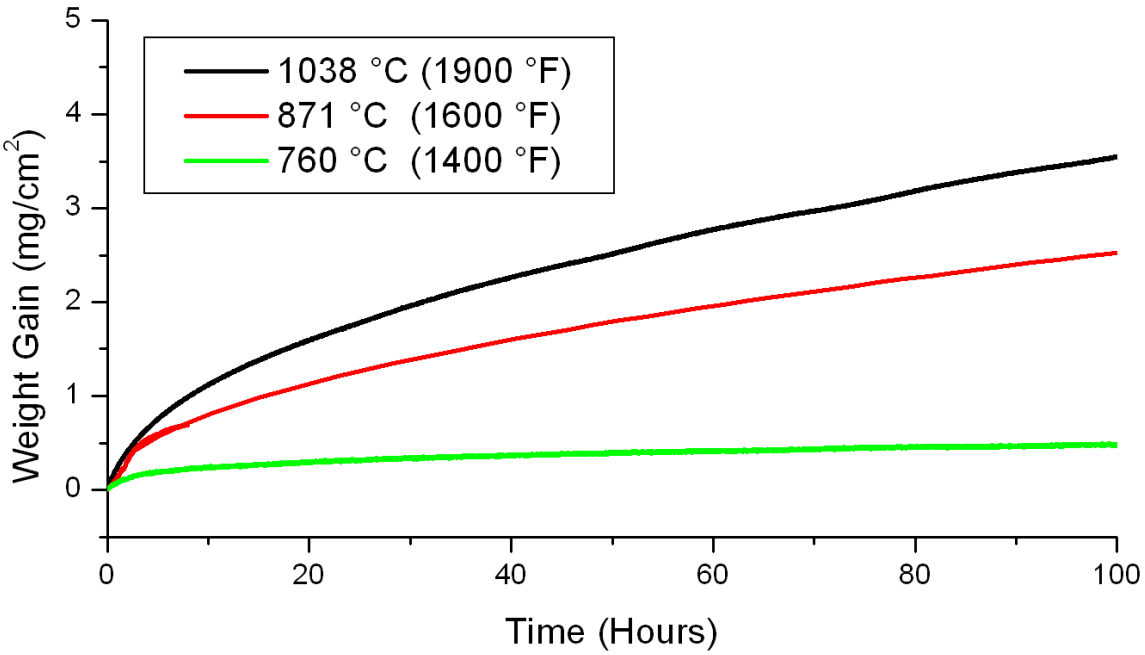

Figure 62: Weight gain versus T for GTD-111 DS at 760°C (1400°F), 871°C (1600°F), and 1038°C (1900°F) in dry air.

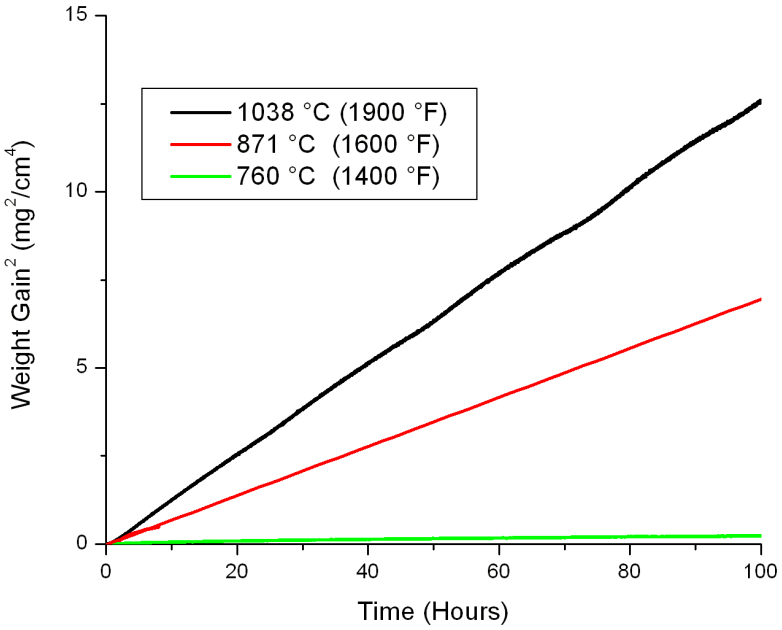

Figure 63: Weight gain^2 versus T for GTD-111 DS at 760°C (1400°F), 871°C (1600°F), and 1038°C (1900°F) in dry air.

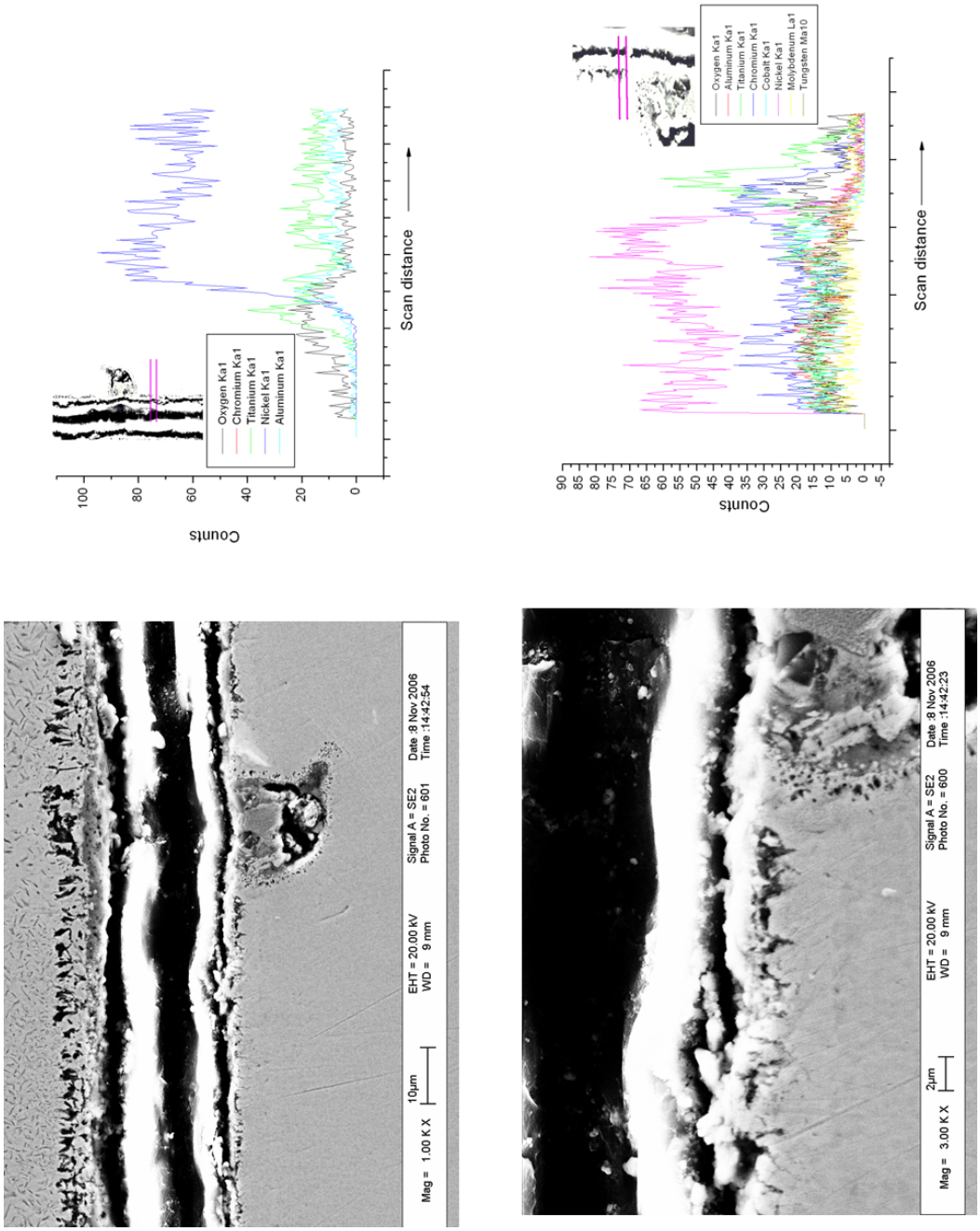

Figure 64: SEM micrographs and EDS linescan of a GTD-111 DS samples tested at 760°C (1400°F) in dry air.

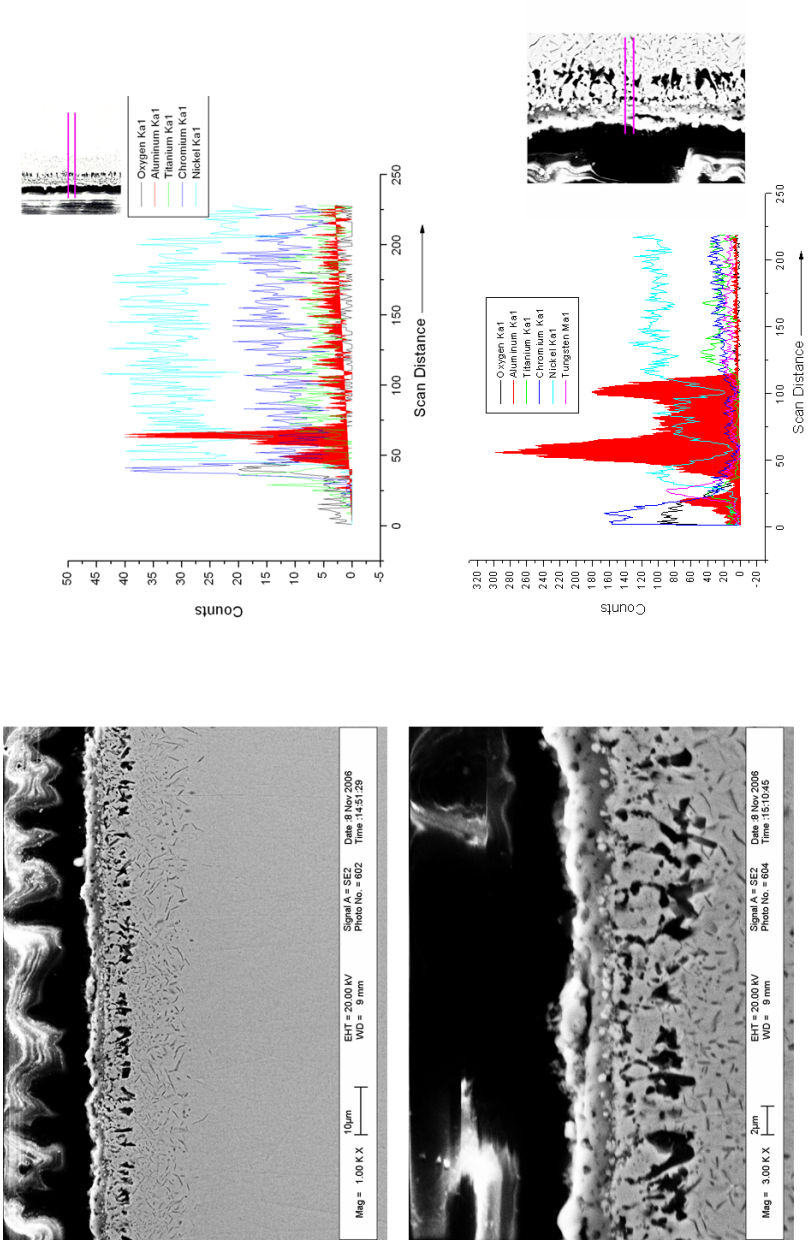

Figure 65: SEM micrographs and EDS linescan of a GTD-111 DS samples tested at 871°C (1600°F) in dry air.

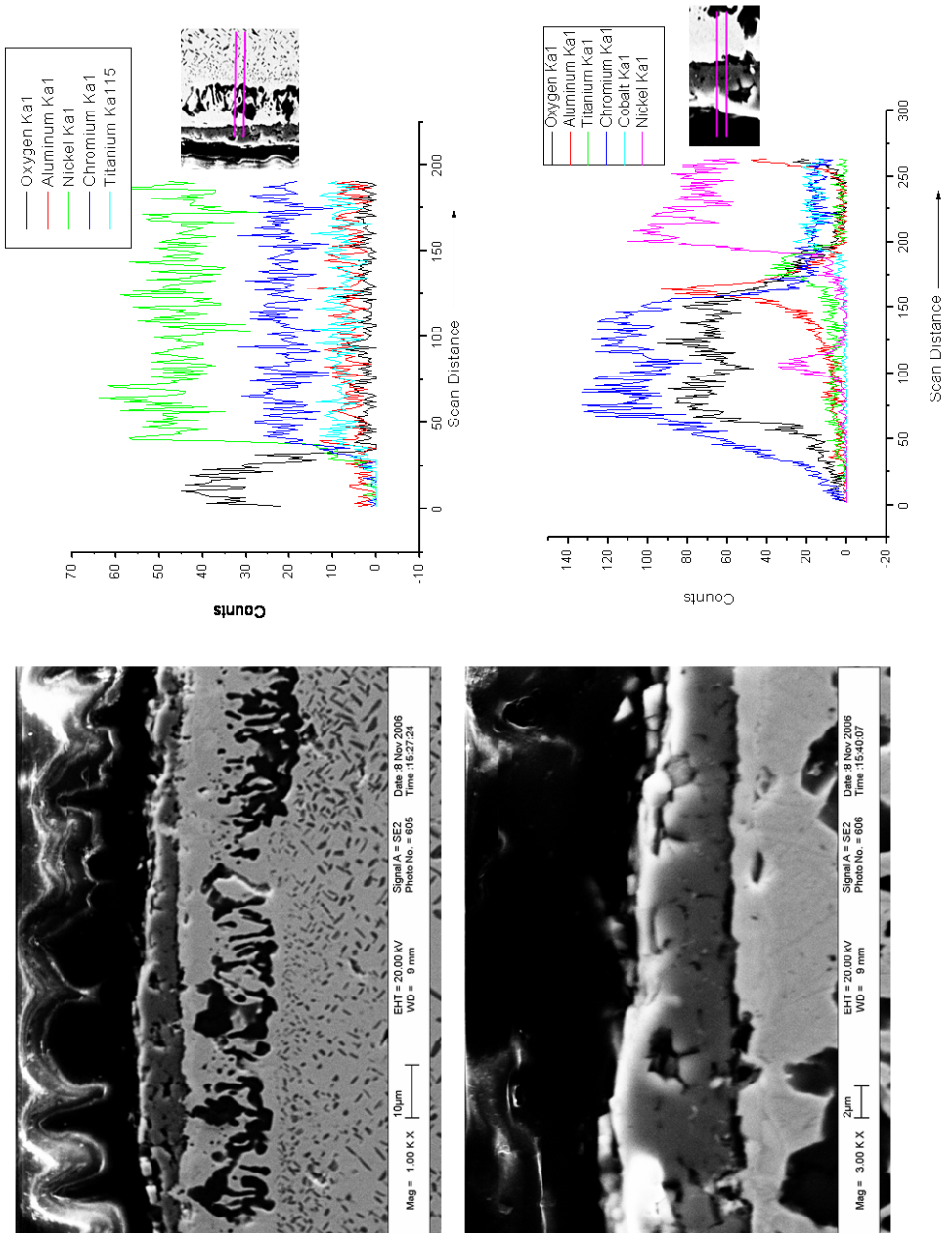

Figure 66: SEM micrographs and EDS linescan of a GTD-111 DS samples tested at 1038°C (1900°F) in dry air.

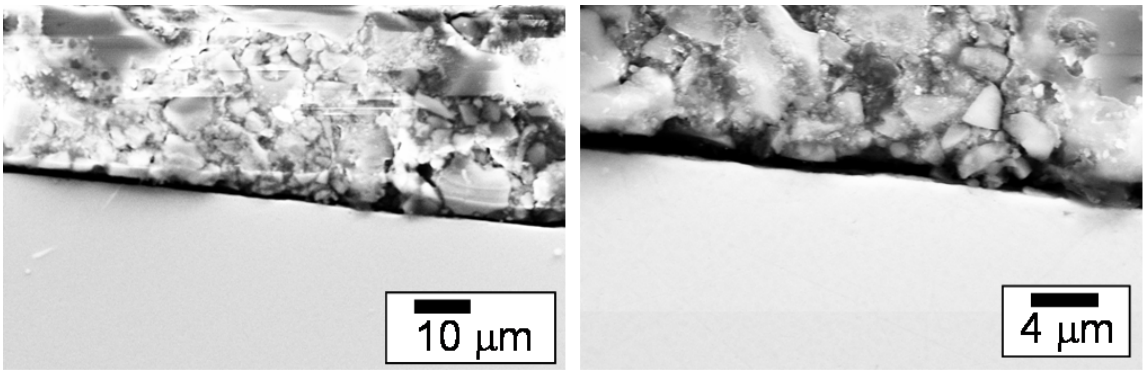

760°C

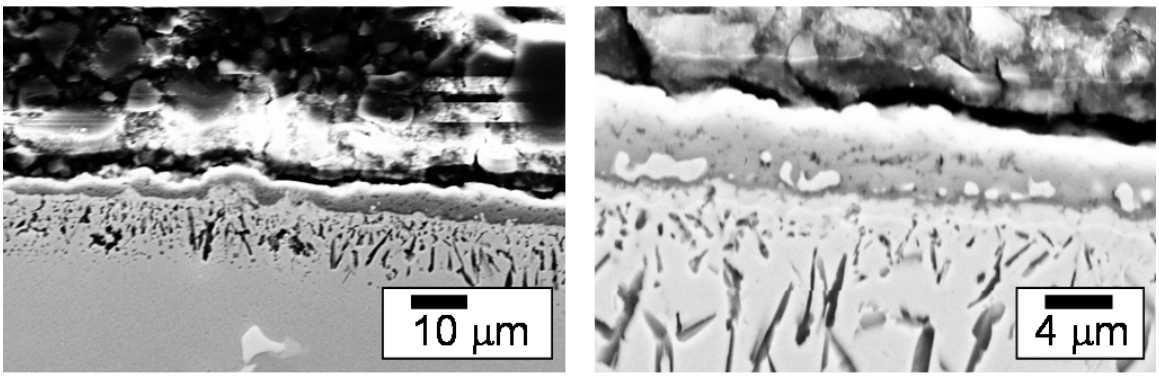

871°C

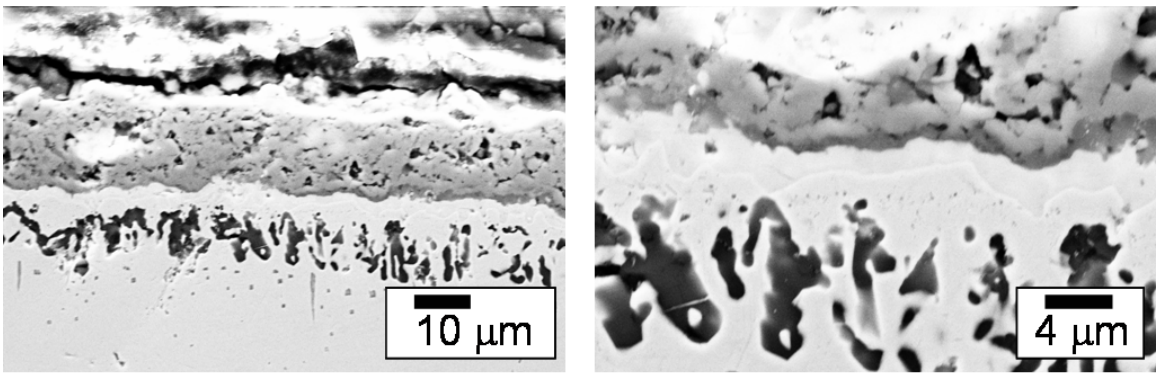

1038°C

Figure 67: Micrographs of GTD-111 DS tested at 760°C (1400°F), 871°C (1600°F), and 1038°C (1900°F) in wet air.

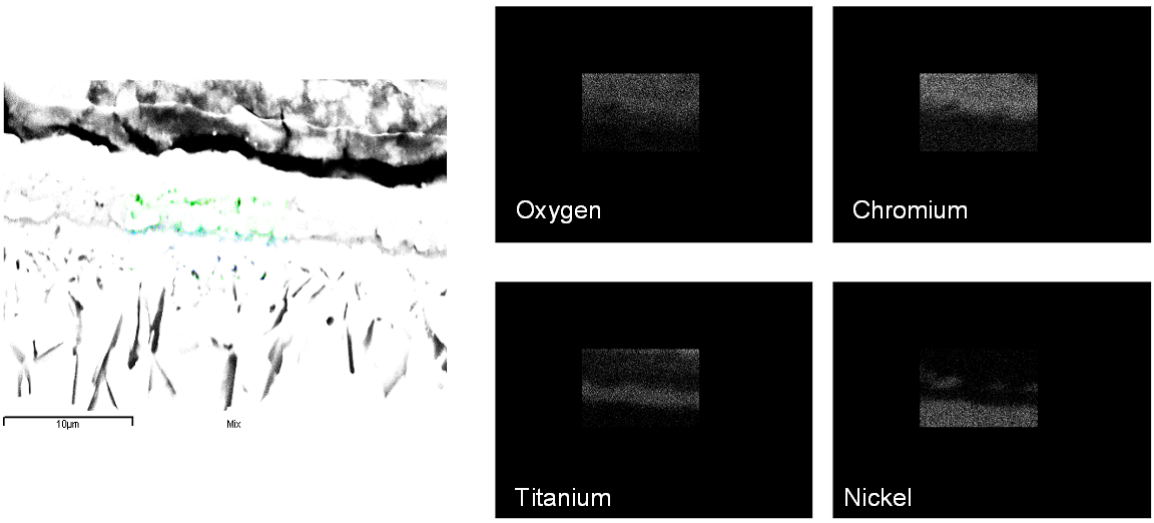

Figure 68: EDS x-ray map of a GTD-111 DS sample tested at 871°C (1600°F) in wet air.

is an Arrehenius plot of the parabolic rate constants obtained for tests conducted in both dry air and air with water vapor. The increase in O_2 pressure causes an increase in k_p and only a slight change in activation energy, which is summarized in Table 7. The value for Q obtained in this work is comparable to those determined by Gordon's isothermal oxidation tests. [12]

Table 7: Oxidation parameters obtained for GTD-111 DS in air

Temperature		Dry Air	Wet Air
°C	$°F$	k_p (mg^2/cm^4h)	k_p (mg^2/cm^4h)
760	1400	0.002	0.004
871	1600	0.0697	0.01098
1038	1900	0.1248	0.12386
Q (kjoules/mole)		71.1	63.8

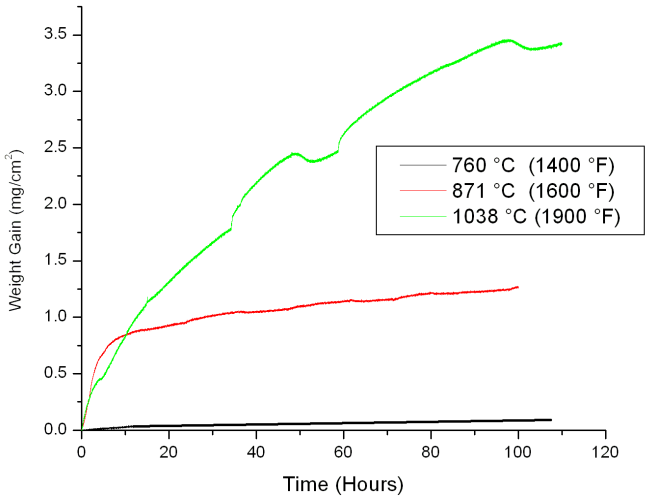

Figure 69: Weight gain versus T for GTD-111 DS at 760°C (1400°F), 871°C (1600°F), and 1038°C (1900°F) in wet air.

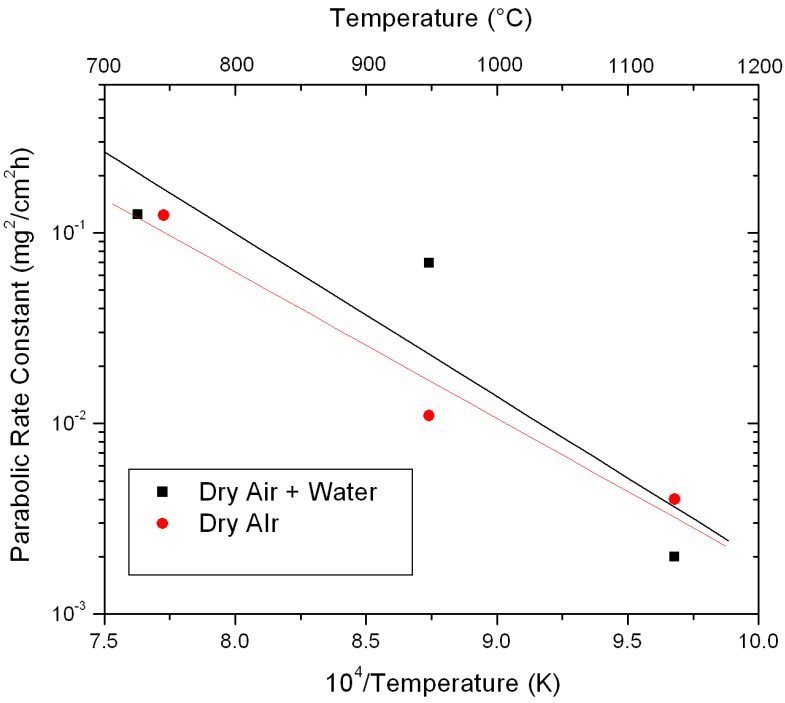

Figure 70: Arrhenius plot of parabolic rate constants versus 10^4/T for GTD-111 DS in dry air and dry air/water cases.

6.3.2 Sulfidation

The TGA results for GTD-111 DS tested in dry N_2 100 ppm H_2S are shown in Figure 71. The weight gain at 760°C proceeds linearly until the weight nearly doubles (45% gain). Massive damage was experienced by the sample, resulting in the sample splitting in half. This was attributed to the formation of liquid sulfides in a grain boundary and is detailed further in section 6.3.4 of this chapter. In the cases of samples tested at 871°C, para-linear oxidation was observed. A protective barrier is initially formed and remains intact for approximately 50 hours, at which point breakdown of the film occurs and the weight gain continues in a linear fashion. It is suggested that breakdown of the film is due to "slagging" mechanism in which molten NiS destroys the barrier and weight gain continues. Figure 72 shows large spherical bubbles of NiS, as was confirmed using electron dispersive x-ray spectrometry. Several of these bubbles appear to burst, suggesting that a boiling reaction is taking place when liquid NiS is present. These bubbles are also observed in the 871°C and 1038°C samples. No breakdown of the scale was observed in the 1038°C sample and the overall weight gain was less than both the 760°C and 871°C samples. However, NiS can be volatile at higher temperatures. It is suggested that the NiS is boiling off of the sample as time continues. Two reactions taking place. The first is the formation of sulfide scales that account for the weight gain. The second reaction is the volatization of this scale as the molten sulfide layer boils off of the surface. This is supported by small NiS spheres and a relatively clean surface on the 1038°C sample (Figure 72). SEM micrographs of samples tested in N_2 with 100 ppm H_2S are shown in Figures 73 through 75. The experimental configuration used in this work was unable to monitor the volume of material that may boil off the sample. Hence, weight gain alone cannot represent the degradation of the material since weight is being simultaneously gained and lost. To account for the damage to samples tested at 1038°C, samples were exposed at 1038°C in N_2 for varying amounts of time. After testing, the weight of these samples was measured, then the outer scale was removed by sand blasting. This allowed the amount of metal that was lost in the corrosion process, as a function of time, to be determined, which is shown in Figure 76.

Clearly as the exposure time increases, metal is being consumed, either forming a sulfide

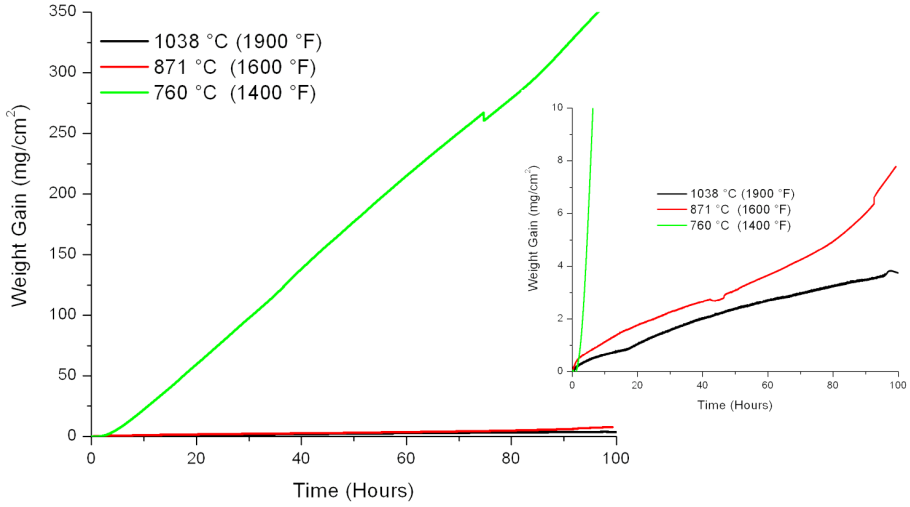

Figure 71: Weight gain versus T for GTD-111 DS at 760°C (1400°F), 871°C (1600°F), and 1038°C (1900°F) in N_2 with 100 ppm H_2S.

scale that remains on the sample, which accounts for the weight gain measured by the TGA, or forming a molten sulfide that volatizes, leaves the sample and is lost in the exhaust of the experiment. At this time it is important to also state that the differences between these three curves may also be largely dependent on the number of grain boundaries that are present in each sample as it was noticed that grain boundaries are preferentially attacked due to enhance diffusion. Section 6.3.4 of this chapter is devoted to the role of grain boundaries in corrosion of GTD-111 DS.

The addition of water vapor to the N_2 with 100 ppm H_2S gas mixture introduced an O_2 source, allowing the formation of protective oxides that further hinder attack by H_2S. In fact, pre-oxidized nickel based superalloys have been shown to be more resistant to H_2S due to compact oxide films [14, 7, 53].

Figure 77 is a plot of the weight gain as a function of time for GTD-111 DS in N_2 with 100 ppm H_2S bubbled through distilled water. At room temperature, the solubility of H_2S in water is minimal [54], which ensures that only water vapor was introduced to the gas stream and that sulfur was not being trapped in the water. Parabolic kinetics were observed for the 760°C. The total weight gain in the atmosphere consisting of wet N_2 with 100 ppm

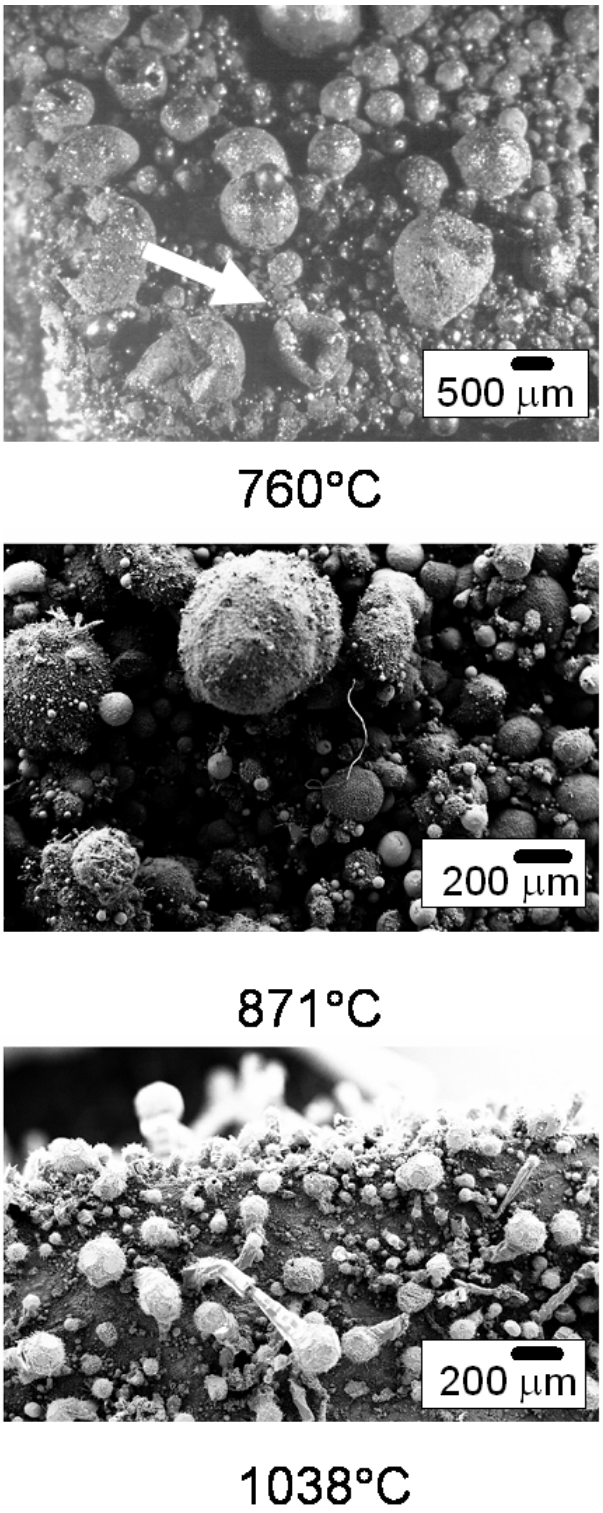

Figure 72: Micrographs of samples tested at 760°C (1400°F), 871°C (1600°F), and 1038°C (1900°F) in N_2 with 100 ppm H_2S, which show NiS spheroids. These spheroids were formed as the molten sulfide cooled after the test. The relative size of the spheres decreased as temperature increased, which is attributed to increased boiling kinetics. The arrows points to bubbles that have burst and frozen on the surface of the samples.

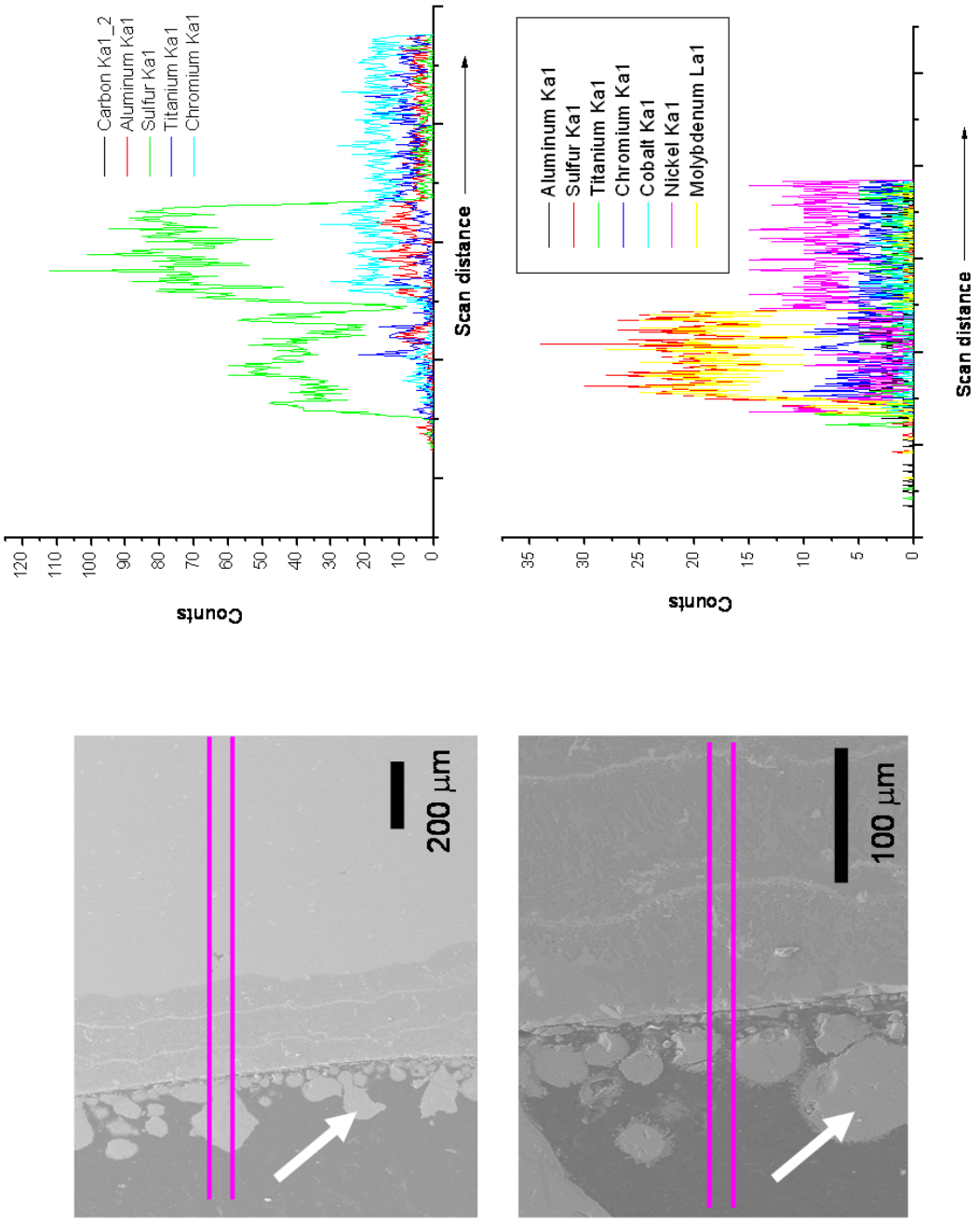

Figure 73: SEM micrographs and EDS linescan of a GTD-111 DS samples tested at 760°C (1400°F) in N_2 with 100 ppm H_2S. The arrows denote solidified NiS spheres.

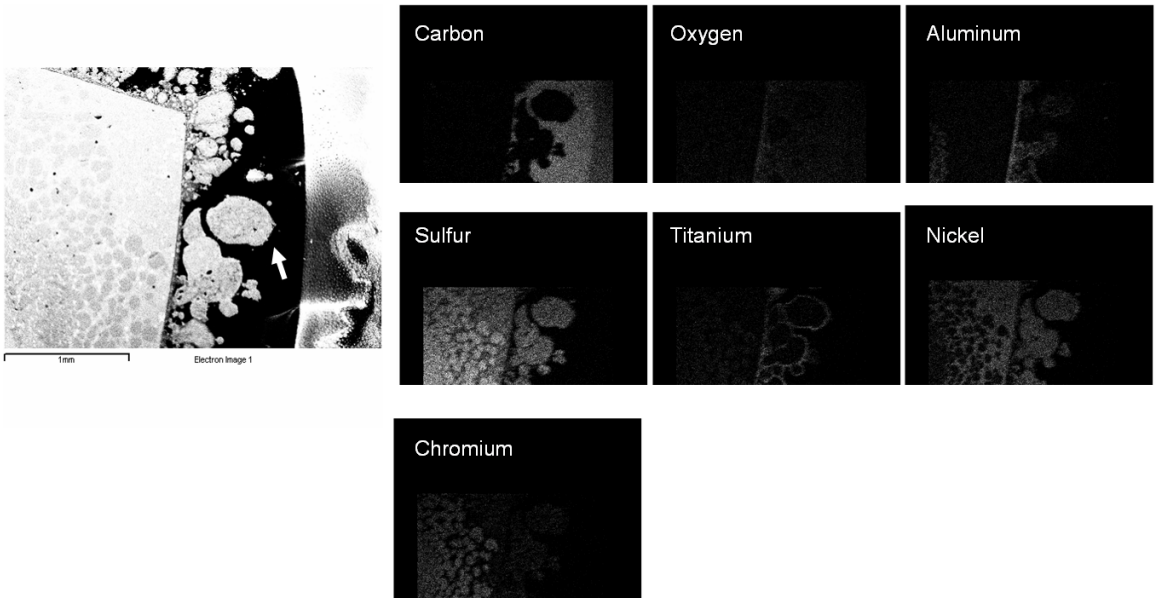

Figure 74: EDS x-ray map of a GTD-111 DS sample tested at 871°C (1600°F) in N_2 with 100 ppm H_2S. The arrows denote solidified NiS spheres.

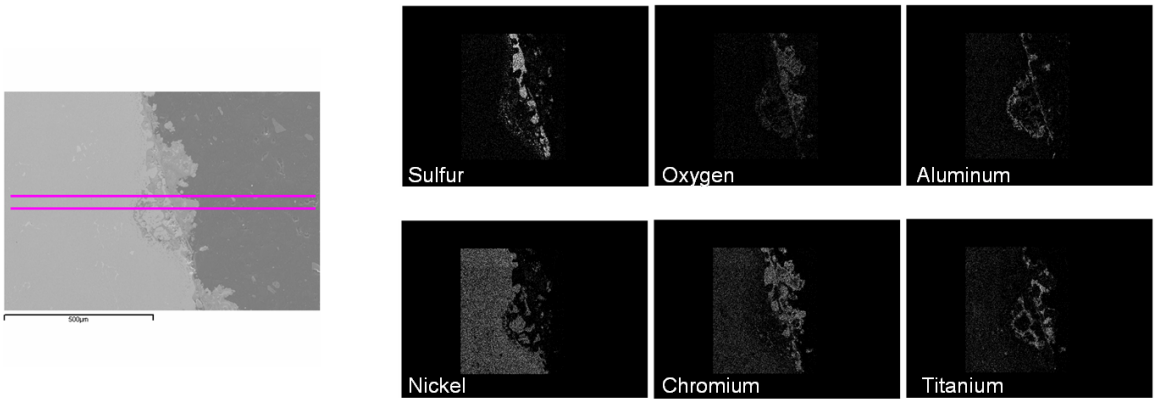

Figure 75: EDS x-ray map of a GTD-111 DS sample tested at 1038°C (1900°F) in N_2 with 100 ppm H_2S.

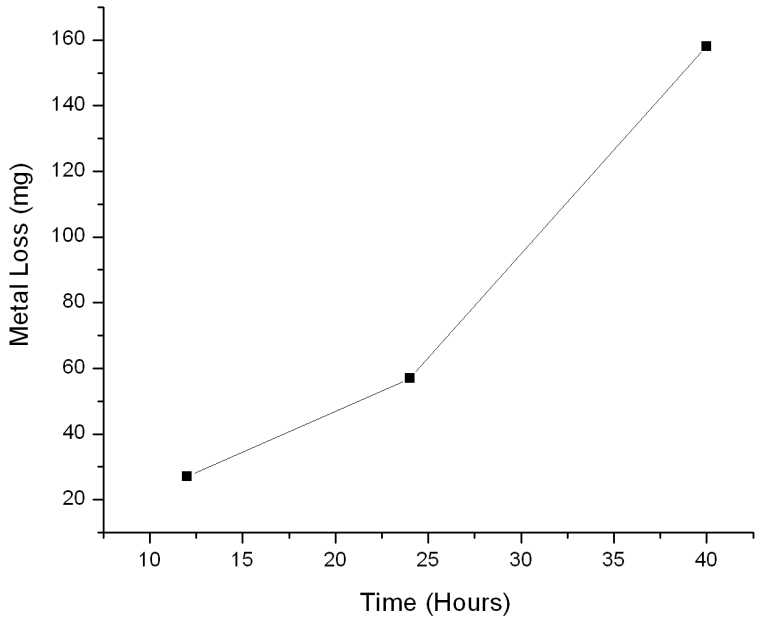

Figure 76: Metal loss versus T for GTD-111 DS at 1038°C (1900°F) in N_2 with 100 ppm H_2S.

H_2S was 0.828 mg/cm^2. This was an order of magnitude higher than the weight gain seen (0.087 mg/cm^2) in the wet air test. This suggests that while formation of a protective oxide layer is possible in both cases, the sulfur is also attacking the base metal, possibly because the oxide is porous or locally absent, which allows sulfur access to the surface.

At 871°C para-linear oxidation is observed, which was not observed in the wet air test. A thick oxide can be seen on the surface. However, this scale shows abundant, massive cracks, each of which can serve as a direct diffusion line for sulfur. At 1038°C, there is an initial linear increase in weight, which transitions to parabolic behavior as a compact oxide scale is formed, seen in Figure 78.

An Arrhenius plot was used to determine the activation energies for corrosion in both dry and wet N_2 with 100 ppm H_2S for samples that showed parabolic behavior. Figure 79 shows that the activation energy changes as water vapor is introduced to dry N_2 with 100 ppm H_2S. The addition of water vapor increases the activation energy from 50.3 kjoules/mole, for the dry case to 69.2 kjoules/mole for the tests conducted with water.

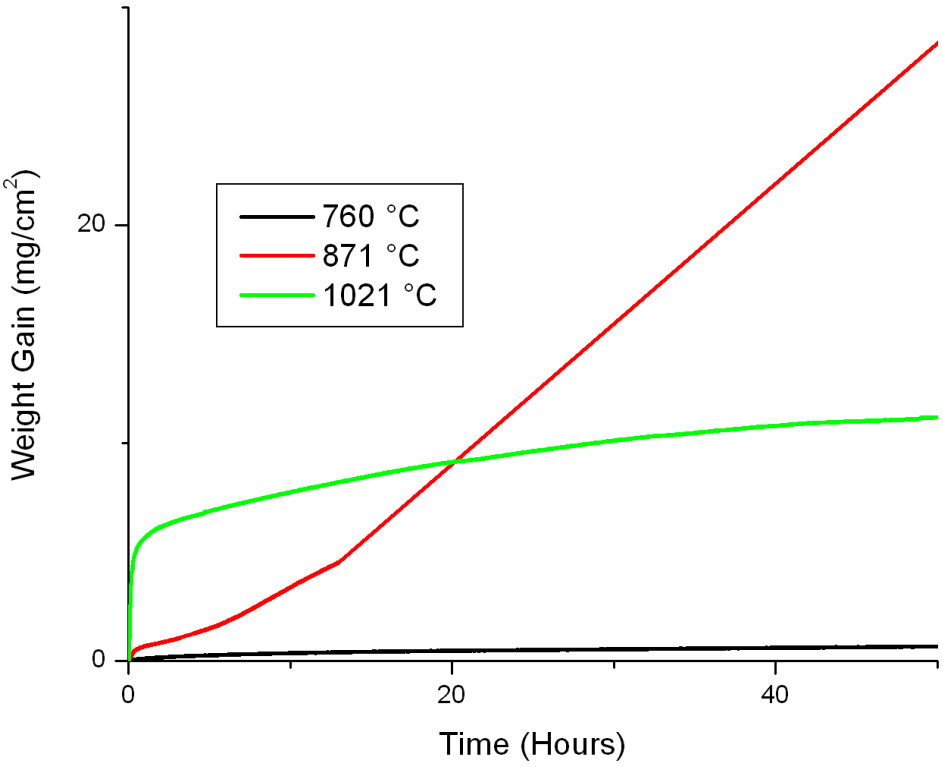

Figure 77: Weight gain versus T for GTD-111 DS at 760°C (1400°F), 871°C (1600°F), and 1038°C (1900°F) in wet N_2 with 100 ppm.

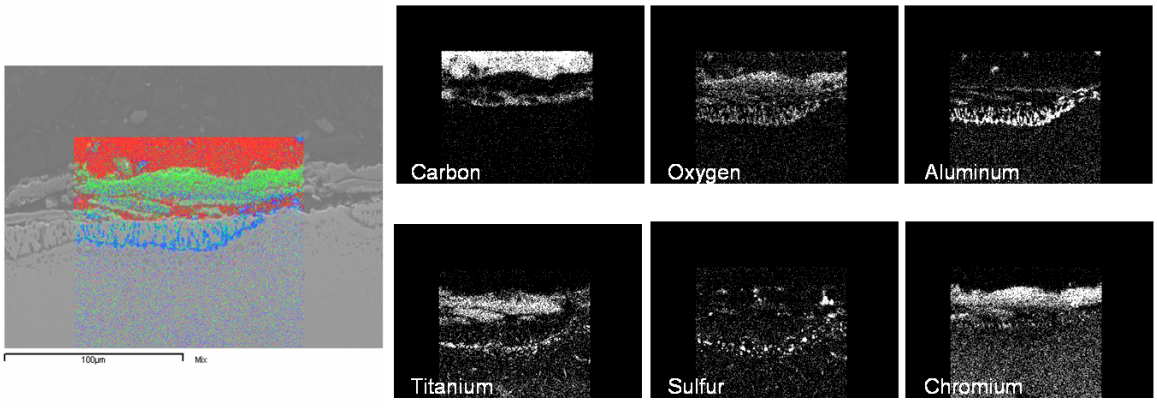

Figure 78: EDS x-ray map of a GTD-111 DS sample tested at 1038°C (1900°F) in wet N_2 with 100 ppm.

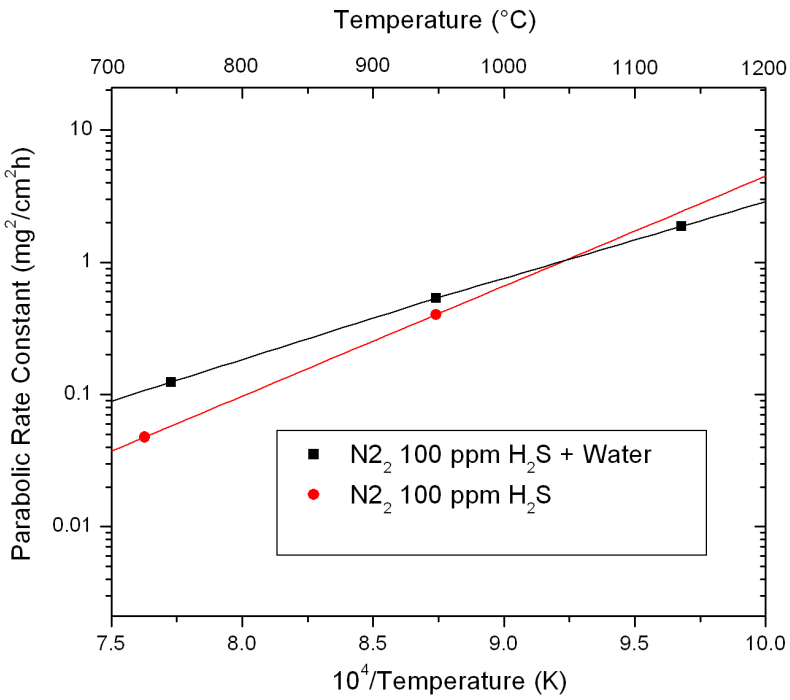

Figure 79: Arrhenius plot of parabolic rate constants versus 10^4/T for GTD-111 DS in dry N_2 100 ppm H_2S and wet N_2 with 100 ppm.

6.3.3 X-ray Diffraction

The exact composition of any scales formed on the surface were determined using x-ray diffraction (XRD) techniques. Table 8 summarizes the characterization of each TGA sample after testing. This technique was most useful when trying to confirm that the low melting phase Ni_3S_2 was present in addition to NiS. It is important to note that due to the relatively small penetration depth, only surface phases could be identified. To obtain accurate compositional information from cross sections, other techniques such as wavelength dispersive spectroscopy (WDS) or electron backscattered diffraction (EBSD) should be used.

Table 8: Summary of identified surface scales based on x-ray diffraction

Sample						
°C	°F	Atmosphere	Phases Indentified			
760	1400	Dry Air		TiO_2	Al_2O_3	Cr_2O_3
871	1600	Dry Air		TiO_2	Al_2O_3	Cr_2O_3
1038	1900	Dry Air		TiO_2	Al_2O_3	Cr_2O_3
760	1400	Air + H_2O		TiO_2	$NiCr_2O_3$	$CrO_{0.87}$
871	1600	Air + H_2O		TiO_2	$NiAl_2O_4$	Cr_2O_3
1038	1900	Air + H_2O		TiO_2	Al_2O_3	Cr_2O_3
760	1400	N_2 w/100 ppm H_2S		NiS	Ni_2S_3	Ni_xS_6
871-1	1600	N_2 w/100 ppm H_2S			NiS	
871-2	1600	N_2 w/100 ppm H_2S			NiS	
871-3	1600	N_2 w/100 ppm H_2S			NiS	
1038	1900	N_2 w/100 ppm H_2S		NiS	Ni_3S_4	CrS
760	1400	N_2 w/100 ppm H_2S+H_2O	NiS	NiS_2	Cr_2O_3	$CrO_{0.87}$
871	1600	N_2 w/100 ppm H_2S+H_2O	NiS	Ni_3S_2	TiO_2	$CrO_{0.87}$
1038	1900	N_2 w/100 ppm H_2S+ H_2O	Ni	NiS	Cr_2Ni_3	TiS

6.3.4 Grain Boundary Diffusion

Throughout this work, grain boundaries play an important role in fracture path and precipitate nucleation. When considering high temperature sulfidation, grain boundaries have been found to greatly influence the extent of corrosion damage. This can best be observed in Figure 80 which shows the dramatic "splitting" of a GTD-111 DS sample along a clear grain boundary after testing at 760°C. It is proposed that grain boundary diffusion leads

to the formation of the low temperature melting phase Ni_3S_2, also know as Heazlewoodite. This phase was identified by its metallic yellow color [55] and was also confirmed by XRD.

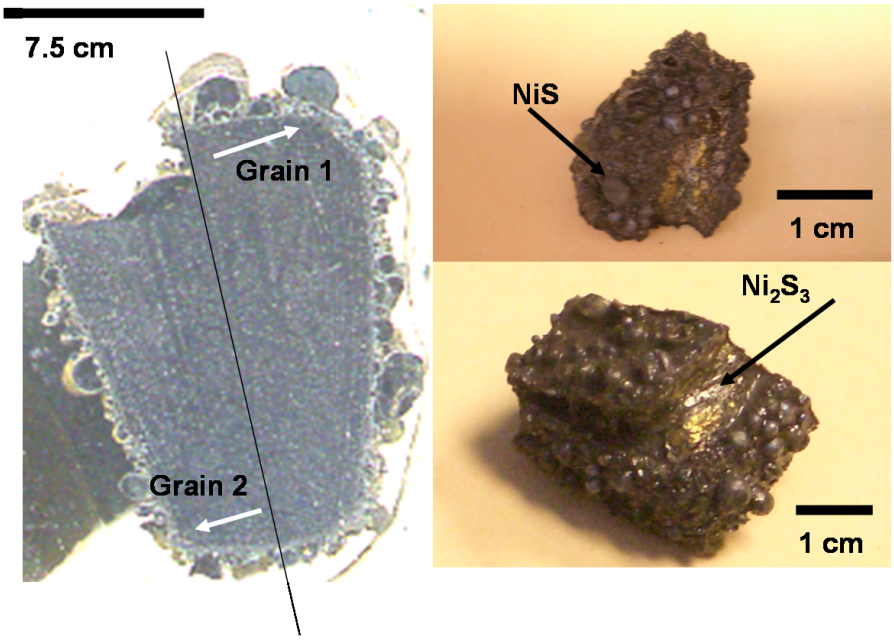

Figure 80: Images (courtesy of Morgana Martin) of a sample tested at 760°C that shows massive grain boundary corrosion that "splits" the sample along a grain boundary.

The issue of sample size versus the large columnar grain structure was again encountered during tests at 871°C, which demonstrates the importance of grain boundaries in sulfidation. Three samples, all tested at 871°C and designated 871-1, 871-2, and 871-3, were cut from an etched bar (Figure 81). This bar clearly contains at least two grains. However, depending on the specific cut, it is possible to include both grains, isolate a single grain, or cover a variety of grain boundaries, depending on the 3-D microstructure, which was not visible from the 2-D etched bar. Figure 82 is a plot of weight gain versus time for each of these three samples. In each case there is para-linear behavior, however the time at which breakdown occurs and the extent of corrosion is different for each specimen.

Cross-sectioning revealed that sample 871-1, which shows the greatest amount of corrosion, has a sulfide scale around the edges of the cross-section, but also corroded across an internal grain boundary (Figure 83). The behavior of this sample is similar to the 760°C sample shown in Figure 80. During the test, 871-1 fell out of the hot-zone of the furnace

Figure 81: Etched bar of GTD-111 DS showing the grain structure prior to sectioning and testing in the TGA.

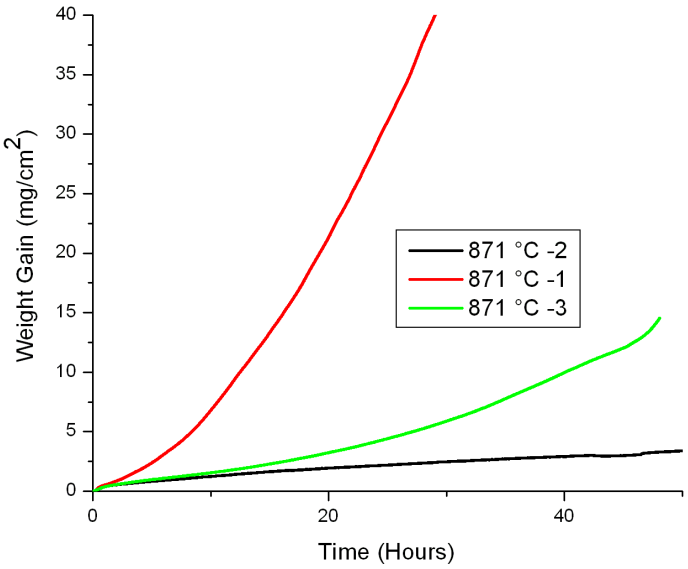

Figure 82: Weight gain versus time for three GTD-111 DS samples tested at 871°C (1600°F) in wet N_2 with 100 ppm H_2S.

and the test was interrupted. However, it is believed that the corrosion would continue across the grain boundary and "split" the sample.

The cross-sections of the remaining two samples tested at 871°C did not show any clear grain boundary corrosion. The two cross-sections are compared in Figure 84. The difference between the two samples was found to be cracking along the outer edges. Specimen 871-3 was heavily cracked along the edge and contained several internal cracks that are parallel to the sample edges. 871-3 subsequently experienced breakdown prior to sample 871-2, which showed no internal cracks. Apart from the sulfide scale along the outer edge, linear features parallel to the scales were observed. These "beachmark" features are also found

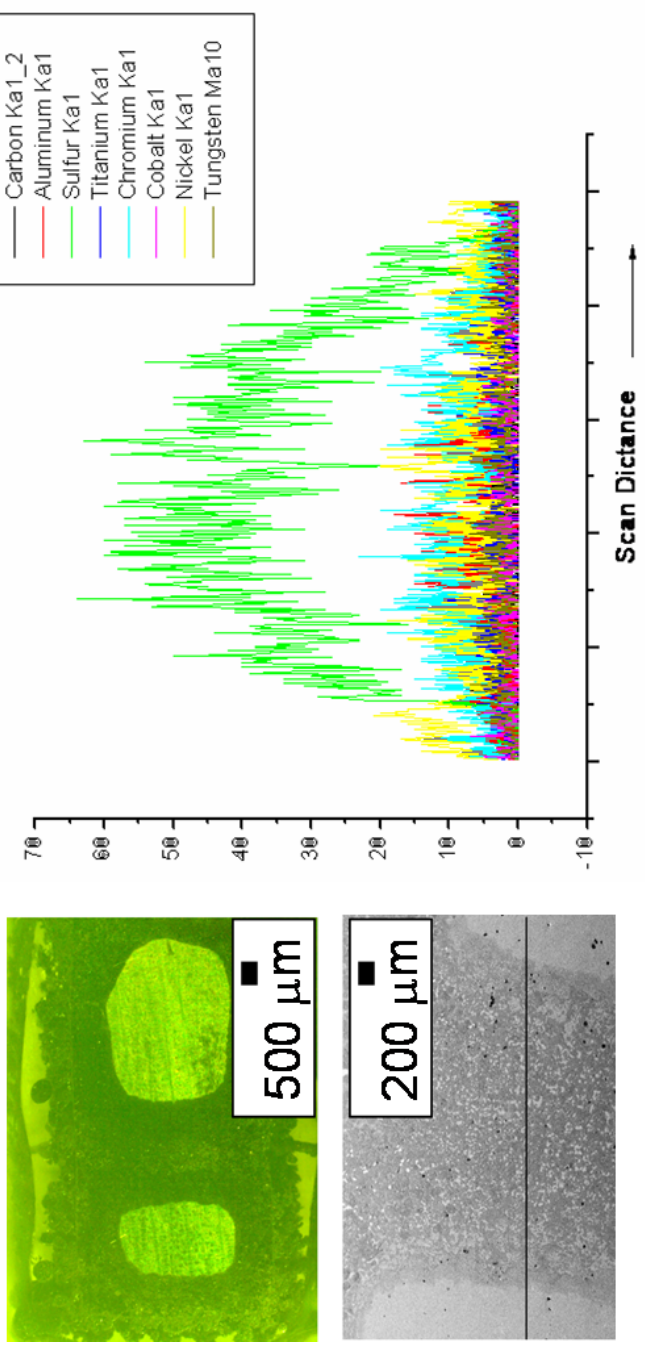

Figure 83: Images and EDS linescan of sample 871-1 that shows massive grain boundary corrosion as indicated by the increased sulfur concentration.

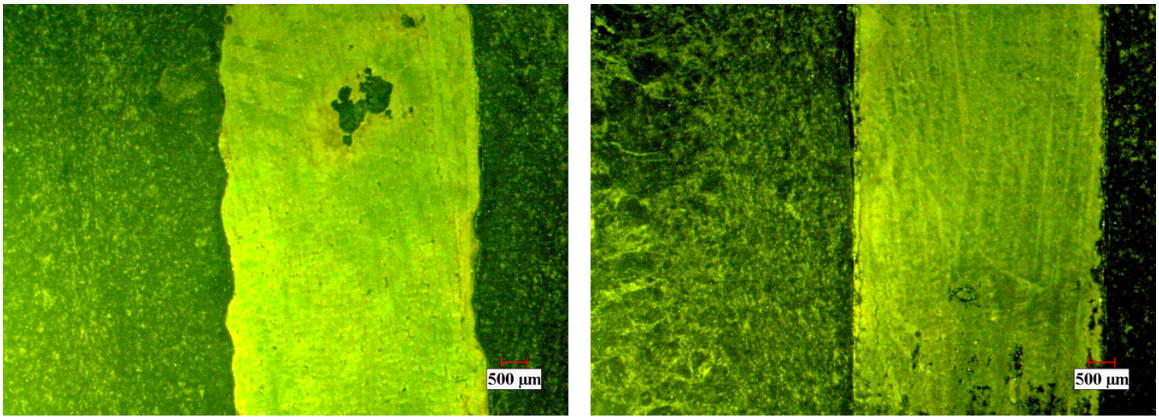

Figure 84: Images of cross-sectioned samples 871-2 and 871-3 that different cracking feature along the outer edges. The outer edges of 871-2 are more jagged, possibly because the edges include grain boundaries where the scale can crack. The edges 871-3 remain relatively planar and experience less damage as the scale remains intact and hinders further corrosion.

in the samples tested at 760°C and 1038°C. Figure 85 shows that the "beachmarks" are rich in sulfur and are spaced approximately 100 μm apart. This is significant because the secondary dendrite arm spacing is on this same scale. Therefore, diffusion of sulfide is enhanced by both grain boundaries and to a lesser extent, secondary dendrite arms, which form sub-boundaries. This observation was expected as diffusion is known to decrease from D_{GB} >D$_{sub}$ >D$_{bulk}$ [25].

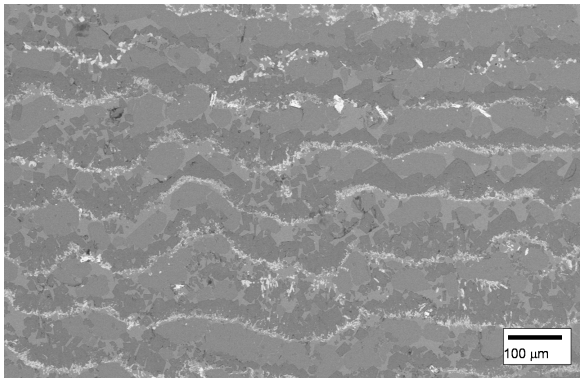

Figure 85: Image of "beachmarks" found in a GTD-111 DS sample tested at 760°C (1400°F) in dry N_2 with 100 ppm H_2S. EDS results show that the mark are rich in sulfur and are spaced approximately 100 μm apart.

6.3.5 Thermal Stress Effects

In addition to heavily corroded grain boundaries and beachmarks, secondary intergranular cracking was observed as a results of TGA tests in N_2 with 100 ppm H_2S as can be seen in Figure 86. These cracks were originally believed to be the product of sulfur attack of these boundaries. This is in agreement with the previous results (section 6.3.4) obtained showing sulfur diffusion in the areas between secondary dendrite arms. However, after SEM and EDS analysis, no sulfur was detected in the region of the cracks. Consequently, a second mechanism was proposed, in which the cracks form upon cooling from the test temperature. The CTEs of metals are much greater that those of oxides and sulfides. The result is that the metal will contract faster than the scale, which puts the metal under tensile loading. Given the substantial volume of scales, this type of failure mechanism was deemed possible, although further work can be done to quantify the levels of stress encountered. The importance of this finding directly applies during start-up and shut-down of turbine engines.

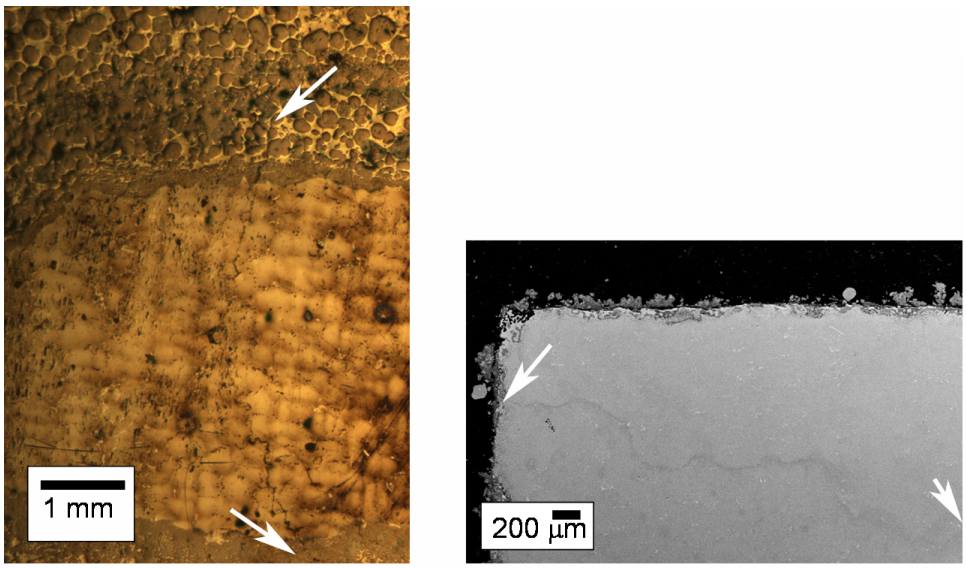

Figure 86: Cracked GTD-111 DS samples tested at 871°C and 1039°C. The cracks follow grain boundaries and shows no sign of sulfidation or oxidation

6.4 Conclusions

It was been found that mechanical properties such as fatigue life [12] are significantly diminished in the presence of Syngas. The focus of this work was to determine the kinetics of sulfidation under stress-free conditions and to investigate the role of microstructure during corrosion. These results indicate that catastrophic failure may occur in stress-free conditions either by direct grain boundary separation or by thermal stresses generated by a high difference of CTEs between the base metal and the sulfide/oxide scale.

High temperature oxidation/sulfidation test were conducted in both dry and wet conditions. Parabolic oxidation kinetics were observed in most samples and a direct link between grain boundaries and secondary dendrite arm spacing was observed. The significance of the work presented in this chapter towards steam and IGCC turbines can be summarized by:

1. TGA testing at 760°C, 871°C, and 1038°C in air confirmed parabolic oxidation behavior.

2. The addition of water vapor to the air increases the parabolic rate constant, k_p, but has a minimal effect on the activation energy, Q ($Q_{Dry} = 71.1$ kjoule/mole, $Q_{Wet} = 63.8$ kjoule/mole) of approximately 10%.

3. The activation energies of samples tested in N_2 with 100 ppm H_2S are lower than those of samples tested in air ($Q_{Dry} = -50.3$ kjoule/mole, $Q_{Wet} = -69.2$ kjoule/mole). The increase in activation energies with O_2 was attributed to the formation of oxide scales, which hinder corrosion.

4. Grain boundary "splitting" was observed at 760°C and 871°C in N_2 with 100 ppm H_2S due to enhanced diffusion.

5. Enhanced sulfur diffusion in the regions between secondary dendrites led to the formation of "beachmarks" spaced approximately 100 μm apart. These linear features were also observed to be prone to extensive cracking, which may aid corrosion.

CHAPTER VII

CONCLUSIONS

1. Due to the partially oriented structure of GTD-111 DS, samples sectioned in the transverse direction with respect to the growth axis will have approximately 4 times as many grain boundaries per unit length than longitudinally oriented samples. These grain boundaries are perpendicular to the loading axis and, based on creep elongation data, are weaker than longitudinally oriented grain boundaries.

2. Profile analysis has shown that for tensile tests conducted at temperatures of 25, 649, 760, and 871°C, the true area fraction of carbides on the fracture surface is significantly higher than the volume fraction of carbides found in the bulk material (2%) for longitudinally oriented samples.

3. For transversely oriented samples, where profilemetry could not be used, laser confocal microscopy was employed to determine the surface roughness number of the samples and calculate the true area fraction and number density of carbides on the fracture surface. Again, these values are 3-5 times greater than those found in the bulk material. This indicates that the carbides clearly influence the fracture of the material in both orientations, although there was a greater amount of carbides found in the longitudinal case. This is attributed to the fact that transversely oriented grains are weak and cause failure, whereas failure of longitudinally oriented boundaries, which are stronger, must be assisted by the presence of the carbides.

4. Examination of mating fracture surfaces of tensile specimen shows that carbides are cracking rather than debonding from the matrix.

5. Each of the three methods used to determine the γ' solvus temperature; metallography, DTA, and dilatometry, suggest that the solvus temperature is approximately 1200°C. This validates dilatometry as a method of investigation of as-cast superalloys.

6. Dilatometry has the ability to detect the delayed onset of precipitation reactions, and therefore the barrier to nucleation.

7. Heat treatment at 1300°C after 240 minutes eliminates the "eutectic" γ' while persevering the columnar grain structure and the volume fraction of carbides. Thus, tensile test specimens can be heat treated to isolate the carbides as possible fracture initiation sites without significantly changing the columnar grain structure of GTD-111 DS.

8. TGA testing at 760°C, 871°C, and 1038°C in air confirmed parabolic oxidation behavior.

9. The addition of water vapor to the air increases the parabolic rate constant, k_p, but has a minimal effect on the activation energy, Q ($Q_{Dry} = 71.1$ kjoule/mole, $Q_{Wet} = 63.8$ kjoule/mole) of approximately 10%.

10. The activation energies of samples tested in N_2 with 100 ppm H_2S are lower than those of samples tested in air ($Q_{Dry} = -50.3$ kjoule/mole, $Q_{Wet} = -69.2$ kjoule/mole). The increase in activation energies with O_2 was attributed to the formation of oxide scales, which hinder corrosion.

11. Grain boundary "splitting" was observed at 760°C and 871°C in N_2 with 100 ppm H_2S due to enhanced diffusion.

12. Enhanced sulfur diffusion along in the regions between the secondary dendrites led to the formation of "beachmarks" spaced approximately 100 μm apart. These linear features were also observed to be prone to extensive cracking, which may aid corrosion.

CHAPTER VIII

RECOMMENDATIONS

While the results of this work have enhanced the understanding of the relationship between microstructure and high temperature mechanical and corrosion properties, there are several facets that warrant further investigation. This chapter outlines several possible directions for further study of GTD-111 DS.

8.1 Microstructure

Large amounts of segregation are unavoidable during the processing of GTD-111 DS. However, precise analysis of the segregation of solute across the dendrite arms can help determine that extent of interdendritic stresses present, which can yield information about the phases that nucleate in the interdendritic regions. For example, discontinuous precipitation may be initiated by local deformation in addition to grain boundary diffusion. Therefore:

1. Determine the segregation of solute across dendrite arms accurately using wavelength dispersive spectroscopy (WDS), otherwise known as microprobe analysis.

2. Use dilatometry to measures the dendritic stresses that are caused by the amount of segregation in GTD-111 DS as outlined by Epishin *et al.* [56].

3. Investigate what effect, if any, these stresses have on discontinuous precipitation. Are the stresses large enough to trigger discontinuous solid solution precipitation after solidification of the alloy?

8.2 Tensile tests

Additional tensile tests should be preformed using the homogenization heat- treatment developed in this work to determine the effect of eliminating the "eutectic" precipitates as a function of temperature. Also, since it has been shown that sample size and orientation relative to the as-cast slab is important in terms of grain sampling, all tests should be

cut from polished material of known orientations. This would ensure that the important parameters, such as the number of grains per sample and their relative orientation,would be known prior to testing.

8.3 Corrosion

Further sampling of GTD-111 DS is needed since the results show a strong dependence on the number of grain boundaries present in each sample. Knowing exactly how many grain boundaries are present may help predict the extent of corrosion damage. Tests in polycrystalline GTD-111 as well and single crystal GTD-111 may also provide important information about the role of grain boundaries in corrosion.

Larger sample sizes for TGA experiments would also more accurately represent the microstructure of in-use components of GTD-111 DS. However, the high density of the alloy may prevent the use of sensitive a Cahn-type microbalance, as the weights of material would be too high. One alternative is using a spring balance that can handle very large sample sizes and can be automated using a digital imaging technique [57].

Finally, exposure tests of coated GTD-111 samples are needed as it is common practice for turbine components to be coated with a protective layer. Knowledge of how well the coating protects GTD-111 DS from the environment is an important factor to understand.

REFERENCES

[1] Gladstone Centre for Clean Coal. *http://www.gc3.cqu.edu.au*, 04/10/2005.

[2] D.A. Porter and E.A. Easterling. *Phase Transformation in Metals and Alloys*. Stanley Thornes, 1992.

[3] D.B. Williams and E.P. Butler. Grain boundary discontinuous precipitation reactions. *International Materials Review*, 26(3):153–183, 1981.

[4] I. Manna S.K Pabi and W. Gust. Discontinuous reactions in solids. *International Materials Review*, 46(2):53–91, 2001.

[5] C.S. Giggins and F.S. Petit. *Journal of the Electrochemical Society*, 118:1782–1790, 1971.

[6] W.F. Smith. *Structure and Properties of Engineering Alloys 2nd Ed.* McGraw-Hill, 1993.

[7] A.S. Khanna. *Introduction to High Temperature Oxidation and Corrosion*. ASM Internation, 2002.

[8] Alejandro Ibanez. PhD thesis, Georgia Institute of Technology, 2003.

[9] E.E. Underwood. *Quantitative Sterology*. Addison-Wesley, Reading, MA, 1970.

[10] R.T. Dehoff and Rhines. *Quantitative Microscopy*. McGraw-Hill, New York, 1968.

[11] M.D. Trexler B.C. Church and T.H. Sanders Jr. *Scripta Materialia*, (55):561–564, 2006.

[12] Ali Gordon. PhD thesis, Georgia Institute of Technology, 2005.

[13] Outokumpu Technology Products. *http://www.outokumputechnology.com*, 11/13/2006.

[14] Denny A. Jones. *Principle and Prevention of Corrosion*. Macmillan Publishing Co., 1992.

[15] ASM. *ASM HANDBOOK VOLUME 3: Phase Diagrams*, volume 3. 1992.

[16] W. Kurz and D.J. Fisher. *Fundamentals of Solidification*. Trans Tech Publication, 1998.

[17] M. Durand-Durand-Charre. *The Microstructure of Superalloys*. Gordon and Breach Science Publishers, 1997.

[18] Gregg M. Janowski. Master's thesis, Michigan Technological University, 1984.

[19] R.B. Scarlin. Discountinuous percipitation in a directionally solidified nickel-based alloys. *Scripta Metallurgica*, 10:711–715, 1976.

[20] E. Huron. Master's thesis, Georgia Institute of Technology, March 1986.

[21] W.W. Mullins and R.F. Serkerka. *Journal of Appied Physics*, 34:323–329, 1963.

[22] Mario Macia. PhD thesis, Georgia Institute of Technology, May 1996.

[23] Khachaturyan S. Semenovskaya V. and Morris J.W. *Acta Metallurgica*, 36:1563–1572, 1988.

[24] Wang Y. Banerjee D. Su C.C. Khachaturyan S. *Acta Metallurgica*, 46:2983–3001, 1998.

[25] Martin J.W. Doherty R.D and B. Cantor. *Stability of Microstructures in Metallic Systems*. Cambridge University Press, 1997.

[26] K.N. Tu and D. Turnbull. *Acta Metallurgica*, 15:369–376, 1967.

[27] Chester Sims. *Superalloys II*. John Wiley and Sons, 1987.

[28] E. Lvova and D Norsworthy. Influence of service-induced microstructural changes on the aging kinetics of rejuvenated ni-based superalloy gas turbine blades. *JMEPEG*, 10:299–313, 2001.

[29] M. Frebel and B. Otte. *Scripta Metallurgica*, 9:1317–1320, 1975.

[30] K.L Gasko G.M. Janowski and B.J. Pletka. *Materials Science and Engineering A*, 104:1–8, 1988.

[31] R. Leverant and M. Gell. The elevated temperature fatigue of a nickel-based superalloy, mar-m200 in conventionally-cast and directionally solidified forms. *Transaction of the Metallurgical Society AIME*, 245:1167–1173, June 1969.

[32] I. Chattaoraj S.K. Das S. Jana and S.P. Chakraborty. *Journal of Materials Science*, 30:5313–5320, 1995.

[33] Internation Joint Power Generation Conference. *Oxidation and Gamma Prime Particle Coarsening Behavior of IN-738 and GTD-111*. ASME, July 2000.

[34] Arun M. Gokhale. *AMS Handbook*, volume 9, pages 428–448. 2004.

[35] J.A Daleo K. A Ellision and D.A. Woodford. *Journal of engineering of Gas Turbines and Power*, 6:129–137, 1999.

[36] D.A. Woodford and A. Stiles. *Journal of Materials Engineering and Performance*, 6:521–533, 1997.

[37] A. Majumdar B.J.Wicks. *The 5th Australian Aeronautical Conference. Part 2 (of 2)*, pages pp. 375–378, 1993.

[38] Walter Milligan. PhD thesis, Georgia Institute of Technology, 1988.

[39] B.S. Rho H.U. Hong and S.W. Nam. *International Journal of Fatigue*, 22:683–690, 2000.

[40] M.J. Alinger G.R. Odette and G.E. Lucas. Tensile and fracture toughness properties of ma957:implications to the delopment of nancoposited ferritic alloys. *Journal of Nuclear Materials*, (307-311):484–489, 2002.

[41] M.J. Alinger G.R. Odette and G.E. Lucas. *International Journal of Fatigue*, 22:683–690, 2000.

[42] Arun M. Gokhale. *AMS Handbook*, volume 11, pages 538–556. 2002.

[43] William Drury. PhD thesis, Georgia Institute of Technology, September 1992.

[44] J. Goldstein D. Newbury P. Echlin D. Joy A. Romig C Lyman C. Fior and E. Lifshin. *Scanning Electron Microscopy and X-ray Microanalysis*. Plenum Press, 1992.

[45] K.E. Kurtis N.H. El-Ashkar C.L. Collins and N.N.Naik. Examing cement-based materials by laser scanning confocal microscopy. *Cement and Concrete Composites*, (25):695–701, 2003.

[46] M.J. Donachie Jr. and O.H. Kreige. Phase extraction and analysis in superalloys-summary of investigations by astm comittee e-4 task group 1. *Journal Of Materials*, 7(3):269–278, September 1972.

[47] Zupanic F.Boncina T.Krizman A. and F.D. Tichelaar. *Journal of Alloys and Compounds*, pages 290–297, 2001.

[48] A. Formenti A. Eliasson A. Michell and H. Frediksson. *High temperature Materials and Processes*, 24:239–258, 2005.

[49] W. D. Cao. Superalloys 718, 625 and Various Derivatives, page 147, 1991.

[50] W. Hermann M. Fahrmann and H.G. Sockel. Superalloys 2004, 24:517, 2004.

[51] Robert Speyer. *Thermal Analysis of Materials*. Marcel Dekker Inc., 1999.

[52] H.R. Last T.H. Sanders and J.M. Gonsalves. *Metallurgical Transactions:A*, 21A:557–565, 1990.

[53] ASM. *ASM HANDBOOK VOLUME 13: Corrosion*, volume 13. 1987.

[54] Apache Corp. Msds hydrogen sulfide. *http://www.apachecorp.com/*, 11/05/2006.

[55] Mineral of the Month Club. *http://webmineral.com/data/Heazlewoodite.shtml*, 10/30/2006.

[56] B. Fedelich A. Epishin T. Link U. Bruckner and P. Portella. Superalloys 2004, 24:537–543, 2004.

[57] M.D. Trexler P.M. Singh and T.H. Sanders Jr. *Review of Scientific Instruments*, 77(2):025103, 2006.